JOURNAL OF HYDRO - METEOROLOGY

ISSN 2525 - 2208

VIETNAM METEOROLOGICAL AND HYDROLOGICAL ADMINISTRATION

No 19
06-2024

Publishing licence
No: 166/GP-BTTTT - Ministry of Information and Communication dated 17/04/2018

Editorial office
No 8 Phao Dai Lang, Dong Da, Ha Noi
Tel: 024.39364963
Email: tapchikttv@gmail.com

Engraving and printing
Ha Thanh Thang Long Printing And Trading Joint Stock Company
Tel: 0243.2022639

JOURNAL OF HYDRO-METEOROLOGY
Volume 19 - 6/2024

TABLE OF CONTENT

JOURNAL OF
HYDRO-METEOROLOGY

Research Article

Application of MNDWI index for flood damage area calculation in Lam river basin using google earth engine platform

Ngoc Minh Trinh[1*]

[1] Faculty of Hydrology, Meteorology and Oceanography, Vietnam National University - Hanoi University of Science; trinhminhngoc@hus.edu.vn

*Corresponding author: trinhminhngoc@hus.edu.vn; Tel.: +84–966610784

Received: 15 February 2024; Accepted: 25 March 2024; Published: 25 June 2024

Abstract: Floods, as natural occurrences, often result in significant impacts on human life. The construction of flood maps plays a crucial role in devising appropriate strategies to mitigate the adverse effects of floods. In recent decades, there has been notable attention towards flood mapping methods utilizing remote sensing images. This paper introduces a methodology for generating an inundation map for rainy season and river network. To achieve this objective, we investigated the use of the recently developed Modified Normalized Difference Water Index (MNDWI) within the Google Earth Engine platform for extracting surface water. The study yielded flood maps extracted with considerable precision, facilitating the calculation and analysis of flood extents within the study area.

Keywords: Flood damage; Sentinel–2; Google earth engine.

1. Introduction

Since the dawn of history, floods have been one of the natural disasters that have appeared and caused a tremendous influence on human life. Especially in recent decades, floods have become increasingly fierce and unpredictable. Statistics show that the number of people affected by floods increased steadily from 147 million people per year (1981-1990) to 211 million people per year (1991-2000) [1]. Countries that have suffered from the severity of floods include China (2007), Thailand (2011), Japan (2011), India (2012), Myanmar (2012); in Europe: Central and Eastern European countries (2006 and 2013), France, Greece, Turkey (2007); in the Americas: Guatemala (2005), the United States (2009); in Africa: Angola (2010), Nigeria (2010) [2, 3]. Accordingly, it may be considered that floods are global in nature and increasingly complex, causing heavy damage. In terms of scale, they are not as intense as a tsunami or storm, but their impact is long-lasting and leaves many atrocious consequences for future generations.

Vietnam has faced floods since ancient times. This disaster occurs widely across the country, with floods appearing most frequently in the Central region, where rivers have steep slopes and high water concentration. In the Central region, the flood time is very rapid due to the swift flow of rivers and the inappropriate management of irrigation and hydroelectric reservoirs. As a result, the occurrence of floods, both natural and artificial, is quite frequent, posing significant challenges and obstacles for flood prevention management [4]. Flood situations and damage in some river basins in the Central region, such as the Lam River basin (total damage due to storms and floods in the 21 years from 1990 to 2010 amounted to more than 3,300 billion VND), Vu Gia - Thu Bon (from 1997 to 2009, natural disasters in the Vu Gia - Thu Bon river basin resulted in 765 deaths, 63 missing persons, and 2,403 injuries, with a total property damage value of more than 18,000 billion VND), and Ve - Tra Khuc (from

1996 to 2010, natural disasters caused 601 deaths and missing persons, 1,017 injuries, and the collapse and sweeping away of 8,501 houses [5–7]. According to statistics from 1990 to 2010, the Ca River basin suffered 34 direct landfall storms, with an average of 1 to 1.5 storms each year. The wind speed caused by the storms reached level 9 to 10, with gusts up to level 12. Storms often arrive in the Ca River basin from late September to early November. The maximum wind speed observed in Tuong Duong was 25 m/s in the west-north direction (1975), in Quy Chau, it exceeded 20 m/s in the west-north direction in 1973, and in Do Luong, it reached 28 m/s in the east-north direction (1965). Regarding floods, in the past 21 years, there have been 29 significant floods causing tremendous damage to people and property. Floodwater level monitoring data over the past 40 years shows that the greatest floods occurred in the main stream. Notable floods in the Ca River basin include those in 1954, 1963, 1973, 1978, 1988, 2007, and 2010. On average, major floods occur every 9 to 10 years. Some years have resulted in dike failures, as seen in the floods of 1954, 1978, 1988, and 1996. Especially in the flood of 1954, many dikes were breached (from Nam Dan to the sea), with floodwater flowing from the river into the fields for a continuous 16-days period. The total damage caused by storms and floods in the 21 years from 1990 to 2010 amounted to more than 3,300 billion VND. Solutions to minimize damage caused by floods include a set of structural measures (building flood prevention works, diverting floods, and relocating structures and people from flood-prone areas) as well as non-structural solutions [8–10]. The group of construction solutions is often directly effective but requires significant funds, making some solutions in this category challenging to implement. Therefore, priority is given to solutions within the non-structural group. One effective non-structural solution involves establishing a database with information on floods, risks, and the potential impact of floods on people's economic livelihoods. This includes data on flood depth, the extent of flooded areas within the city, and flood-prone zones [11–13]. Creating such a database enables localities to proactively formulate timely plans and solutions when faced with floods, representing a reasonable choice with high economic efficiency. In recent years, flood maps have become an increasingly effective tool for assessing the impact of floods on people. These maps provide a visual representation of the scope and level of flooding. Currently, there are various methods for constructing flood maps, with the most popular one recently applied in Vietnam being a combination of hydraulic modeling and GIS tools. This method has been implemented for more than a decade, utilizing both one-dimensional and two-dimensional models to construct flood maps. Notable applications include the study [14, 15] for the Quang Nam, the study [16, 17] for rivers in Khanh Hoa province, and [18, 19] for the Ben Hai and Thach Han river systems. While this method yields positive results and offers flexibility in calculating scenarios, it does have several limitations. A significant requirement is the considerable amount of input data needed for the model, necessitating time and effort for field surveys, data collection, and editing. The utilization of this method requires an experienced expert to verify and calibrate the model appropriately. Notably, in areas affected by rainfall in the field, the current hydraulic model may not fully address the issue. However, with the advancement of remote sensing technology, a new avenue has emerged for data collection and analysis. Remote sensing images have the capability to collect data over a broad area and an extended period with high repetition frequency. The availability of free satellite sources enhances the potential of this method as a valuable resource The method of using remote sensing images has been adopted by numerous domestic and international authors to determine the extent of flooding. The study [20] determined the coastline by calculating the difference threshold between the reflection levels in the green band and the NIR and MIR bands. However, the use of optical images may be hindered if the sky is covered with clouds, especially during periods of heavy rain. This challenge was addressed by [21–23] who utilized remote sensing images, ensuring that the information received is not limited by cloud cover. While this approach is suitable, it does not distinguish between

various water bodies (such as rivers and lakes) and flooded lands. Additionally, the study compared the differences between flooded and unflooded photos to discern areas affected by rain and areas with regular water presence.

This article presents the results of creating flood maps for the Lam River using Multiband Water index (MNDWI), implemented on the Google Earth Engine cloud computing platform. Google Earth Engine is a cloud-based geospatial analysis platform that enables users to visualize and analyze Earth satellite imagery. The platform's dataset encompasses over 40 years of historical and current global satellite imagery, along with the tools and computing power necessary to analyze and mine that extensive data trove without the need to download it to a local computer. Additionally, for more specific research purposes, users can create custom scripts by visiting https://code.earthengine.google.com/ [25,26]. From the perspective of flood research, the study [24] highlighted that with GEE, users no longer need to switch between different platforms where data is originally collected and distributed, so that GEE applications are reusable and can work with many different configurations. In the Field of Flood Research, it further demonstrates its usefulness by improving the reusability of GEE scripts and creating ready-to-use applications for other research areas, thus making it possible quickly create a flash flood map.

2. Materials and methods

2.1. Description of the study area

The Lam River basin, the second largest in the North Central region, originates from the mountainous areas of Laos. Covering an expansive area of 27,200 square kilometers within Vietnamese territory, it stretches from 18°15' to 20°10'30" North latitude and 103°45'20" to 105°15'20" East longitude. This basin encompasses significant portions of Nghe An and Ha Tinh provinces, along with a part of Nhu Xuan district in Thanh Hoa province.

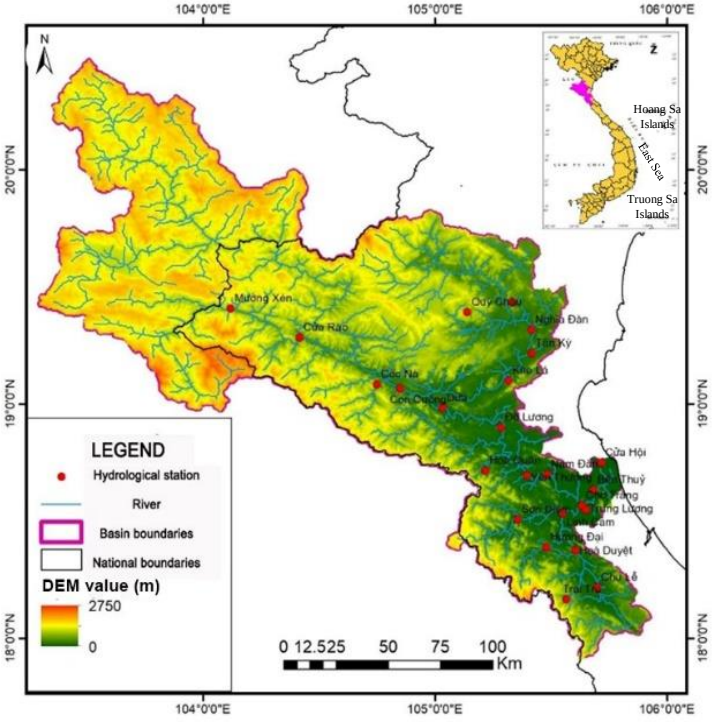

Figure 1. Map of the study area - Lam river basin.

The primary stream of the Lam River originates from the lofty peaks of Xieng Khouang province in Laos, where it gains elevation of over 2,000 meters. Initially flowing in a Northwest - Southeast direction, it then veers to a West - East trajectory before eventually meeting the sea at Cua Hoi. Despite its considerable length of 531 kilometers, the Lam River maintains a relatively stable main bed with minimal mudflats, showcasing a meandering coefficient of 1.74. With a river density of 0.6 km/km^2, the Lam River system is bolstered by 44 level I tributaries, which contribute significantly to its hydrological dynamics. Noteworthy among these tributaries are the Nam Mo River, Hieu River, Giang River, and La River. These tributaries, often originating from regions characterized by heavy rainfall, have a significant impact on the overall flow patterns within the basin [7, 27].

One of the most pressing challenges facing the Lam River basin is the occurrence of significant floods, primarily attributed to prolonged heavy rainfall on a large scale, coupled with the basin's slope and intricate river network. These floods, concentrated predominantly in the middle and lower reaches of the basin, are characterized by total rainfall exceeding 650 mm in the rain center, with extreme events reaching up to 1,500 mm, as witnessed during the devastating flood of 1978. An intriguing aspect of floods in the Lam River basin is the occurrence of dual peaks, particularly notable in major flood events such as those in 1978, 1988, 1980, and 2008 [28, 29]. The latter peak tends to be larger than the initial one, accentuating the complexity of flood dynamics within the basin. Notably, these peaks often coincide with the saturation of the basin's storage capacity, typically observed during the month of September. Understanding the intricate characteristics of the Lam River basin is paramount for effective flood management and mitigation strategies. By comprehensively analyzing its hydrological patterns, tributary dynamics, and flood behavior, policymakers and stakeholders can implement targeted measures to minimize the impact of floods and safeguard the communities residing within the basin and its vicinity.

2.2. Methods

While numerous techniques for extracting surface water have been introduced in previous studies, accurately extracting surface water in areas with low-reflectance background surfaces, such as mountainous shadows, high building shadows, and dark built-up areas like asphalt roads and dark building materials in downtown, remains a challenging problem. The presence of low-reflectance surfaces can lead to misclassification due to their similar low reflectance with surface water [25, 30, 31].

The passage discusses the development of a Modified Normalized Difference Water Index (MNDWI) aimed at improving the accuracy of surface water extraction in regions with complex backgrounds. The study evaluates the effectiveness of the proposed MNDWI compared to six other commonly used water indices across various climatic zones and seasons. The objective is to create a water index (MNDWI) that consistently delivers highly accurate surface water extraction, even in the presence of environmental noise.

In Vietnam, there are various approaches for calculating the MNDWI index on Landsat images, used for studying water resource changes [32], assessing coastline changes [33], and urban surface water body changes [34]. These studies typically involve downloading satellite images and processing them using specialized software, which can be limited due to pre- and post-processing requirements and the computational demands of the software. However, using platforms like Google Earth Engine (GEE) can overcome these limitations by providing efficient processing and reducing solution time [24, 30].

The study [35] specifically focuses on calculating three water indices (NDWI, MNDWI, and WNDW) to interpret water areas in Sentinel–2 images on the GEE platform. The results show high efficiency in processing and solution time, indicating the potential of using GEE for remote sensing image analysis, particularly for water resource monitoring and management in Vietnam.

The MNDWI was chosen for water classification, since it has produced the best results in the literature among the index-based algorithms. The MNDWI is based on distinctions between water and other low-reflectance surfaces [36], restricting the brightness value ranges used to those in the lower or “darker” section of the terrestrial spectral range, being characteristic of water [37]. The MNDWI is intended to limit non-water pixels while improving surface water information. The study [38, 39] provided details of the concept of MNDWI, and the calculation is given in Equation (1). In addition, to eliminate mountainous shadows that were mistakenly classified as water bodies, we placed a threshold of 5% slope over the study area, and areas with higher slopes were automatically excluded from the water class.

$$\text{MNDWI} = \frac{\text{Green} - \text{SWIR}}{\text{Green} + \text{SWIR}} \quad [40–42] \tag{1}$$

where Green is the pixel values from the green band; SWIR is the pixel values from the short-wave infrared band.

The research methodology is depicted through the following research diagram (Figure 2).

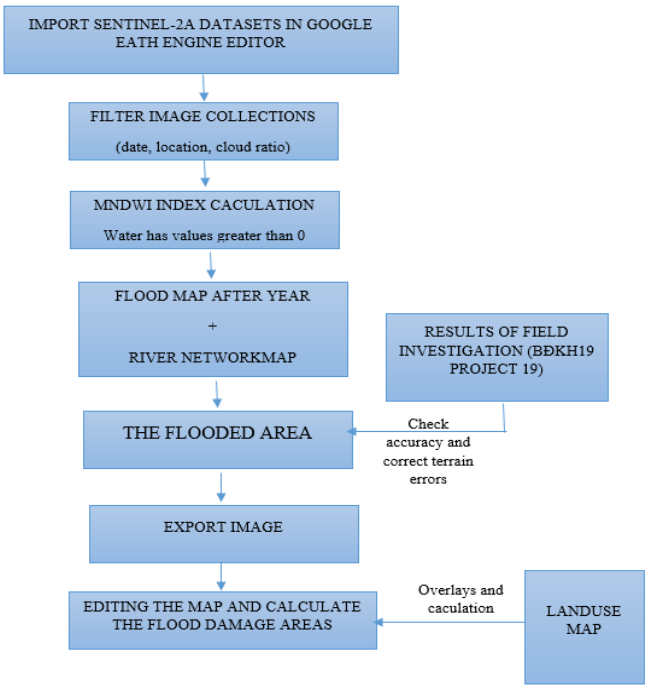

Figure 2. Flowchart illustrating the research steps.

2.3. Data collection

The authors utilized Sentinel–2 remote sensing imagery with a spatial resolution of 10 meters from the Google Earth Engine dataset. The dataset comprises 178 images acquired between October 1, 2015, and October 31, 2022, which were employed to construct a comprehensive river and stream network map. Specifically, an image captured on October 17, 2022, was employed to generate a flood map post-rainfall. By overlaying these two maps, the flood extent was extracted (Figure 3). Given that each individual image only covers half of the basin area, the authors undertook specialized processing of image pairs to seamlessly combine them, thereby creating a unified image of the entire basin. Figure 2 illustrates the process flowchart for distinguishing and identifying flooded and non-flooded areas using the Modified Normalized Difference Water Index (MNDWI) on the Google Earth Engine (GEE) platform as implemented in the study. The steps and main processes for Sentinel–2 image interpretation can be summarized as follows. Firstly, Sentinel–2 images covering the study area are collected. Next, image processing is conducted to eliminate the effects of noise factors. Subsequently, a high-pass filter is applied to homogenize the spatial resolution (10 m) for all bands. Using the MNDWI index, pixels are classified into water and non-water (post-rain flood) areas within the study area. Finally, the computed results are evaluated to assess the accuracy of identifying, distinguishing, and interpreting water and non-water areas within the study region. Post-rain flood areas and river/stream networks are overlaid to calculate the flooded areas. Then, these areas are extracted in vector form and inputted into MapInfo software for comparison with land use maps, calculating damage extents for each land type, and editing the final product map.

The test data includes the flood map of the Lam River basin developed as part of the BDKH19 project in 2015, along with flood trace survey data from 2013 to 2014 [40, 41], as documented in previous studies [7, 9, 28]. These datasets were utilized to perform a comparative analysis with the threshold classification results. The comparison revealed that the flood area calculated using both methods exhibited equivalent accuracy, reaching 99%.

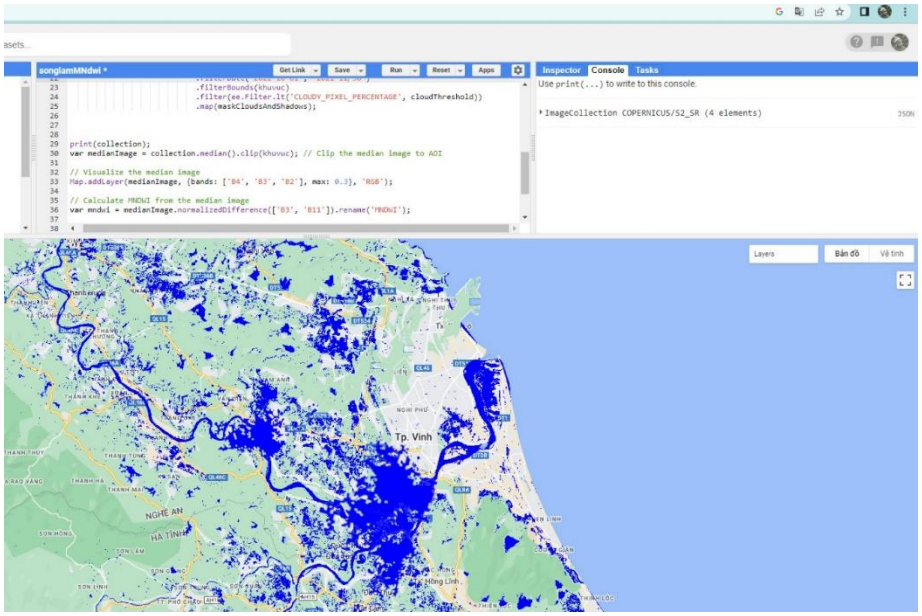

Figure 3. The output of water mask interpretation (MDNWI menthod) in Google Earth Engine.

To assess the accuracy of interpretation results derived from remote sensing imagery, the study incorporated additional field datasets comprising flood trace surveys (comprising 200 surveys) using the Kappa error construction method [42–44]. The Kappa error of the interpretation results obtained from remote sensing imagery demonstrated a high accuracy level, reaching 97%.

3. Results and discussion

The analysis of satellite images (Figure 4) revealed that the total flooded area spans 98,143 hectares. Predominantly, flooding is concentrated in several districts, including Ky Son and Tuong Duong (Nam Mo - Nam Non river area), Que Phong and Quy Chau (Upper Hieu river), Quy Hop Nghia Dan, Thai Hoa, Tan Ky, and Con Cuong (Ca river), as well as Anh Son, Do Luong, Thanh Chuong (Ca river), parts of Huong Son, Huong Khe, Vu Quang, Duc Tho (Ngan Pho, Ngan Sau, La rivers), and Hung Nguyen, Nghi Loc (Lam River downstream) districts. The areas affected by flooding mainly concentrate in the downstream areas of Thanh Chương, Nam Đàn, Đàm Đàn, and Hưng Nguyên districts. Places less affected by floods are typically mountainous regions, primarily consisting of forested and perennial crop lands. This result is consistent with the findings in document [4] when calculating flood exposure. The obtained results closely resemble those of previous flood studies [4, 39, 40] utilizing flood models.

To assess the impact of flooding on land use categories within the study area, the authors utilized land use maps provided by the Ministry of Natural Resources and Environment in 2010, which delineate over 70 distinct land types. These were classified and grouped into five main categories: bare land and rivers, forest land and industrial crops, agricultural land and aquaculture, residential and commercial land, and public infrastructure. The results, as presented in Table 1, indicate that the scope of flood damage predominantly affects public infrastructure such as schools, hospitals, flood-resistant housing, administrative areas, and roads. The results indicate that areas used for public facilities such as schools, hospitals,

storm shelters, administrative centers, and transportation routes are frequently prone to flooding. These locations often host large populations seeking refuge from floods and serve as centers for relief efforts. If transportation routes and densely populated areas are flooded, residents may become isolated, leading to increased risks to both lives and finances.

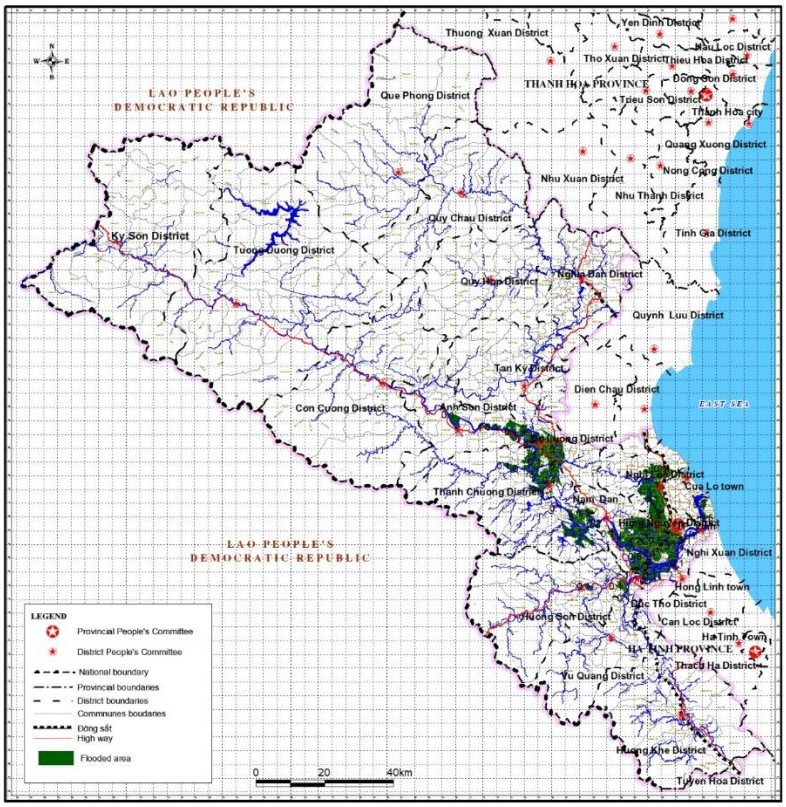

Figure 4. The Lam River basin flood map derived from remote sensing imagery, following the extraction of flood areas using Google Earth Engine.

Therefore, the government needs to inspect and maintain communication systems before the flood season to ensure the continuity of communication networks within flood-affected areas. Public infrastructure should be robust and spacious enough to accommodate residents seeking refuge. Residential and commercial land use areas are less susceptible to flooding compared to public infrastructure; however, since households' residences contain family assets including food supplies, livestock, and other household items, the government should encourage people to build homes in safe areas. Families at risk of flooding should be supported to construct sturdy residences meeting flood-resistant standards to mitigate flood risks.

Table 1. The range of damage due to flooding calculated through satellite image analysis results.

No	Land-use type	Damaged area (ha)	Damaged percentage (%)
1	Public land	45460	45.75
2	Housing land and production and business land	18255	18.37
3	Agricultural land and aquaculture land	14200	14.29
4	Forest land and industrial crops	16500	16.61
5	Bare land and rivers	4947	4.98
	Total damage	**98143**	**99362**

The residents living in the downstream area of the Lam River primarily engage in agriculture, with rice cultivation being the main source of food and income for them. When rice paddies and flower fields are flooded, it causes significant damage and long-term impacts

on the livelihoods of the people. They have to wait until the next planting season to restore their production activities. However, rice and flowers are less resilient to flooding compared to other industrial crops, thus the extent of damage to rice paddies and flower fields during floods is higher than that of industrial crops. Meanwhile, vacant lands or higher ground near rivers are less prone to flooding.

4. Conclusions

The study has demonstrated the effectiveness of flood analysis results obtained from Sentinel–2 remote sensing images using the MNDWI method, yielding relatively good outcomes. The analysis revealed concentrated flooding in several districts, including Ky Son, Tuong Duong, Que Phong, Quy Chau, Quy Hop, Nghia Dan, Thai Hoa, Tan Ky, Con Cuong, Anh Son, Do Luong, Thanh Chuong, Huong Son, Huong Khe, Vu Quang, Duc Tho, Hung Nguyen, and Nghi Loc, with the Lam River downstream experiencing significant impact. Additionally, the study calculated the extent of flood damage, highlighting the predominance of affected areas in public lands (44.26%), agricultural lands (34%), and residential lands (22%), emphasizing their critical role in flood prevention efforts. The research findings contribute to flood damage assessment and monitoring, underscoring the need for local authorities to enhance flood prevention measures through robust planning and prompt implementation to restore normalcy in production and daily activities, thereby minimizing economic and human losses. Researching flood damage through inundation area using a remote sensing index remains constrained. In forthcoming studies, the author intends to expand their research by assessing the effects of water extraction through multiple remote sensing indices.

Author contribution statement: Conceived and designed the experiments; Analyzed and interpreted the data; manuscript editing: T.M.N.; Analysis tools or data; performed the experiments: T.M.N.; Wrote the draft manuscript: T.M.N.; Contributed reagents, materials: T.M.N.

Competing interest statement: The authors declare no conflict of interest.

References

1. King, D.; Macgregor, C. Using social indicators to measure community vulnerability to natural hazards. *Aust. J. Emerg. Manage.* **2000**, *15(3)*, 52–57.
2. Hebb, A. Floods: mapping vulnerability in the upper Thames watershed under a changing climate. Report XI, CFCAS project of water resources risk and vulnerability to changing climatic conditions. University of Western Ontario, London, 2007.
3. Blaikie, P.; Cannon, R.; Davis, I.; Wisner, B. At risk: Natural hazards, people's vulnerability, and disasters, 1994.
4. Anh, L.T.; Anh, T.N.; Dat, T.V.; Giang, N.T.; Hung, N.Q.; Kha, D.D.; Ngoc, T.M.; Son, N.T.; Tuan, N.C.; Van, C.T. Flood inundation maps and vulnerability assessment maps due to floods in the basins of the Lam River, Ben Hai - Thach Han, and Thu Bon. Science and Technics Publishing House, 2015.
5. Luan, N.T.; Hung, N.T.; Cuong, V.D.; Huyen, N.T.; Son, P.Q. Research on creating flood maps from Radar remote sensing images applied to the Tra Khuc and Ve River basins, Quang Ngai province. *J. Water Resour. Technol.* **2017**, *39*, 1–8.
6. Son, N.T.; Van, C.T. Method of assessing vulnerability - Theory and practice. Part 1: Applicability in assessing flood vulnerability in Central Vietnam. *VNU J. Sci.: Nanosci. Sci. Technol.* **2012**, *2*, 115–122.
7. Kieu, T.D. Research on managing large floods in the Lam river basin. Doctoral Thesis, Hanoi, 2012.

8. Tuyen, H.M. Research on developing a decision support framework for water resources management in the Ca River Basin. Ministry of Science and Technology research, 2004–2006.
9. Son, N.T.; Anh, T.N.; Kha, D.D.; Tien, N.X.; Thin, L.V. Testing the impact assessment of Climate Change on flooding in the downstream area of the Lam River. *J. Hydrometeorol.* **2014**, *645*, 13–20.
10. An, T.V.; Lanh, N.V. A study to identify weather patterns causing heavy rain in Nghe An province. *J. Sci. Technol*. **2019**, *2*, 9–17.
11. Bhusal, A.; Thakur, B.; Kalra, A.; Benjankar, R.; Shrestha, A. Evaluating the effectiveness of best management practices in adapting the impacts of climate change–induced urban flooding. *Atmosphere* **2024**, *15(3)*, 281.
12. Ámon, G.; Bene, K.; Ray, R.; Gribovszki, Z.; Kalicz, P. Improving flash flood hydrodynamic simulations by integrating leaf litter and interception processes in steep–sloped natural watersheds. *Water* **2024**, *16(5)*,750.
13. Dulawan, J.M.T.; Imamura, Y.; Amaguchi, H. Social drivers of flood vulnerability: understanding household perspectives and persistence of living in flood zones of Metro Manila, Philippines. *Water* **2024**, *16(6)*, 799.
14. Van, C.T.; Hung, B.V.; Anh, V.T.V.; Nam, N.V.; Tuan, N.C.; Nguyen, B.Q.; Viet, C.T.; An, N.V.; Son, N.T.; Ninh, L.V (NASATI). Research on developing a method for assessing flood risk in the Mekong Delta region – Pilot application for An Giang province, 2021.
15. Van, C.T.; Son, N.T.; Anh, T.N.; Tuan, N.C. Developing vulnerability indices for flood susceptibility using the Analytic Hierarchy Process (AHP) method – Testing on several commune–level units in Quang Nam province within the lower basin of the Thu Bon River. *J. Hydrometeorol*. **2017**, *643(04*), 10–18.
16. Kha, D.D.; Duc, D.D.; Binh, H.T.; Quyen, L.N.; Quang, T.X.; Anh, T.N. Building flood inundation maps for the main river systems in Khanh Hoa province according to climate change scenarios. *VNU J. Sci.: Nanosci. Sci. Technol*. **2013**, *29*, 101–102.
17. Anh, T.N.; Duc, D.D.; Kha, D.D.; Quynh, P.T.N.; Binh, H.T.; Dung, D.T.H.; Son, B.M.; Thanh, N. Developing a method to assess the impacts of climate change and sea level rise on technical infrastructure – Testing for the coastal areas of Khanh Hoa province. *VNU J. Sci.: Nanosci. Sci. Technol*. **2024**, *29(4*), 1–12.
18. Long, V.D.; Anh, T.N.; Binh, H.T.; Dinh, D. Introducing the flood forecasting technology for the Ben Hai and Thach Han river systems using the MIKE 11 model. *VNU J. Sci.: Nanosci. Sci. Technol*. **2010**, *26(3)*, 397.
19. Anh, T.N. Building flood inundation maps for the Ben Hai and Thach Han rivers in Quang Tri province. *VNU J. Sci.: Nanosci. Sci. Technol*. **2011**, *15*.
20. Alesheikh, A.A.; Ghorbanali, A.; Nour, N. Coastline change detection using remote sensing. *Int. J. Environ. Sci. Technol*. **2007**, *4*, 61–66.
21. Toan, D.D.; Quan, N.A.; Son, N.H.; Ngoc, N. Researching the development of flood inundation maps for the lower reaches of the Dak Bla River. *J. Water Resour. Environ. Eng.* **2015**, *28*, 1–99.
22. Toan, N.T.; Chau, T.K.; Tam, D.T.; Linh, N.H. Application of remote sensing technology to construct flood inundation maps for the Bui River area during the historic flood of 2018. *J. Water Resour. Environ. Eng.* **2019**, *66*, 81–87.
23. Chau, T.K. Mapping extent of flooded areas using Sentinel–1 satellite image. *J. Water Resour. Environ. Eng.* **2017**, *58*, 79–82.
24. Li, Z.; Demir, I. MultiRS flood mapper: A google earth engine application for water extent mapping with multimodal remote sensing and quantile–based postprocessing. *Environ. Modell. Software* **2024**, *176*, 106022.

25. Liu, C.; Xu, J.; Xu, K.; Yu, J. Mapping large-scale aquaculture ponds in Jiangsu Province, China: An automatic extraction framework based on Sentinel–1 time-series imagery. *Aquacult.* **2024**, *581*, 740441.
26. Bandak, S.; Naeini, S.A.R.M.; Komaki, C.B.; Verrelst, J.; Kakooei, M.; Mahmoodi, M.A. Satellite–based estimation of soil moisture content in croplands: A case study in Golestan province, North of Iran. *Remote Sens.* **2023**, *15(8)*, 2155.
27. Hung, N.Q.; Son, N.T.; Kha, D.D. Development and application of flood vulnerability indies for commune level – A case study in Lam river basine, Nghe An province, Vietnam. International Young Researchers Workshop River Basin Environment and Management, Thailand, 2014.
28. Kieu, T.D.; Dinh, L. Researching indicators of major floods and delineating areas prone to major flooding in the Lam River basin. *J. Water Resour. Environ. Eng.* **2011**, 3–8.
29. Anh, T.N.; Binh, H.T. Report on the development of a 1–D, 2–D integrated hydraulic model for sediment deposition in the Ca River basin. A research project on hydrological adaptation to climate change and the establishment of a multi-stakeholder information system to minimize vulnerability in the North Central region of Vietnam. (CPIS)–11.P04.VIE, 2012–2015.
30. Zhang, C.; Zhang, H.; Tian, S. Phenology–assisted supervised paddy rice mapping with the landsat imagery on google earth engine: Experiments in Heilongjiang province of China from 1990 to 2020. *Comput. Electron. Agric.* **2023**, *212*, 108105.
31. Lu, H.; Zhao, R.; Zhao, L.; Lyu, B.; Wang; J.; Zhang, L. A contrarian growth: The spatiotemporal dynamics of open–surface water bodies on the northern slope of Kunlun Mountains. *Ecol. Indic.* **2023**, *157*, 111249.
32. Hoa, N.H.; Anh, N.T. Using the NDWI and MNDWI indices to assess changes in groundwater resources due to mineral extraction activities in Hoanh Bo district, Quang Ninh province. *Vietnam J. Sci. Technol*. **2017**, *169(09)*, 111–116.
33. Quynh, H.N.N.; Khoi, D.N.; Hoa, H.C.; Bay, N.T. Using landsat satellite images for assessing riverbank changes in the Mekong and Bassac rivers in the An Giang province. *J. Hydro-Meteorol.* **2018**, *9(130)*.
34. Tuan, V.A.; Hang, L.T.T.; Quang, N.H. Monitoring urban surface water body changes using MNDWI estimated from pan-sharpened optical satellite images. *J. Sci.* **2018**, *15(11b)*, 29–36.
35. Chien, P.V. Researching water indices identification from Sentinel–2 images on google earth engine: Application for Sa Dec city, Dong Thap province. *J. Water Resour. Technol.* **2020**, *60*, 1–9.
36. Anusha, B.N.; Raghu Babu, K.; Rajasekhar, M. Geospatial approaches for monitoring and mapping of water resources in semi-arid regions of Southern India. *Environ. Challenges* **2022**, *8*, 100569.
37. Silva, J.B.A.; Almeida, G.L.P.; Almeida, A.C.D.S. Characterization of water status and vegetation cover change in a watershed in Northeastern Brazil. *J. South Am. Earth Sci.* **2023**, *130*, 104546.
38. Rashid, Md.B. Monitoring of drainage system and waterlogging area in the human–induced Ganges–Brahmaputra tidal delta plain of Bangladesh using MNDWI index. *Heliyon* **2023**, *9*, e17412.
39. Dong, X.; Hu, C.; Zhao, Y. Novel threshold self-regulating water extraction method. *J. Hydrol. Eng.* **2023**, *28(8)*, 04023020-1– 04023020-9.
40. Kha, D.D.; Duc, D.D.; Binh, H.T.; Quyen, L.N.; Quang, T.X.; Anh, T.N. Developing a template questionnaire to assess flood resilience of residents for evaluating vulnerability to floods. *VNU J. Sci.: Nanosci. Sci. Technol*. **2013**, *29(2S)*, 101–112.

41. Kha, D.D.; Son, N.T.; Anh, T.N. Developing maps of flood risk, sensitivity, and resilience to support the creation of flood vulnerability maps in the Lam River basin. National Workshop on Climate Change – Impact Assessment, Vulnerability Evaluation, and Proposal of Adaptation Solutions to Climate Change, Da Nang, Vietnam. 2014, pp. 115–119.
42. Rosenfield, G.H.; Fitzpatrick–Lins, K. A coefficient of agreement as a measure of thematic classification accuracy. *Photogramm. Eng. Remote Sens*. **1986**, 223–227.
43. McHugh, M.L. Interrater reliability: The Kappa statistic. *Biochem Med.* **2012**, *22(3)*, 276–282.
44. Ju, Y. Water bodies' mapping from Sentinel–2 imagery with modified normalized difference water index at 10m spatial resolution produced by sharpening the SWIR Band. *Remote Sens.* **2016**, *354(8)*, 1–19.
45. Moreri, K.K. Using Kappa methodology to consider volunteered geographic information in official land administration systems in developing countries. *Spatial Inf. Res.* **2020**, *28*, 299–311.

JOURNAL OF
HYDRO-METEOROLOGY

Research Article

Analytical methods used in microplastics identification: A review

Huynh Phu[1], Huynh Thi Ngoc Han[2]*, Tran Ngoc Nu[3]

[1] HUTECH University; Hutech University of Applied Sciences; h.phu@hutech.edu.vn
[2] Hochiminh City University of Natural Resources and Environment; htnhan_ctn@hcmunre.edu.vn
[3] Institute for Environment and Circular Economy Southern; tngocnu043@gmail.com

*Corresponding author: htnhan_ctn@hcmunre.edu.vn; Tel.: +84–975397953

Received: 12 March 2024; Accepted: 08 April 2024; Published: 25 June 2024

Abstract: Microplastic research plays a crucial role in identifying microplastic polymers. Scientists use different methods such as Flame tests, Differential thermal scanning, Thermogravimetric analysis, and Infrared spectroscopy to accomplish this. The objective of this study incluce: (i) Firstly, it aims to summarize recent research trends on techniques for determining polymer types in various environments. It provides an overview of each technique and compares their strengths and limitations. (ii) Secondly, it determines the types of microplastics in surface water samples in the Saigon - Dong Nai River basin, during the period 2023. The Fourier transform infrared spectroscopy (FTIR) technique is applied according to the total attenuation method (ATR-FTIR). The study shows that it is possible to quantify and classify microplastics by manual observation or through observation or microscopy. However, determining the type of polymer is almost impossible. To overcome this limitation, scientists use a combination of physical (e.g., light microscopy, magnifying microscopy), chemical (e.g., spectroscopy), and thermal analysis techniques. The study results reveal that there are more than 60 types of microplastics present in the main water supply for daily drinking and drinking purposes of the people of Ho Chi Minh City and neighboring provinces. It provides a foundation for river basin water resource managers to propose appropriate water resource management measures and programs during the process of water exploitation and use in the area.

Keywords: Identification of microplastics; Microplastic analysis methods; Microplastics in surface water; Microplastics; Saigon River - Dong Nai.

1. Introduction

Since 2019, almost the whole world has been and will be struggling with a global pandemic - the Covid 19 epidemic. The World Health Organization has requested a 40% increase in disposable PPE (Polyphenylene Ether) production. Currently, the most commonly produced plastics are polypropylene (PP), polyethylene (PE), polyvinyl chloride (PVC), polyethylene terephthalate (PET) and polystyrene (PS) [1]. The term microplastics was first mentioned by Thompson and colleagues in 2004 [2]. Microplastics are defined as particles ranging in size from 1-5000 μm [3]. More clearly, it is distinguished as plastic particles, pieces, and fibers with a size of 5 to 1 mm, while a size of 1 mm or less is considered microplastic (nano-sized). They pose a potential risk to human health and the natural environment [4].

Identifying microplastics is quite complicated, there are many different methods [5]. Over the years, identification techniques such as Fourier transform infrared spectroscopy [6], Raman microscopy [7], gas chromatography desorption-mass spectrometry [8] or pyrolysis

gas chromatography [9] have had many improvements and more in-depth research. Many studies have been published on methods to identify microplastics [5, 10–11]. Additionally, research publications [12, 13] summarize knowledge gaps and future research priorities. Looking at the total number of research publications on microplastics over the past and present years clearly shows that there is a need to strengthen technical methods for identifying microplastics beyond sampling.

New analytical tools need to be developed and integrated with existing instruments to tackle the challenges in the field of microplastic identification. The main issue to be addressed is the limited ability of current techniques to detect microplastics of different sizes. The detectable size limit of microplastics using current methods is only a few micrometers. However, there is a growing need to identify the presence, distribution, and polymer type of microplastics of various sizes, particularly in the nanoscale range. The detection and identification of polymers in nano-microplastics pose a significant challenge in microplastics research.

Accordingly, the purpose of this article is to present and compare current advanced techniques that can identify microplastics in water samples, thereby gaining a more general overview of the advantages and disadvantages of these methods. Techniques for identifying microplastics. In addition, the application of infrared techniques to identify microplastics in surface water samples of the Saigon - Dong Nai River was researched to find polymer types present in reality. There is an inference about their origin. Research results are the basis for researchers to consider choosing appropriate methods in research.

2. Materials and methods

2.1. Research process and structure diagram

The research process and structure diagram are shown in Figure 1. Figure 1 provides an overview of the study implementation process. We began by collecting analytical methods to identify microplastics and parameters from machinery and equipment manufacturers. We then synthesized, compared, and presented an overview and comparison of the strengths and limitations of each technique. After careful consideration, we chose a total attenuation Fourier transform infrared spectroscopy (ATR-FTIR) technique to study the polymers of microplastics in water samples of the river basin of Saigon - Dong Nai.

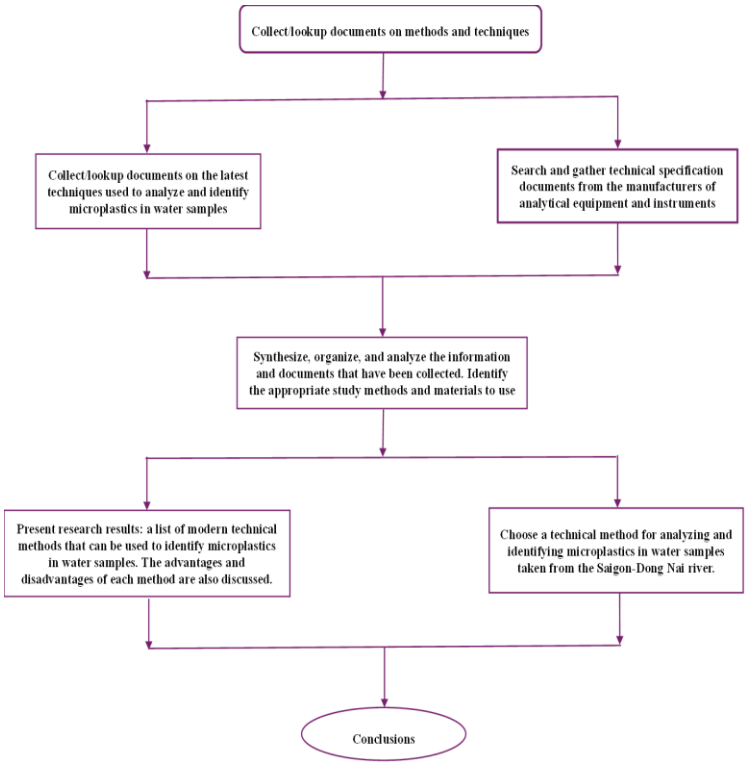

Figure 1. Flow chart outlining the process for implementing resear.

2.2. Study sites, sampling and surveys

The research was conducted at 18 locations in the Saigon - Dong Nai River basin in 2023. Of these, 13 locations are taken in the Saigon River branch from Dau Tieng lake to Ky Ha Rach junction (area near Soai Rap River) designated from S1 to S13 and 5 locations

are in the Dong Nai River branch from Tri An lake to Dong Nai-Soai Rap River mouth with symbols from D1 to D5 (Figure 2).

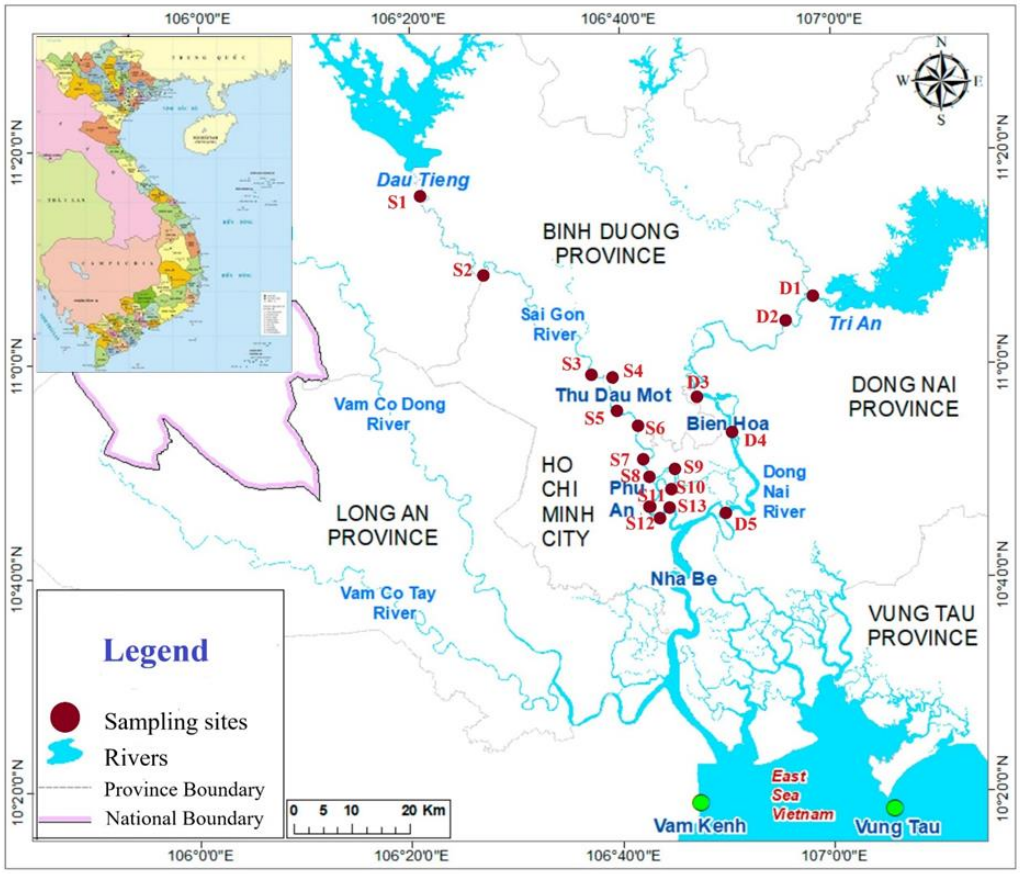

Figure 2. Sampling site.

2.3. Sampling method

Microplastic sampling in surface water was based on published methods of the National Oceanic and Atmospheric Administration [14]. The plankton net set (Neuston, 300 µm mesh) is attached to the Manta Trawl surface water microplastic sampling box (L×W×H = 30×30×15 cm) and anchored to the Neuston Katamaran floating buoy. The buoy is floated on the water surface to collect all solid objects floating on the surface water layer (from 0 to 15 cm) including plastic waste and other types of solids. A flow rate meter is also used to measure the water flow velocity at the time of sampling. Samples will be taken with a sampling time of approximately 30 minutes for each location. Once collected, the sample will be classified by hand to remove components > 5 mm in size. Then, these samples will be mixed together in a glass pot (washed and rinsed with 90% ethanol) to form a combined sample, and stored in a 2-liter glass jar with a tight lid. All water samples were transported to the nation lab and the southern institute of environment and circular economy (IECES) analysis room for analysis to identify microplastics.

2.4. Sample preparation methods before observation and identification techniques

To remove organic matter: 20 mL of 30 % H_2O_2 solution (hydrogen peroxide) and 0.05 M $FeSO_4$ (Fe II) solution were added to the device (beaker). The mixture was kept at room temperature for 5 minutes. Stir the mixture well and gently heat it on an electric stove (when you see air bubbles on the surface, take the cup off the stove and put it in a fume hood until the bubbles subside). Continue heating this mixture and adding 20 mL of 30% hydrogen peroxide until the reaction changes color from amber to light yellow.

To separate minerals and metals: Slowly add $ZnCl_2$ solution (d = 1.6 g/mL) into the sample mixture, stir well, then continue to drip $ZnCl_2$ solution into the tube to increase the density of the sample solution. This mixture is put into a centrifuge to completely separate microplastics from metals and minerals. Microplastics with low-density float to the surface of the $ZnCl_2$ solution (minerals and metals with a density greater than 1.4 g/mL sink to the bottom of the mixture). The detected polymer types can be used as the basis for similar inferences about their origin (Figure 3).

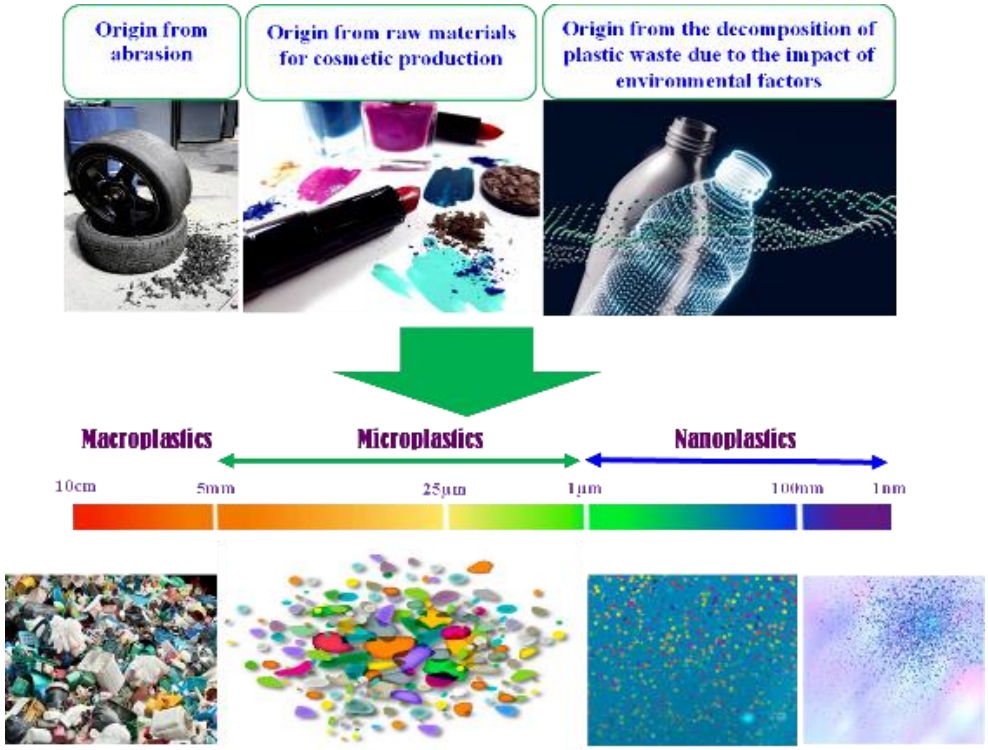

Figure 3. Size classification of microplastics and their relative origin.

2.4. Data analysis method

Calculation and statistical results are performed using Microsoft Excel Software and Spectrometer Technical Software.

3. Results and discussion

3.1. A review of analytical methods used in microplastics identification

3.1.1. Technique for identifying microplastics using electron microscope

Optical microscopy: Widely used to identify MPs in the > 100 µm range. Colorful microplastics can be easily identified using optical microscopy [15].

Electron Microscopy: Scanning Electron Microscopy (SEM), the sample was placed under a scanning electron microscope and all MPs present were counted and identified as flakes, pellets, fibers, films, or foams. SEM can provide very sharp, high-magnification images, even for very small particles, such as nanoplastics [16]; and transmission electron microscopes (TEM), devices that study solid-state microstructures, use magnetic lenses to produce magnified high-resolution images (up to millions of times), images may be produced on a fluorescent screen or on optical film, or recorded with a digital camera. Visual identification of microplastics via TEM may vary depending on the user. Additionally, the composition of additives such as Al, Ca, Mg, Na, and Si or antioxidants in microplastics is recorded [17]. Both have very high prices.

Gemstone microscope (polarizing microscope): it can be successfully used to identify polyethylene (PE). However, depending on the type of plastic, the structure of the plastic affects the transmission of polarized light when measuring. Therefore, this method is only suitable for measuring transparent microplastics [18].

3.1.2. Technique for identifying microplastics using thermal techniques

Differential scanning calorimetry (DSC): It is a thermal analysis technique that can confirm the physical properties of plastics. Because it is easy to melt MPs, it can only be used to identify some main types of microplastics such as PE and PP.

Thermogravimetric analysis (TGA): Equipment includes: a drying oven, micro-balance, temperature control system, and data acquisition. Confirmation of qualitative and quantitative information is performed by measuring the weight loss of the sample while heating at a specific rate under certain temperature conditions. But only polyethylene (PE) and polypropylene (PP) are clearly identified; polyvinyl chloride (PVC), polyethylene terephthalate (PET), and polyurethane (PU) are difficult to identify; polyamide (PA) and polyester (PES) were not identified.

Mass Spectrometry (Py-GC/MS - Pyrolysis Gas Chromatography/Mass Spectrometry): The chromatographic spectrum obtained from a sample is compared with the results of a known plastic standard to determine whether it must be plastic or not. This method can only determine PS well.

3.1.3. Microplastic identification technique using FTIR and Raman spectroscopy (Lazer)

Determining the type of microplastics in water samples was researched and analyzed using Fourier transform infrared spectroscopy (FTIR). When exposed to infrared radiation, microplastics absorb radiation at very specific wavelengths. The visual structure of the laboratory Fourier transform infrared spectroscopy (FTIR) analyzer used to analyze and determine the polymer type of microplastics in water samples is shown in Figure 4. The FTIR analysis technique for samples is a three-stage process: (i) The first stage is to record the FTIR spectrum of a new sample of MPs to obtain a basic FTIR trace; (ii) The second stage is to record the same FTIR spectrum of the used microplastic sample; (iii) The third and final stage is to subtract the new microplastic baseline, often called the new reference, from the used microplastic spectrum to obtain the difference spectrum.

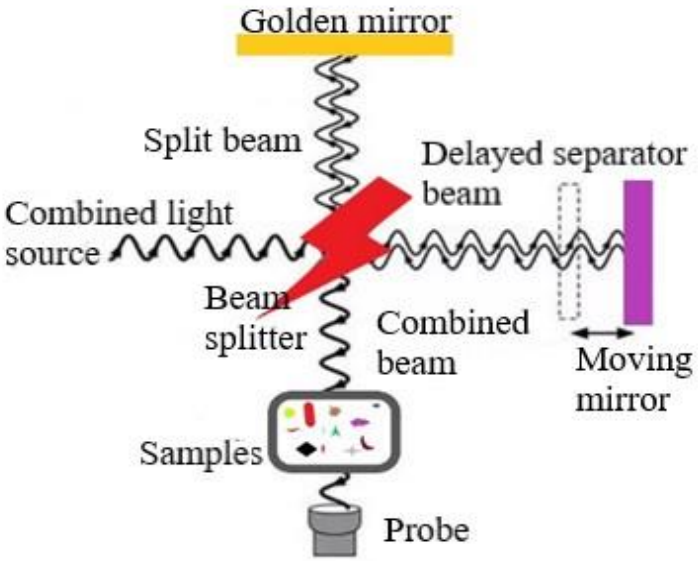

Figure 4. FTIR machine structure.

Both Raman and FTIR spectroscopy are capable of identifying microplastics. However, Raman spectroscopy has three distinct advantages when applied. The first is Raman spectroscopy which uses sub-micron wavelength lasers as the light source and, as such, is capable of resolving particles down to 1 µm or less. FTIR microscopy uses mid-infrared light as its source, resulting in a wavelength range that eliminates the ability to identify particles below 10 µm. The second is that, unlike IR systems, Raman microscopes are built around research-grade white light microscopes, making it easy to observe particles; The third is the

ease of sampling. There is no need to choose between transmission, reflection, and the required technical ATR sampling, the Raman laser system focuses on the sample, and the spectrum is simply obtained by collecting the scattered light.

3.2. Identification of polymer types in surface water samples of Saigon - Dong Nai River using FTIR spectroscopy technique with ATR accessories

Data collection and analysis of microplastic polymers is also automated through research using FTIR-ATR. Figure 5 shows the Nicolet™ iN10 MX FTIR imaging spectroscopy microscope system combined with ATR accessories used to analyze and identify the polymer types of microplastics in this study.

Figure 5. Nicolet iN10 MX FTIR imaging microscope with ATR accessories: a) FTIR machine; b) The FTIR machine is connected to a computer system to record detected data; c) Signal processing and display software; d) Proceed to identify polymer types in the sample.

Applying modern FTIR technology Nicolet iN10 MX with ATR accessories to be able to more accurately determine microplastic components, more effectively for small-sized microplastics that cannot be determined by means of visual. The resulting spectra are compared with spectral libraries to find the closest match and determine the chemical composition. A concordance of 70% or higher was considered sufficient for confirmation. Polymer types of microplastics in the samples were confirmed through spectral peak data collected when running the samples (Figure 6).

In principle, reflection is the easiest technique because it does not require sample preparation or interaction between the microscope and the specimen. However, it can distort the spectrum, which can complicate the identification of plastic components. Therefore, before observing using polymer-type identification techniques, it is necessary to remove impurities such as minerals and perform Fentonization of the sample.

The two main characteristics that need to be studied for microplastics are physical properties (size, shape, and color) and chemical properties (polymer type). Any method that reliably measures both is suitable for analyzing microplastics in samples. Because it is difficult to obtain both types of characteristics using only one analysis tool, a combination of methods can be applied. The minimum limit size of microplastics, as in this article, is 1mm – 5 mm, this is an important factor to consider when choosing identification, and qualitative methods. The optical microscope is an essential tool for measuring physical properties.

Optical microscopes can only classify microplastics by color, making it difficult to identify the polymer type like a spectroscopic microscope. However, infrared spectroscopy is expensive and requires a technician to operate professional training. Thermal technology faces many limitations and is limited in the list of polymer types and destroyed microplastic samples (Figure 7).

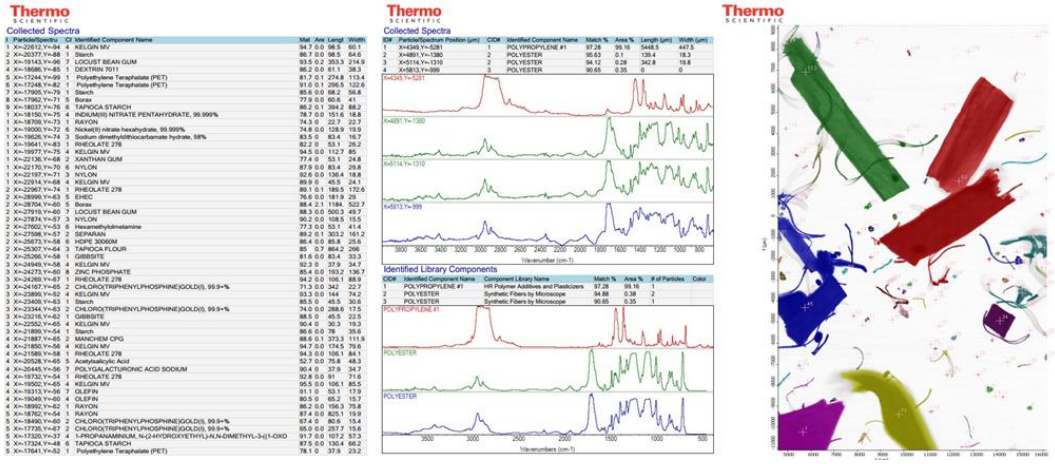

Figure 6. Interface of analysis results to determine the type of microplastics in water samples using the FTIR Transform Infrared Spectroscopy device on the screen.

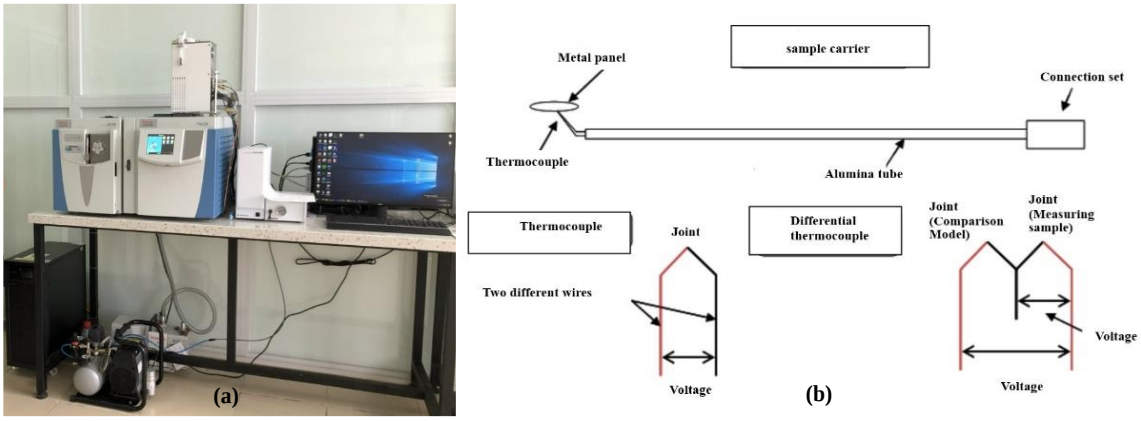

Figure 7. Thermal analysis techniques: a) Pyrolysi -GC-MS analysis identifies microplastics in the sample; b) Diagram of differential thermal analysis [19].

Pyrolysis -GC-MS analysis identifies isolated plastic particles from sediment samples such as PE, PP, PVC, PS, PA, PET, and chlorinated or chlorosulfonated PE. Thermal analysis provides an alternative to spectroscopy for the chemical determination of certain polymers. However, thermal analysis is a destructive method, which prevents further additional analysis of the sample. For large-sized microplastics that can be manipulated by hand (picking, counting...), magnifying microscopes and optical microscopes can be used because they will analyze the physical properties themselves along with a few additional tests (e.g. needle puncture) to determine the polymer type only relatively, lacking reliability. But if the size of the microplastic is < 1 mm and the minimum limit size is tens of micrometers, it is necessary to combine it with chemical analysis such as spectroscopy or thermal techniques to easily identify them according to the library of the system. Regarding convenience in processing, analysis time, and an abundant number of polymer types, choosing the μ-ATR-FTIR spectroscopy technique is the most optimal, especially for environmental samples.

If the minimum size is limited to a few micrometers, Raman (Lazer) spectroscopy should be a reliable technique for obtaining better spectra from particles < 20 μm in size. Although the μ-ATR-FTIR and Raman techniques are both very optimal, microplastics with too small

sizes can still be missed or information lost in complex environmental samples with many impurities such as colorants, glues, catalysts, labels..., even for many unknown types of polymers such as weathering polymers. These methods are not recommended for routine monitoring studies today because they are very expensive, the equipment storage and preservation environment needs to ensure limited indexes of room temperature and humidity. Dust-proof, and above all, it requires a skilled technician to operate it. FTIR and Raman spectroscopy are powerful analytical tools for identifying microplastics in aquatic environments. There are many solutions, from simple point-and-shoot devices to complex imaging systems. The choice of system depends on the size of the particles being studied, on which the analysis to be performed is performed and the level of automation required. This information is summarized in Table 1.

Table 1. Information about infrared spectrum analyzers.

		FTIR + ATR	**FTIR + Smart Spot ATR**	**Point-and-Shoot FTIR**	**FTIR + Imaging + ATR**	**Raman microscope (Lazer)**
Microplastic size	5 mm	✓				
	1 mm	✓				
	500 µm	✓	✓			
	100 µm		✓	✓	✓	
	10 µm		✓	✓	✓	✓
	1 µm					✓
Just set the template manually		✓	✓	✓		
Automated analysis					✓	✓
Not affected by sample fluorescence		✓	✓	✓	✓	
Relative cost		Low	Medium	Medium	Hight	Very Hight

Data collection and analysis can be automated through the use of a microscope equipped with a motorized stage and associated software. Automatic analysis of this image using software can generate information about the identity, number, and size of each individual microplastic. The first result, though, is that images can contain large amounts of redundant data. There may be only a small percentage of the image data set that contains information about particles, the rest is filtered. The approach chosen is situational dependent on: i) How many particles are analyzed?; ii) In stock?; iii) In what area? Therefore, these advanced techniques prioritize identification and detection research and are limited in quantitative research, determining the density, color, and size of microplastics.

3.3. Polymer types detected in surface water samples of the Saigon - Dong Nai River using the FTIR-ATR method

As a result of FTIR transform infrared spectroscopy analysis, the study discovered more than 60 polymer types from microplastics found in surface water samples of the Saigon - Dong Nai river. This result is shown in Figure 8. Polymer types found in the samples according to chemical origin: VINYL-based plastic accounts for 3.29%; ETHYLENE-based plastic accounts for 40.8%; MUF synthetic glue-based resin accounts for 0.16%; TEFLON plastic (PTEF) accounts for 7.06%; PROPYLENE plastic accounts for 10.3%; OLEFIN synthetic resin (HIDROCACBON) accounts for 1.37%; AMINO synthetic resin accounts for 1.22%; STYRENE plastic accounts for 1.52%; NYLON accounts for 42.14%; The remaining 3.86% is other types of polymers.

The findings highlight how microplastics are already present in the water of these two tributaries from a range of plastic products such as packaging, nets, and single-use products such as straws and masks. The density of PE, PP, and PVC is very small, from 0.90 to 0.95 $g.cm^{-3}$ [20].

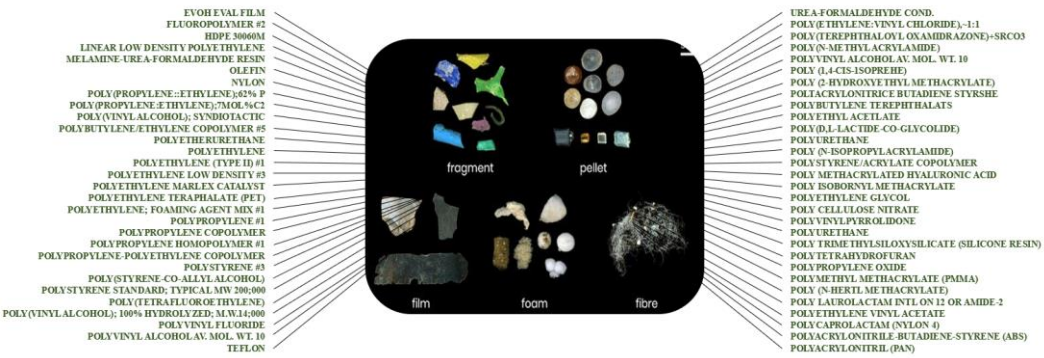

Figure 8. Polymer types detected in surface water samples of two branches of the Saigon and Dong Nai rivers.

They can float on the surface of river water, where the particles are then deposited on the sediment layer. Initial results of the study have identified microplastics present in the water environment. At the same time, the percentage of polymer-type radicals detected also represents a relative relationship from product to microplastic. Specifically, the NYLON plastic base belongs to the Polyamide industrial plastic group (PA plastic), with soft, smooth but waterproof properties, can withstand weather phenomena, and can resist natural influences such as mold or mildew insects, NYLON often produces artificial fiber products, doormats, tablecloths, raincoats, garbage bags, gloves, food wraps, and kitchen utensils,... these products have a high potential to decompose into fibrous and fragmented microplastics. In addition, PROPYLENE-based plastic is a hard, tough, and crystalline polymer thermoplastic produced from propene monomer (or propylene), often used to produce bottle caps, jars, and rice barrels, etc. that are difficult to decompose. If exposed to physical impacts and light environments that make them brittle and broken, they will mostly create microplastics in the form of hard pieces or granules. Similarly, ETHYLENE-based plastic is a flexible material that belongs to the polyolefin plastic group and plays an extremely important role in the plastic industry, producing many products for daily use such as food wrap, plastic straws, zip bags..., easily break and melt under sunlight and heat.

4. Conclusion

Different combinations of microplastic analysis methods will help identify microplastics in different complex environmental matrices. The need to identify microplastics from research projects are increasing, in many different environments such as water, air, and food to assess the risks and impacts of microplastics on natural ecosystems and human health, existing identification techniques need to be properly selected to reduce implementation time and effort. Although the optical microscope technique is simple, despite its low cost, it cannot identify microplastics. If the thermal technique is applied, it is limited because the polymer-type library is quite poor. After samples are analyzed using this technique, further experiments cannot be carried out because the microplastic sample is almost destroyed. Completely canceled and the price was also very expensive. By far the most popular spectroscopic technique for the analysis of plastics is total attenuation Fourier transform infrared spectroscopy (ATR-FTIR), a technique for the analysis of liquids. For samples smaller than 1mm, the ATR accessory can provide viewing and magnification capabilities, facilitating analysis of samples in the 1mm to 70 µm range. When the particle size drops below 100 µm, magnification is required.

There are two options, infrared microscopy and Raman microscopy (both are techniques also known as spectroscopic microscopy). For particles smaller than 10 µm, Raman is the preferred choice. Both FTIR and Raman are modern techniques but they are very expensive. In addition, the study has shown results on the presence of a variety of polymer types in the surface water of the two rivers Saigon and Dong Nai. FTIR imaging microscopy techniques

combined with ATR accessories, specifically the Nicolet™ iN10 MX FTIR imaging spectroscopy microscope, more than 60 polymer types were detected. In particular, the highest is NYLON origin accounting for 42.14%, and ETHYLENE origin accounting for 40.8%. These are the two main sources in the production of packaging products, artificial fibers, raincoats, garbage bags, gloves, food wrap, kitchen utensils, and straws... these are flexible plastics, soft and smooth, easily disintegrate when exposed to rain, wind and heat from the environment, especially sunlight. Therefore, this issue should also be considered when research on microplastics is carried out. When performing identification, in order not to confuse polymer types with similar materials, it is also necessary to pay attention to those features to distinguish them. In addition, research should continue to identify and isolate microplastics from environmental samples through the introduction development and updating of new polymer types into the library spectrum, which is a major limitation because it requires coordination. Coordinate with manufacturers and update software systems.

Author contributions: Developing research ideas: H.P., H.T.N.H.; Choosing research methods: H.P., H.T.N.H., T.N.N.; Data processing: H.T.N.H., T.T.M.H.; Sampling: H.T.N.H., T.N.N.; Writing draft of article: H.T.N.H., T.N.N.; Editing the article: H.P., H.T.N.H.

Acknowledgments: This research was conducted under the sponsorship of the research project Institute for Environment and Circular Economy in The South (IECES).

Declaration: The authors warrant that this article is their own work, has not been published elsewhere, and has not been copied from previous research; There are no conflicts of interest within the author group.

References

1. PlasticsEurope. Plastics - the Facts 2017: An analysis of european plastics production, demand and waste data. 70. Available online: https://search.issuelab.org/resource/plastics-the-facts-2017-an-analysis-of-european-plastics-production-demand-and-waste-data.html (Accessed February 2024).
2. Thompson, R.C.; Olsen, Y.; Mitchell, R.P.; Davis, A.; Rowland, S.J.; John, A.W.; McGonigle, D.; Russell, A.E. Lost at sea: where is all the plastic?. *Science* **2004**, *304*, 838. https://doi.org/10.1126/science.1094559.
3. Kershaw, P.; Turra, A.; Galgani, F. Guidelines for the monitoring and assessment of plastic litter in the ocean. GESAMP Reports and Studies, 2019, pp. 99. Available online: https://vidamarina.info/wp-content/uploads/gesamp2019.pdf.
4. Phu, H.; Han, H.T.N.; Thao, N.L.N. Plastic waste, microplastics in the Saigon – Dong Nai river basin, the risk of impacts on the health of people. *J. Hydro-Meteorol.* **2022**, *736(1)*, 14–27. https://doi.org/10.36335/VNJHM.2022(736(1)).14-27.
5. Klein, S.; Dimzon, I.K.; Eubeler, J.; Knepper, T.P. Analysis, occurrence, and degradation of microplastics in the aqueous environment. Springer International Publishing, Cham, 2018, pp. 51.
6. Loder, M.G.J.; Kuczera, M.; Mintenig, S.; Lorenz, C.; Gerdts, G. Focal plane array detector-based micro-fourier-transform infrared imaging for the analysis of microplastics in environmental samples. *Environ. Chem.* **2015**, *12(5)*, 563–581. https://doi.org/10.1071/EN14205.
7. Anger, P.; Esch, E.V.D.; Baumann, T.; Elsner, M.; Niessner, R.; Ivleva, N.P. Raman microspectroscopy as a tool for microplastic particle analysis. *Trac Trends Anal. Chem.* **2018**, *109*, 214–226. https://doi.org/10.13140/RG.2.2.15927.47524.
8. Dümichen, E.; Braun, U.; Senz, R.; Fabian, G.; Sturm, H. Assessment of a new method for the analysis of decomposition gases of polymers by a combining

thermogravimetric solid-phase extraction and thermal desorption gas chromatography mass spectrometry. *J. Chromatogr. A.* **2014**, *1354*, 117–128. https://doi.org/10.1016/j.chroma.2014.05.057.

9. Fischer, M.; Scholz-Bottcher, B.M. Simultaneous trace identification and quantification of common types of microplastics in environmental samples by pyrolysis-gas chromatography-mass 764 spectrometry. *Environ. Sci. Technol*. **2017**, *51*, 5052–5060. https://doi.org/10.1021/acs.est.6b06362.
10. Van Cauwenberghe, L.L.; Devriese, L.; Galgani, F.; Robbens, J.; Janssen, C.R. Microplastics in sediments: A review of techniques, occurrence and effects. *Mar. Environ. Res*. **2015**, *111*, 5–17. https://doi.org/10.1016/j.marenvres.2015.06.007.
11. Rocha-Santos, T.; Duarte, A.C. A critical overview of the analytical approaches to the occurrence, the fate and the behavior of microplastics in the environment. *Trac Trends Anal. Chem*. **2015**, *65*, 47–53. https://doi.org/10.1016/j.trac.2014.10.011.
12. Wagner, M.; Scherer, C.; Alvarez-Munoz, D.; Brennholt, N.; Bourrain, X.; Buchinger, S.; Fries, E.; Grosbois, C.; Klasmeier, J.; Marti, T.; Rodriguez-Mozaz, S.; Urbatzka, R.; Vethaak, A.D.; Winther-Nielsen, M.; Reifferscheid, G. Microplastics in freshwater ecosystems: what we know and what we need to know, Environ. *Sci. Eur*. **2014**, *26*, 1–9. https://doi.org/10.1186/s12302-014-0012-7.
13. Horton, A.A.; Walton, A.; Spurgeon, D.J.; Lahive, E.; Svendsen, C. Microplastics in freshwater and terrestrial environments: evaluating the current understanding to identify the knowledge gaps and future. *Sci. Total Environ*. **2017**, *586*, 127–141. https://doi.org/10.1016/j.scitotenv.2017.01.190.
14. National Oceanic and Atmospheric Administration. Microplastic marine debris fact sheet. 2008. Available online: https://marinedebris.noaa.gov/fact-sheets/microplastic-marine-debris-fact-sheet (Accessed February 2024).
15. Tunali, M.; Uzoefuna, E.N.; Tunali, M.M.; Yenigun, O. Effect of microplastics and microplastic-metal combinations on growth and chlorophyll a concentration of Chlorella vulgaris. *Sci. Total Environ*. **2020**, *743*, 140479. https://doi.org/10.1016/j.scitotenv.2020.140479.
16. Dehghani, S.; Moore, F.; Akhbarizadeh, R. Microplastic pollution in deposited urban dust, Tehran metropolis, Iran. *Environ. Sci. Pollut. Res. Int.* **2017**, *24(25)*, 20360–20371. https://doi.org/10.1007/s11356-017-9674-1.
17. Sabri, N.H.; Muhammad, A.; Abdul Rahim, N.H.; Roslan, A.; Abu Talip, A.R. Feasibility study on co-pyrolyzation of microplastic extraction in conventional sewage sludge for the cementitious application. Mater. *Today Proc*. **2021**, *46*, 2112–2117. https://doi.org/10.1016/j.matpr.2021.05.439.
18. Mossotti, R.; Dalla Fontana, G.; Anceschi, A.; Gasparin, E.; Battistini, T. Preparation and analysis of standards containing microfilaments/microplastic with fibre shape. *Chemosphere* **2021**, *270*, 129410. https://doi.org/10.1016/j.chemosphere.2020.129410.
19. REDSTAR. Manual document thermal analysis method. 2015. Available online: http://redstarvietnam.com/media/lib. (Accessed February 2024).
20. Claessens, M.; Meester, S.D.; Landuyt, L.V.; Clerck, K.D.; Janssen, C.R. Occurrence and distribution of microplastics in marine sediments along the Belgian coast. *Mar. Pollut. Bull*. **2011**, *62(10)*, 2199–2204. https://doi.org/10.1016/j.marpolbul.2011.06.030.

JOURNAL OF
HYDRO-METEOROLOGY

Research Article

Estimation of the virtual water trade of agricultural products between Vietnam and China

Huong Nguyen Thi Thu[1]*, Thu Pham Anh[1], Thao Vu Thi Ngoc[1]

[1] Department of Environmental Science and Technology, School of Chemistry and Life Sciences, Hanoi University of Science and Technology;
huong.nguyenthithu4@hust.edu.vn; thu.pa193452@sis.hust.edu.vn;
thao.vtn193450@sis.hust.edu.vn

*Corresponding author: huong.nguyenthithu4@hust.edu.vn; Tel.: +84–396915145
Received: 10 March 2024; Accepted: 08 April 2024; Published: 25 June 2024

Abstract: China not only serves as a significant trading partner for agricultural products with Vietnam but also holds a strategic position as an upstream neighbor in Vietnam's major river basins, thereby influencing the nation's water security. This research initially examines the Vietnam-China relationship through the lens of virtual water trade in agricultural goods, analyzing the period from 2010 to 2021. Findings reveal Vietnam's status as a virtual water deficit country vis-à-vis China, a trend that has been progressively worsening. Vietnam acted as a virtual water exporter during this period, exporting around 98 billion m3 to China while importing 10.96 billion m^3. Both nations share similarities in virtual water structure due to similar climatic conditions and technical advancement levels. In terms of product structure, Vietnam emerges as a strategic partner, predominantly supplying China with agricultural products derived from plants. However, this structure lacks balance and is primarily centered around a select few products such as soybean oil (constituting 20.77% of virtual water imports) and manioc starch (constituting 33.48% of virtual water exports). The virtual water trade between Vietnam and China reflects a negative net import, with both countries possessing renewable internal water freshwater resources per capita lower than the global average. While Vietnam currently supports China in addressing water scarcity challenges, diversifying export markets and optimizing the import-export framework with China can enhance Vietnam's resilience and contribute to long-term water sustainability. Consequently, prioritizing policies aligned with the virtual water perspective will empower Vietnam to effectively manage water scarcity, ensuring its future sustainability.

Keywords: Virtual Water Trade; Agriculture Products; Vietnam and China; Virtual Water Defcit.

1. Introduction

Vietnam is a country with a high average rainfall of 1000-4000 mm (2020) [1] and a dense river system with over 2,360 rivers having more than 10 km in length [2]. However, two-thirds of Vietnam's total water resources originate from abroad. If only considering renewable internal water resources, the amount of annual available water will be about 3,719 m^3 per capita in 2020, lower than the world average (5,500 m^3 per capita) [3]. Moreover, Vietnam is situated in a susceptible region positioned downstream of major transnational rivers, which are significantly impacted by upstream nations like Laos and China. Presently, there is a notable increase in the construction of large-scale hydroelectric dams upstream of the Mekong River, resulting in alterations to seasonal flows downstream. This phenomenon impacts the sediment load, triggers floods, and disrupts agricultural and fishery practices [4]. In Vietnam, the study computed the aggregate volume of virtual water expended on four

primary crops-rice, corn, coffee, and sugarcane illustrating that reliance solely on domestic water reservoirs would lead to severe water scarcity in regions such as the Red River Delta and the South Central Coast [5]. Consequently, prioritizing the regulation of water resources for Vietnam through inter-country policies to uphold water security emerges as a paramount task. Efforts to mitigate strain on potable water sources have been investigated and put into practical application. Since the 1980s, the notion of "Virtual Water", as introduced by the study [6] has been advocated to quantify the water consumption associated with various goods or food items, necessitating thorough investigation. This approach is regarded as a sustainable method for assessing a nation's water usage concerning goods and food items, thereby offering a clearer and more comprehensive understanding of water resource utilization issues. Addressing scarcity can be facilitated by importing commodities with substantial virtual water content from countries endowed with relatively abundant water resources, thus alleviating strain on local river basins [7].

The trade relationship between Vietnam and China has developed dramatically in the period 2010-2020 [8]. Subsequently, the trade dynamics and commerce between the two nations have fostered a robust relationship, establishing a connection between goods and food. China emerges as a crucial partner in the import-export domain for agricultural commodities, benefiting from Vietnam's geographical proximity, which facilitates reduced transit time and transportation expenses for agricultural products. Leveraging the ASEAN-China Free Trade Agreement (2002), Vietnam has secured tariff reductions for over 8,000 export items, encompassing agricultural products [9]. Hence, based on data from the General Statistics Office, China stands as Vietnam's primary trading partner, leading in both imports and exports. From 2010 to 2020, Vietnam's trade with China escalated from 17.8% to 24.4%, with indications suggesting a potential continuation of this upward trend [10]. Additionally, as per previous research in the period 2001-2014, Vietnam emerged as the leading provider of virtual water to China among nations engaged in the Trans-Pacific Partnership Agreement, including the US, through its exports about 2.72 billion m^3/year, while simultaneously ranking as the second-largest importer of such products from China within this group, accounting for 1.29 billion m^3 per year [11]. This indicates that Vietnam experiences a virtual water deficit in its trade dealings with China. Coupled with Vietnam's reliance on upstream countries for river basins as aforementioned, investigating the virtual water trade between Vietnam and China becomes an urgent priority. Previous reports on virtual water trade had also been carried out by many countries such as Malaysia [12], Spain [13], and the Nile basin [14] to manage water security for countries. Moreover, this represents a new research avenue that has not yet been explored in Vietnam.

The main purpose of the study is to clarify the virtual water trade relationship between China and Vietnam in the period from 2010 to 2021 by examining the specific water footprint of agricultural trade products derived from plants and animals for agricultural products which is the largest freshwater consumption in the world, accounting for about 70-95% [15]. The study seeks to provide an in-depth analysis of the China-Vietnam relationship through the lens of virtual water trade. Additionally, it will utilize the virtual water footprint of various product types to meticulously calculate and present data, shedding light on the trade dynamics between the two nations in terms of product composition and water footprint makeup, with a focus on water sustainability. Following the introduction, section 2 will outline the research methodology, section 3 will present the results and discussion, and section 4 will conclude the study.

2. Materials and Methods

2.1. Method of research

2.1.1. Virtual water calculation for agricultural products

Virtual water, also known as “embedded water” or “indirect water”, refers to the water that is concealed within the products, services, and processes consumed daily by individuals. Despite remaining unseen by the end-user, this water is expended throughout the entire value chain, enabling the creation of the respective product or service. Virtual water and water footprint both concern the water consumption in manufacturing, but the concept of water footprint has broader applications. While virtual water accounts for all water used in a product's production, the water footprint (WF) is the volume of water required to produce an agricultural product which is calculated as three components of water: green water footprint, blue water footprint, and grey water footprint. Additionally, we can evaluate whether a product’s water footprint aligns with local water resources and ecological conditions. The green water footprint pertains to the rainwater utilized during the production of an item, the blue water footprint relates to the surface and groundwater utilized (through evaporation). Additionally, the grey water footprint signifies water pollution, representing the volume of freshwater needed to absorb pollutants based on prevailing ambient water quality standards [5].

The virtual water amount for each crop is calculated based on the specific water needs of the crop and each country with the productivity of that crop [16]. The virtual water content of animal products is calculated based on the following factors: Virtual water content from consumed food, virtual water content from drinking water, and virtual water content from service water [17].

The amount of imported and exported virtual water will be calculated based on the water footprint of that product and that country's agricultural product trade as below:

$$VWF = CT \times WF \quad (1)$$

VWF (Virtual water flows) is the amount of virtual water calculated for products from the exporting country to the importing country or vice versa (m^3/year), CT (The agriculture product trade) is the import or export volume of product (kg/year), WF (water footprint) is the water footprint of that product (m^3/kg) [11].

In determining virtual water trade between Vietnam and China, essential data includes import/export quantities and the water footprint associated with each product. The water footprint of a single product varies across different countries. Therefore, to assess products exported from Vietnam, the study uses the datda of export quantity and water footprint of the Vietnam’s product, while the data of import quatity and water footprint of China is used for the imported products. The virtual water trade volume comprises the green water footprint, blue water footprint, and grey water footprint of the product.

2.1.2. Virtual water surplus and deficit

The concept of “Virtual Water” by [6] is a means to optimize water use through the import and export of virtual water between nations. Virtual water trade enables water-scarce countries to manage water consumption by importing water-intensive products, effectively transporting the water embedded in goods to alleviate scarcity pressure [18]. Conversely, nations abundant in water resources can capitalize on the resources they export [19]. Hence, exporting a product with substantial water usage to another nation constitutes exporting virtual water [16].

The trajectory of a nation's foreign trade can be delineated by its trade surplus and deficit. In international trade, a surplus occurs when a country’s exports surpass its imports within a defined period, whereas a deficit indicates the opposite scenario, thereby reflecting the international balance of payments. Conversely, the computation of virtual water contrasts with the principles of the international balance of payments. A surplus in virtual water trade occurs when a country’s total imported virtual water surpasses its exported volume, and conversely for a deficit. This delineates the equilibrium of water resources. By employing this methodology, we have acquired data on imported and exported virtual water flows

between Vietnam and China. If Vietnam's total imported virtual water from China exceeds its exported volume, Vietnam operates under a virtual water trade surplus, and vice versa for a deficit. This approach also facilitates an understanding of the virtual water trade status of individual nations [20].

2.1.3. The assessment indicator of trade partners

This analysis was conducted using two factors. The initial factor, net import, assesses the difference between virtual water imports and exports, indicating either surplus or deficit. The second factor, water abundance, compares each country's renewable internal freshwater resources per capita (measured in cubic meters) with the global average, revealing either abundance or scarcity. If a country's renewable internal freshwater resources per capita surpass the global average in a given year, it is considered abundant in water; conversely, it is deemed to face water scarcity. Renewable internal freshwater resource flows encompass the internal renewable resources within a country, such as internal river flows and groundwater replenished by rainfall. Through the application of these two factors, it becomes feasible to evaluate the dynamics of virtual water management between Vietnam and China.

2.2. Data

2.2.1. Data on import and export of products agriculture

Data on agricultural products exchanged between the two nations are drawn in the period from 2010 to 2021. The year 2010 marks the end of the 10-year socio-economic development strategy from 2001 to 2010, serving as a stary year for subsequent 10-year socio-economic development strategies as per Vietnam's planning [21]. Moreover, the HS code systems have changed since 2021. Therefore, the research has conducted a thorough investigation, providing further insights into the trade dynamics between Vietnam and China, particularly focusing on virtual water trade during the period 2010-2021. Data pertaining to agricultural trade has been meticulously researched and compiled by the International Trade Center (ITC) [22]. ITC provides international trade data by product and country including 99 product groups, this study will focus on agricultural product groups. The data from the ITC are estimated by the United Nations Statistics Unit (UNSD).

2.2.2. Data on the product's water footprint

The calculation will utilize trade data encompassing 339 plant products and 124 animal products. Each product will be assessed based on its green water, blue water, and grey water footprint. These footprint metrics are documented in Mekonnen and Hoekstra's Water Value Research Series No.47 and No. 48, published by the Institute for Water Education (UNESCO-IHE) [23, 24]. Specifically, green and blue water footprint data were computed utilizing the CROPWAT 8.0 model developed by the Food and Agriculture Organization of the United Nations (FAO). However, water footprint data for 126 crops were sourced from MICRA2000 due to the classification dependency on whether the crop is perennial or annual [23, 25]. The grey water factor is determined by the nitrogen fertilizer application and the actual crop yield. Report numbers 47 and 48 employ the 6-digit HS product code for reference; hence, this same code is utilized to retrieve the product quantity data from the International Trade Center (ITC).

2.2.3. Limitations

During the implementation of the study, certain limitations pertaining to data were identified. Specifically, some products changed their HS codes (Harmonized System codes) by the World Customs Organization (WCO) on a 5-year cycle. Consequently, numerous

codes became obsolete while new codes were introduced. For instance, the cotton seeds product with code 120720 was replaced by two separate products: Cotton seeds for sowing and cotton seeds, each assigned with distinct codes 120721 and 120729, respectively, in 2007 [22]. Therefore, the study presumed that new codes derived from the same old code would retain the same water footprint and maintain identical characteristics to the previous product code. Furthermore, the study assumes uniformity in the amount of water utilized for irrigation, planting schedules, and crop harvests at the national level, without considering regional disparities within a country. Another limitation lies in the calculation of the grey water footprint, which is based on nitrogen in fertilizers, with natural nitrogen concentrations assumed to be zero. Due to the unavailability of net fertilization rates, it was assumed that crops received an equal amount of nitrogen fertilizer per hectare planted across all grid cells within a country, with an average assumed leaching rate of 10% for fertilizers [23].

Additionally, Report 48 lacks virtual water data pertaining to agricultural products derived from aquatic sources, hence data on this product category was not included in the study. However, seafood represents a significant aspect of Vietnam's import and export activities, prompting consideration for future research on this matter. Furthermore, the study assumes that products are manufactured within their respective countries, and thus utilizes the water footprint of the corresponding country for each product [26].

Despite some limitations encountered in this study, it has successfully estimated the volume of virtual water exchanged between the two countries, aligning with the project's objectives. Moving forward, these identified limitations serve as valuable research avenues that the research team intends to explore in the future.

3. Results and discussion

3.1. Balance of virtual water trade between Vietnam and China

Figure 1.a shows that Vietnam is a virtual water exporter, with the amount of virtual water exported to China reaching 98 billion m^3, and imports from China reaching 10.96 billion m^3 during the entire period 2010-2021. The level of virtual water deficit is increasing rapidly in the period from 1.27 billion m^3/year in 2010 to 9.45 billion m^3/year in 2021 by 7.4 times [22]. The virtual water trade of agricultural products between Vietnam and China has exhibited a notable upward trend over the years, although a substantial disparity exists between exports and imports. From 2010 to 2013, there was a rapid increase in the volume of virtual water exported from Vietnam to China, followed by a stabilization period from 2014 to 2017, and then another increase from 2019 to 2021. Conversely, the amount of virtual water imported from agricultural products remained relatively stable throughout the period from 2010 to 2021. For instance, in 2010, the volume of virtual water imports was approximately 0.65 billion m^3/year, while the export volume was about 1.93 billion m^3. Thus by 2021, the disparity between virtual water imports and exports became more pronounced, with Vietnam importing approximately 1.19 billion m^3 and exporting about 10.65 billion m^3. This indicates a significant increase, approximately 8.9 times higher than the combined import and export volume in 2010. Particularly in 2018, the repercussions of the trade tensions between China and the US led to a general inclination among several nations, including China, to curtail imports of goods wherein Vietnam possessed a competitive edge.

The 2018 Vietnam Trade Report underscores this trend, revealing a notable decline in trade volume between the two countries for various commodities. Notably, there was a decrease in the import of rice (amounting to 638.3 million USD, a decrease of 33.4%) and natural rubber (1.37 billion USD, down by 5%) compared to the figures recorded in 2017 [27]. These agricultural products, which possess a substantial water footprint and constitute a significant portion of the trade volume, consequently experienced a sharp decline in virtual water exports in 2018. For instance, the export of cassava and cassava products totaled 2.15

million tons, marking a decline of 7.3% compared to 2017, with a high water footprint [23, 27]. Hence, the disparity in the quantity of virtual water exports between 2017 and 2018 amounted to approximately 2.57 billion m^3.

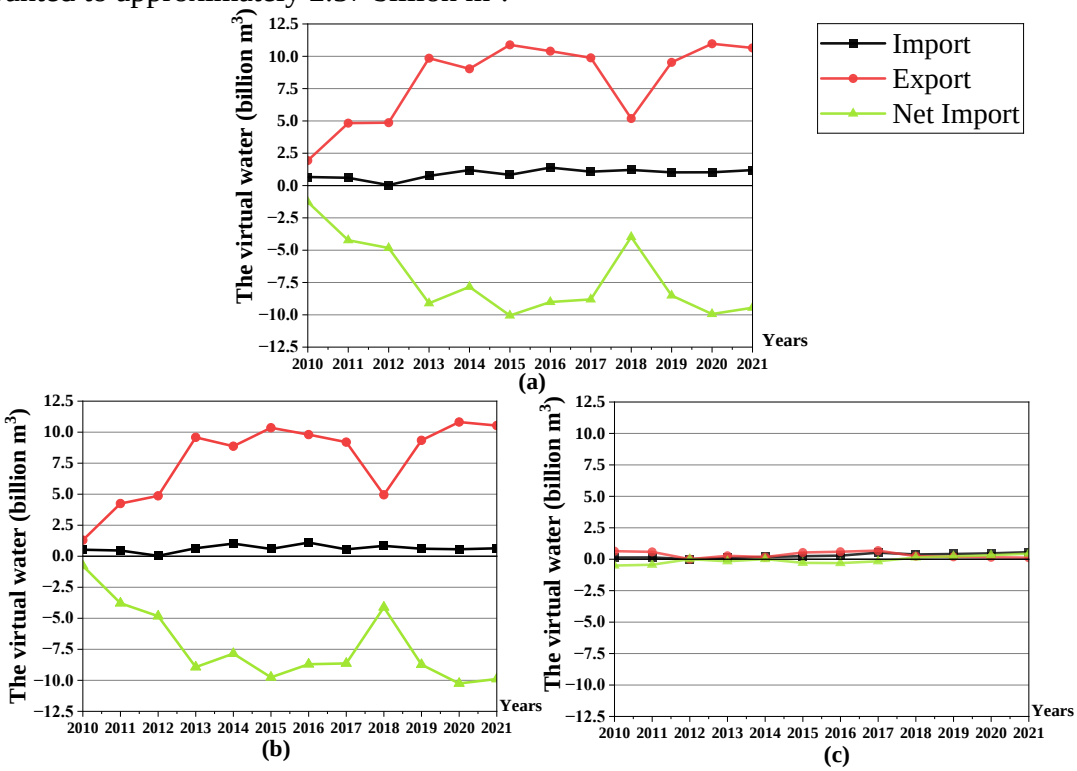

Figure 1. (a) The virtual water trade in agricultural products between Vietnam and China; (b) The virtual water trade in agricultural products derived from plants between Vietnam and China; (c) The virtual water trade in products derived from animals between Vietnam and China.

Vietnam excels in exporting agricultural products derived from plants, hence contributing significantly to the substantial virtual water volume (Figure 1b), exemplified by commodities such as "manioc starch" (32 billion m^3), "natural rubber latex, whether or not prevulcanised" (7.39 billion m^3), "fresh tamarinds, cashew apples, jackfruit, lychees, sapodilla plums, passion fruit, carambola, …" (4.05 billion m^3). The virtual water trade in animal products between Vietnam and China constitutes a notably smaller proportion compared to plant-based agricultural products. The volume of virtual water imported from plant-based agricultural products stands at 7.2 billion m^3, whereas that from animal products is 3.3 billion m^3, marking a 2.18 times difference (Figures 1b, 1c). Nonetheless, during the period from 2010 to 2021, the total virtual water imported from animal-based agricultural products also doubled from approximately 0.6 billion m^3 to 1.2 billion m^3. This underscores the trade relationship's heavy reliance on the exchange of plant-based agricultural products. Two primary factors contribute to the virtual water deficit in the Vietnam-China trade relationship. Firstly, Vietnam boasts a dominant position in exporting key commodities such as rice and cassava. Secondly, China's rapid economic growth has spurred urbanization, triggering population pressures and exacerbating land scarcity for cultivation [11].

3.2. Analysis of the component structure of virtual water trade

The virtual water trade relies on the exchange of three water components: green water, blue water, and grey water. Analyzing the trade involving these water components assists Vietnam in managing water resources effectively, mitigating water deficits in regions facing water scarcity. The general trend showed an increase of virtual water trade in both import and export between Vietnam and China over the years from 2010 to 2021 (Figures 2a_1, a_2,

b_1, b_2), especially a high volume of green water. However, net imports showed a deep downward trend during the study period (Figures $2a_3$, b_3, c_3). Beginning at approximately -1.27 billion m^3 of green water in 2010, the exchange of virtual water between Vietnam and China saw a notable increase, reaching about -9.45 billion m^3 by 2021, with a contribution of 8.8 billion m^3 from green water. From 2010 to 2021, Vietnam's imported virtual water structure consisted of 81.2% green water,6.4% blue water, and 12.4% grey water. Conversely, Vietnam's exported virtual water from China comprised 86.9% green water, 4.4% blue water, and 8.7% grey water. In the virtual water trade between Vietnam and China, green water, primarily sourced from rainfall, predominates in agricultural production. Given Vietnam's location in the tropical monsoon region with abundant rainfall ranging from 1000 to 4000 mm annually in 2020, rainwater serves as the primary source for irrigation [1].

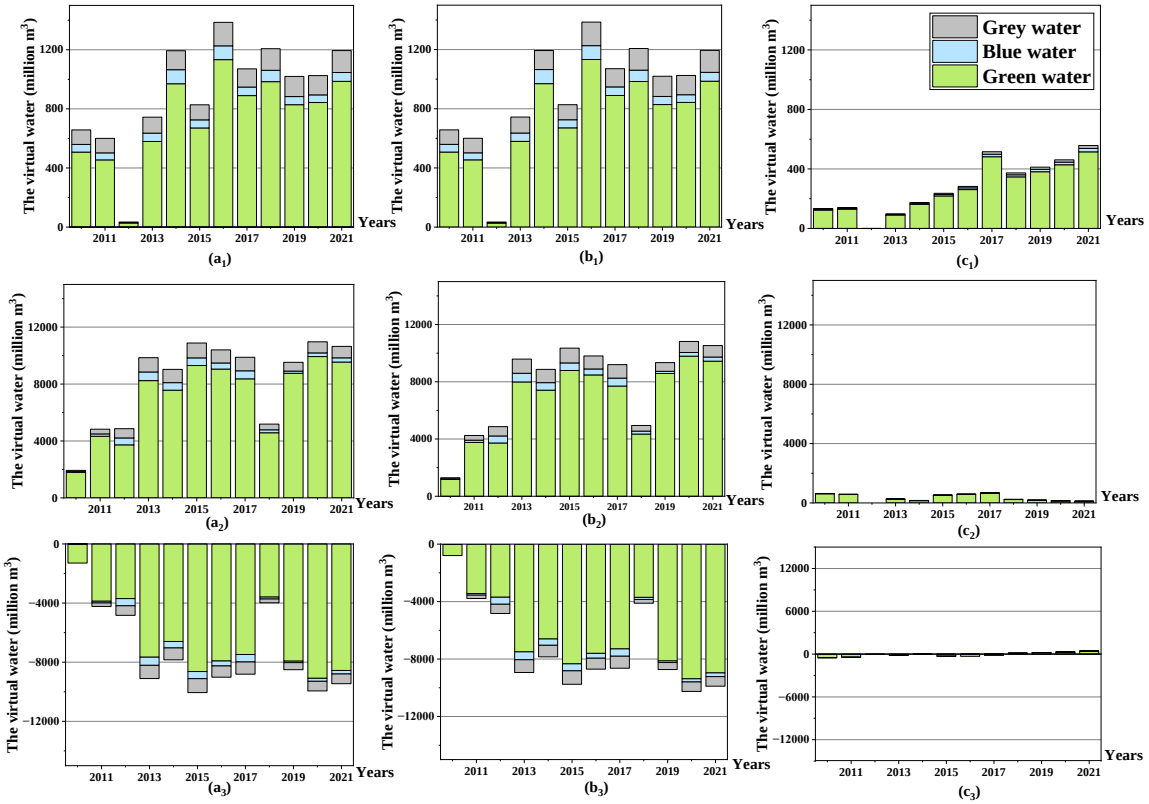

Figure 2. Virtual water structure of imports of all agricultural products (a_1), plant-derived agricultural products (b_1), and animal-derived agricultural products (c_1); Virtual water structure of exports of all agricultural products (a_2), and animal-derived agricultural products (b_2), and animal-derived agricultural products (c_2); Virtual water structure of net imports of all agricultural products (a_3), plant-derived agricultural products (b_3), and animal-derived agricultural products (c_3).

It is clear that the green virtualwater was the highest, and still trend increased in the period 2010-2021.There was a significant decrease in 2012 (Figures $2a_1$, $2b_1$) due to a lack of data recorded in the ITC [22]. The total import of virtual green water reached a peak at around 1.15 billion m^3 in 2016 (Figure $2a_1$). While the total export of virtual green water in 2016 is about 8.7 billion m^3 (Figure $2a_2$) including from plant products around 8.1 billion m^3 (Figure $2b_2$), and the virtual green water of animal products about is 0.6 billion m^3 (Figure $2b_3$). The difference can be explained by Vietnam's advantage in exporting agricultural products especially products derived from plants (Figure 1) and higher green water footprint products of Vietnam than that of China (Table 2). As for virtual water trade in agricultural products sourced from animals, the proportion of green countries accounts for more than the remaining countries. It can be explained due to the high water footpring such as leather "incl. parchment-dressed leather" of the whole hides and skins of bovine "incl.buffalo"... (HS code

410799) has a blue water footprint of 27,203 m^3/ton, 64 times higher than a green water footprint of 426 m^3/ton and 136 times higher than a grey water footprint of 200 m^3/ton [24]. The grey water footprint of agricultural and livestock products is reflected in the grey water footprint of crops in animal feed [23, 24]. Similar to animals products, the majority of the water footprint of plant products is also attributed to green water, for example "natural rubber latex, whether or not prevulcanised" (HS code 400110) of Vietnam has a green water footprint of 14,776 m^3/ton, 92 times higher than a blue water footprint of 160 m^3/ton and 23 times than a grey water footprint of 631 m^3/ton [23]. Furthermore, China encompasses four primary climate zones-desert, polar, continental, and warm temperate [12], resulting in an average rainfall in 2020 of approximately 694.8 mm lower than that of Vietnam. Consequently, China's green water volume is lower than that of Vietnam [28].

The disparity in grey water import and export volumes between China and Vietnam appears relatively minimal, suggesting a similar level of agricultural science and technology between the two nations. Generally, it can be seen that grey virtual water significantly increased both import and export in the period 2010-2021. The large difference in the amount of grey water embedded in the goods traded between China and Vietnam points to the difference in agricultural development levels between the two countries. In 2010, the total grey water import was approximately 0.09 billion m^3 and increased dramatically to 0.15 billion m^3 in 2021. While the total grey water export from Vietnam was about 0.08 billion m^3 in 2010, peaked at 1 billion m^3 in 2015, approximately 0.8 billion m^3 in 2021. Vietnam exhibits a slightly higher grey water footprint, indicating a greater loss of nitrogen fertilizer compared to Vietnam (Figures $2b_1$, $2b_2$).

Table 1. List of 10 agricultural products with the highest export/import virtual water flow between Vietnam and China in the period 2010-2021.

No	Import				Export			
	HS Code	**Product**	**Virtual water (Billion m^3)**	**Percent**	**HS Code**	**Product**	**Virtual water (Billion m^3)**	**Percent**
1	240110	Tobacco, unstemmed or unstripped	0.2	1.87%	071410	Fresh, chilled, frozen or dried roots and tubers of manioc "cassava", whether or not sliced, etc.	1.8	1.83%
2	410419	Hides and skins of bovine "incl. Buffalo" or equine animals, in the wet state "incl. wet-blue", etc.	0.26	2.42%	520299	Cotton waste (excl. yarn waste, thread waste and garnetted stock)	1.88	1.92%
3	170260	Fructose in solid form and fructose syrup, not containing added flavoring or coloring matter, etc.	0.27	2.46%	090111	Coffee (excl. roasted and decaffeinated)	1.95	2.00%
4	051199	Products of animal origin, n.e.s., dead animals, unfit for human consumption (excl. fish, crustaceans, etc.)	0.34	3.12%	170199	Cane or beet sugar and chemically pure sucrose, in solid form (excl. cane and beet sugar containing, etc.	2.22	2.26%
5	110900	Wheat gluten, whether or not dried	0.36	3.29%	410419	Hides and skins of bovine "incl. buffalo" or equine animals, in the wet state "incl. wet-blue", etc.	2.92	2.98%
6	100610	Rice in the husk, "paddy" or rough	0.37	3.42%	081090	Fresh tamarinds, cashew apples, jackfruit, lychees, sapodilla plums, passion fruit, carambola, etc.	4.05	4.13%

No	Import				Export			
	HS Code	Product	Virtual water (Billion m^3)	Percent	HS Code	Product	Virtual water (Billion m^3)	Percent
7	110710	Malt (excl. roasted)	0.41	3.78%	100640	Broken Rice	5.21	5.31%
8	170220	Maple sugar, in solid form, and maple syrup (excl. flavored or colored)	0.76	6.96%	400110	Natural rubber latex, whether or not prevulcanised	7.39	7.54%
9	410799	Leather "incl. parchment-dressed leather" of the portions, strips or sheets of hides and skins, etc.	2.16	19.69%	100630	Semi-milled or wholly milled rice, whether or not polished or glazed	27.06	27.61%
10	230400	Oilcake and other solid residues, whether or not ground or in the form of pellets, resulting, etc.	2.28	20.77%	110814	Manioc starch	32.81	33.48%

The proportion of the blue water footprint remains relatively small in both imports and exports of animal and plant products. Specifically, in 2010, the volume of agricultural products derived from plants exported with blue water was approximately 0.36 billion m^3 less than the volume of imported products, which contained around 0.46 billion m^3 of blue water. Additionally, animals imported accounted for approximately 0.13 billion m^3 of blue water, whereas the exported volume was around 0.07 billion m^3. The variation between animals and plants arises from the greater number of plant products, totaling 372, compared to animal products, which amount to 124.

Overall, there is not a substantial variation in the proportion of virtual water components over the years. Green water comprises the biggest share, followed by grey water and blue water. Consequently, the percentage breakdown of virtual water import and export for agricultural products between Vietnam and China remains relatively constant.

3.3. Analysis of product structure

During the study period spanning from 2010 to 2021, Vietnam imported approximately 0.05 billion tons of goods from China, while exporting around 0.43 billion tons of agricultural products [21]. This is equivalent to 10.6 billion m^3 of virtual water imported and 97.9 billion m^3 of virtual water exported from Vietnam to the Chinese market.

Vietnam mainly imports agricultural products derived from plants, such as "oilcake and other solid residues, whether or not ground or in the form of pellets, resulting", which accounts for the largest proportion of virtual water at approximately 2.28 billion m^3, constituting 20.77% of the total virtual water import (Table 1). Following "oilcake and other solid residues, whether or not ground or in the form of pellets, resulting" are "maple sugar, in solid form, and maple syrup (excl. flavored or colored)", "malt (excl. roasted)", and "rice in the husk, "paddy or rough", accounting for 6.96%, 3.78%, and 3.42% of the total respectively [23]. Furthermore, the animal product with the highest virtual water proportion in imports is leather "incl. parchment-dressed leather" of the portions, strips or sheets of hides and skins ..." (HS code 410799), amounting to 19.69%, equivalent to 2.16 billion m^3, owing to its high water footprint of 18,628 m^3/ton [24].

Table 2. Variations in the virtual water footprint of individual products between Vietnam and China.

No.	HS code	Product	China (m^3/ ton)			Vietnam (m^3/ ton)		
			Green	Blue	Grey	Green	Blue	Grey
1	230400	Oilcake and other solid residues, whether or not ground or in the form of pellets, resulting	2,114	207	181	2,355	0	308

No.	HS code	Product	China (m^3/ ton)			Vietnam (m^3/ ton)		
			Green	Blue	Grey	Green	Blue	Grey
2	170220	Maple sugar, in solid form, and maple syrup (excl. flavoured or colored)	1,436	54	261	1,853	288	220
3	110710	Malt (excl. roasted)	761	39	194	0	0	0
4	100610	Rice in the husk, "paddy" or rough	549	246	215	1,026	161	205
5	51199	Products of animal origin, n.e.s., dead animals, unfit for human consumption (excl. fish, crustaceans, etc.	80,777	1,412	2,324	87,892	2,092	1,311
6	110814	Manioc starch	1,325	0	293	2,256	0	162
7	100630	Semi-milled or wholly milled rice, whether or not polished or glazed	792	355	310	1,480	232	295
8	400110	Natural rubber latex, whether or not prevulcanised	5,971	359	1,016	14,776	160	631
9	100640	Broken rice	820	367	321	1,531	240	306
10	81090	Fresh tamarinds, cashew apples, jackfruit, lychees, sapodilla plums, passion fruit, carambola, etc.	2,860	90	999	920	0	24

Vietnam's forte lies in exporting plant-derived agricultural products to China, including cassava, rice, rubber, coffee, and fresh fruits. Among these, manioc starch products contribute significantly to the virtual water exported to China, representing 32.8 billion m^3 or 33.48% of the total exported virtual water volume. This prominence is attributed to Vietnam's substantial cassava exports to the Chinese market, with an export volume of approximately 2.26 million tons in 2019 [29] coupled with its substantial water footprint of 2,418 m^3/ton [23]. Additionally, other agricultural products also hold a considerable share, such as "semi-milled or wholly milled rice, whether or not polished or glazed", "natural rubber latex, whether or not prevulcanised", and "fresh tamarinds, cashew apples, jackfruit, lychees, sapodillo plums, passion fruit, carambola, etc.", accounting for 27.61%, 7.54%, and 4.13%, respectively. As for animal-derived agricultural products, wet hides of buffaloes, cows, or horses dominate the export proportion at about 2.98%, with a water footprint of 18,181 m^3/ton.

It is clearly seen from Table 2 that the water footprint of the same product varies between. For instance, for "manioc starch", Vietnam's green, blue, and grey water footprints are 2,256; 0; 162 (m^3/ton), whereas China's green, blue, and grey water footprints are 1,325; 0; 293 (m^3/ton). This disparity stems from differences in national productivity, crop varieties, and local climate, as well as varying agricultural practices between Vietnam and China [23, 24]. Henceforth, Vietnam must contemplate the importation of products characterized by high water footprints while restricting the export of items with substantial water footprints. This strategic approach will ultimately aid Vietnam in alleviating freshwater strain in local regions and guaranteeing water security through prudent product utilization.

The water footprint of animals typically exceeds that of plants due to three key factors: food conversion efficiency, feed composition, and food origin. Higher food conversion efficiency results in less food required for the animal and reduced water wastage during feed production. Feed composition is primarily determined by the types of plants used as animal feed, with the ratio of grain to soybean meal being a key consideration for chickens and pigs. Moreover, the origin of animal feed varies among countries due to regional climate conditions and agricultural practices [22]. As an illustration, consider the export of "hides and skins of bovine "incl. buffalo" or equine animals, in the wet state "incl. wet-blue" (HS

code 410419), which amounts to a total volume of 0.02 million tons, equivalent to 0.26 billion m^3. In contrast, the export volume of "fructose in solid form and fructose syrup, not containing added flavoring or coloring matter …" (HS code 170260) is 0.15 million tons, also equivalent to 0.26 billion m^3. Therefore, Vietnam should also consider the virtual trade between plant-derived and animal-derived agricultural products.

In summary, the water footprint of each country is determined by its unique climate, precipitation patterns, and technological advancement, resulting in varying green, blue, and grey water footprints for each type (Table 1). Nations grappling with water issues ought to contemplate importing water-intensive products from regions endowed with relatively abundant water resources to alleviate strain on local water reservoirs [6].

3.4. Analysis of trading partners

The issue of water scarcity is exacerbated due to prolonged droughts or population expansion, resulting in heightened water demands [6]. Virtual water trade is regarded as a viable solution to alleviate the strain on water scarcity while also safeguarding food security and conserving resources [10]. Analyzing trading partners enables Vietnam to gain a comprehensive understanding of its role and responsibilities within the global distribution of virtual water trade.

In evaluating the virtual water trade policy between Vietnam and China, it is crucial to account for two pivotal factors: net imports and the abundance of renewable internal freshwater resources per capita (m^3) as data from The World Bank. For instance, the world average renewable freshwater resources in 2020 were recorded at 5,500 m^3/capita/year, while Vietnam and China reported figures of 3,719 m^3/capita/year and 1,993 m^3/capita/year, respectively [3]. Thus, Vietnam and China are both considered countries with serious water scarcity. The virtual water trade between Vietnam and China entails negative net imports, and China exhibits a water potential below the global average (5,500 m^3/capita/year). Consequently, China receives virtual water trade assistance from Vietnam, as indicated in Table 3.

Table 3. Analysis of trading partners based on net import and water abundance.

Country	Net import (Vietnam)	Water abundance 2020 (m^3/capita/year)	World average (m^3/capita/year)
China	-87.05 billion m^3	1,993	**5,500**
Vietnam	-	3,719	

In general, Vietnam is supporting China in addressing water scarcity issues, but moving forward, Vietnam must refine its import and export strategies concerning agricultural virtual water. Continued expansion of exports to China over time may disadvantage Vietnam and exacerbate water scarcity problems. Therefore, increasing imports of products with high water footprints can assist Vietnam in mitigating water and environmental resource shortages.

4. Conclusion

Vietnam and China are two countries with a close and comprehensive relationship. There have been many studies conducted to explore this relationship from a political and economic perspective, but there is still a lack of research conducted from the perspective of water security. Therefore, the study is conducted comprehensively on virtual water trade between Vietnam and China to better understand from a new perspective. Furthermore, this study presents virtual water flows between two countries considering a full range of factors including trade status, product structure, water footprint structure, and trading partner

assessment. From there, it can help Vietnam have policies to adjust the management of trade structures from the perspective of saving water and promoting sustainable use of water resources.

The research findings indicate a significant interconnection in water management between China and Vietnam. China experiences a virtual water deficit sourced from Vietnam through agricultural product imports spanning the period from 2010 to 2021, with a projected upward trajectory in the future. Nevertheless, China is concurrently pursuing a strategy to transition from a net importer to a net exporter in agricultural trade by the year 2050 [30]. Moreover, the virtual water structure of the two countries is similar due to similarities in climatic conditions and levels of scientific and technological advancement in agricultural production. Nonetheless, certain agricultural products, such as cassava, exhibit a higher water footprint in Vietnam compared to China, yet are exported in significant quantities. This necessitates considerations for adjustments in import-export dynamics between regions, particularly for specific products, notably those among the top 10 imports and exports. Additionally, the product structure between the two countries lacks balance, with a predominant focus on certain items like soybean oil (imported) and cassava (exported). Notably, Vietnam contributes significantly to addressing water scarcity through virtual water exports, which are nearly nine times higher than its imports from 2010 to 2021, despite both Vietnam and China possessing considerable potential. However, their domestic water recycling rates are lower than the global average. Thus, it is imperative for Vietnam to prioritize the implementation of policies aimed at mitigating water scarcity by adapting the import-export framework according to the virtual water perspective in the near future.

Author contributions: Developing research ideas: H.N.T.T.; Choosing research methods: H.N.T.T., T.P.A., T.V.T.N.; Data processing: H.N.T.T., T.P.A., T.V.T.N.; Sampling: T.P.A., T.V.T.N.; Writing draft of article: H.N.T.T., T.P.A., T.V.T.N.; Editing the article: H.N.T.T., T.P.A.

Declaration: The authors warrant that this article is their own work, has not been published elsewhere, and has not been copied from previous research; There are no conflicts of interest within the author group.

References

1. Ministry of Natural Resources and Evironment. The 2020 climate summary. Vietnam Institute of Meteorology, Hydrology and Climate Change, 2021.
2. Water Environment Partnership in Asia. Vietnam overview. 2024. Available online: https://wepa-db.net/database/vietnam (Accessed 26 March 2014).
3. World Bank. Renewable internal freshwater resources per capita (cubic meters). Food and Agriculture Organization, AQUASTAT data. Available from: https://data.worldbank.org/indicator/ER.H2O.INTR.PC (Accessed 14 March 2023).
4. Kuenzer, C.; Campbell, I.; Roch, M.; Leinenkugel, P.; Tuan, V.Q.; Dech, S. Understanding the impact of hydropower developments in the context of upstream–downstream relations in the Mekong river basin. *Sustainability Sci.* **2013**, 8, 565–584.
5. Ngo, T.T.; Le, N.T.; Hoang, T.M.; Luong, D.H. Water scarcity in Vietnam: a point of view on virtual water perspective. *Water Resour. Manage.* **2018**, *32*, 3579–3593.
6. Allan, J.A. Fortunately there are substitutes for water otherwise our hydro-political futures would be impossible. Priorities for Water Resources Allocation and Management. Overseas Development Administration, London, 1993, 13–26.
7. Allan, J.A. Water stress and global mitigation: water food and trade. Arid Lands Newsletter, 1999, pp. 45.
8. Chuong, N.A. The problem of imbalance in Vietnam-China economic relations in the period 2010-2020. *VN J. Social Sci. Humanit*. **2022**, *8(4)*.
9. My, N.T. Analysis of Vietnam's agricultural exports to China through trade indicators. *Econ. Manage*. **2023**, *175*, 28–35.

10. General Statistics Office of Vietnam. Vietnam Import-Export Report 2010. Ministry of Industry and Trade, 2011.
11. Zhang, Y.; Zhang, J.; Wang, C.; Cao, J.; Liu, Z.; Wang, L. China and trans-pacific partnership agreement countries: estimation of the virtual water trade of agricultural products. *J. Cleaner Prod.* **2017**, *140*, 1493–1503.
12. Hess, T. Estimating green water footprints in a temperate environment. *Water* **2010**, *2(3)*, 351–362.
13. Duarte, R.; Pinilla, V.; Serrano, A. The effect of globalisation on water consumption: A case study of the Spanish virtual water trade, 1849–1935. *Ecol. Econ*. **2014**, *100*, 96–105.
14. Zeitoun, M.; Allan, J.T.; Mohieldeen, Y. Virtual water "flows" of the Nile Basin, 1998–2004: A first approximation and implications for water security. *Global Environ. Change*. **2010**, *20(2)*, 229–242.
15. FAO. Water for sustainable food and agriculture. A report produced for the G20 Presidency of Germany, 2017. Available online: https://www.fao.org/3/i7959e/i7959e.pdf?fbclid=IwAR32hcMJoBi6cmDh06GCPplWTrJ1jA5Xx-FN6QpbbLUkyaj4sV0lJ0UC5r4 (Accessed 2017).
16. Ay, H. Virtual water trade: A quantification of virtual water flows between nations in relation to international crop trade. Proceedings of the International Expert Meeting on Virtual Water Trade 12, Delft, 2003.
17. Chapagain, A.K.; Hoekstra, A. Virtual water flows between nations in relation to trade in livestock and livestock products. UNESCO-IHE Institute for Water Education, Delft, 2003, 13, pp. 158.
18. Oki, T.; Kanae, S. Virtual water trade and world water resources. *Water Sci. Technol.* **2004**, *49(7)*, 203–209.
19. Hoekstra, A.Y.; Hung, P.Q. Virtual water trade. Proceedings of the International Expert Meeting on virtual water trade. 2003.
20. Zhang, M.; et al. Virtual water flows and drivers in the international trade of agricultural products of the regional comprehensive economic partnership. *Water Sci. Technol.* **2024**, *89(3)*, 730–744.
21. Socio-economic information of 2010. 2011. Available online: https://vietnam.gov.vn/2010/socio-economic-information-of-2010-1695145.
22. International Trade Center. International Trade in Goods Statistic by Product Group. 2024. Available online: https://intracen.org/ (Accessed 30 March 2024).
23. Mekonnen, M.M.; Hoekstra, A.Y. The green, blue and grey water footprint of crops and derived crop products. *Hydrol. Earth Syst. Sci.* **2011**, *15(5)*, 1577–1600.
24. Mekonnen, M.; Hoekstra, A.Y. The green, blue and grey water footprint of farm animals and animal products. *Ecosystems* **2012**, *15*, 401–415.
25. Portmann, F.T.; Siebert, S.; Döll, P. MIRCA2000–Global monthly irrigated and rainfed crop areas around the year 2000: A new high-resolution data set for agricultural and hydrological modeling. *Global Biogeochem Cycles* **2010**, *24(1)*, GB1011.
26. Hoekstra, A.Y.; Mekonnen, M.N. The water footprint of humanity. Proceedings of the National Academy of Sciences, **2012**, *109(9)*, 3232–3237.
27. General Statistics Office of Vietnam. Vietnam import-export report 2018. Ministry of Industry and Trade, 2019.
28. Li, W.; Zhao, S.; Chen, Y.; Wang, Q.; Ai, W. State of China's climate in 2020. *Atmos. Oceanic Sci. Lett*. **2021**, *14(4)*, 100048.
29. General Statistics Office of Vietnam. Vietnam import-export report 2019. Ministry of Industry and Trade, 2020.
30. Zhuo, L.; Mekonnen, M.N.; Hoekstra, A.Y. Consumptive water footprint and virtual water trade scenarios for China–With a focus on crop production, consumption, and trade. *Environ. Int.* **2016**, *94*, 211–223.

JOURNAL OF
HYDRO-METEOROLOGY

Research Article

Longshore sediment transport rate at a pocket beach in Phu Quoc City, Kien Giang Province, Vietnam

Nguyen Anh Huy[1], Tran Van Ty[2], Dinh Van Duy[2]*, Pham Tan Dat[2], Truong Khai Man[2], Nguyen Tran Tan Dat[3] and Quach Van Choi[4]

[1] Department of Agriculture and Rural Development of Dong Thap province; huym4222007@gstudent.ctu.edu.vn
[2] Faculty of Water Resource Engineering, College of Engineering, Can Tho University; tvty@ctu.edu.vn; datb2004702@student.ctu.edu.vn; manb2004706@student.ctu.edu.vn
[3] Seu Do Solutions Limited Liability Company; nguyentrantandat1113@gmail.com
[4] Kim Long Ca Mau Limited Liability Company; kimlongbuild@gmail.com

*Corresponding author: dvduy@ctu.edu.vn; Tel.: +84–906975999
Received: 12 March 2024; Accepted: 09 April 2024; Published: 25 June 2024

Abstract: This study conducts a critical examination of the Longshore Sediment Transport Rate (LSTR) along Cua Can Beach in Phu Quoc City, Kien Giang Province. This notable pocket beach is characterized by its natural beauty and burgeoning tourist developments. The escalating construction of tourist facilities and resorts in close proximity to the shoreline, without considering beach morphological changes, poses a significant threat to the coastal integrity and sustainable development of the region. In response to this concern, our research aims to estimate the LSTR on the west coast of Phu Quoc to advocate for informed coastal engineering management and sustainable development strategies. Employing an integrated methodology that combines remote sensing with a simplistic one-line model, this study provides a comprehensive assessment of sediment dynamics along Cua Can Beach. The findings reveal consistent annual sediment transport from south to north, with an estimated quantity ranging from 5,000 to 20,000 m^3 per year.

Keywords: Phu Quoc; LSTR; Google earth; Satellite image; Shoreline change; One-line model.

1. Introduction

Phu Quoc, known as the “Pearl Island” for its natural beauty, is the first island city of Vietnam and a renowned tourist destination in the southwest of the country. Owing to significant socio-economic advancements over the past decade, this island city has witnessed extensive development of tourist infrastructure [1], such as resorts and bungalows, along its coastline. However, these projects have exerted considerable pressure on the coastal environment, as evidenced by several studies in recent years [2]. Although numerous studies have explored coastal engineering aspects along Phu Quoc Island’s shoreline, there has been scant literature on the Longshore Sediment Transport Rate (LSTR) up to now. Given the critical importance of LSTR for coastal engineering projects and management [3–15], this study seeks to estimate the LSTR at a specific coastal cell (Cua Can Beach) on Phu Quoc Island. This estimation will provide vital data for future coastal management endeavors on the island. To estimate the LSTR along Cua Can Beach, we employed an integrated approach combining remote sensing [16] and a simplified model for shoreline change, known as the One-line model [17]. This study offers essential data, namely the LSTR, for the sustainable management of beaches on Phu Quoc Island, a key city in the southwest of Vietnam.

2. Materials and Methods

2.1. Study area

Cua Can Beach, nestled on the western shores of Phu Quoc Island, exemplifies the typical pocket beach, shaped and sustained by the sediments delivered by the Cua Can River. Phu Quoc, celebrated as Vietnam's first island city, has garnered international acclaim as a prime tourist destination, largely due to its array of pristine and enchanting beaches. Among these, Cua Can Beach stand out for its unique geographical and morphological characteristics, owed in no small part to the vital contributions of the Cua Can River. Originating from the Chua Mountain, the Cua Can River meanders through a course of 28.75 kilometers before it culminates its journey at the western sea, at the Cua Can River mouth. The river's catchment area spans an expansive 147 square kilometers, acting as a crucial source of sediments that shape the coastal landscape of Cua Can Beach [18].

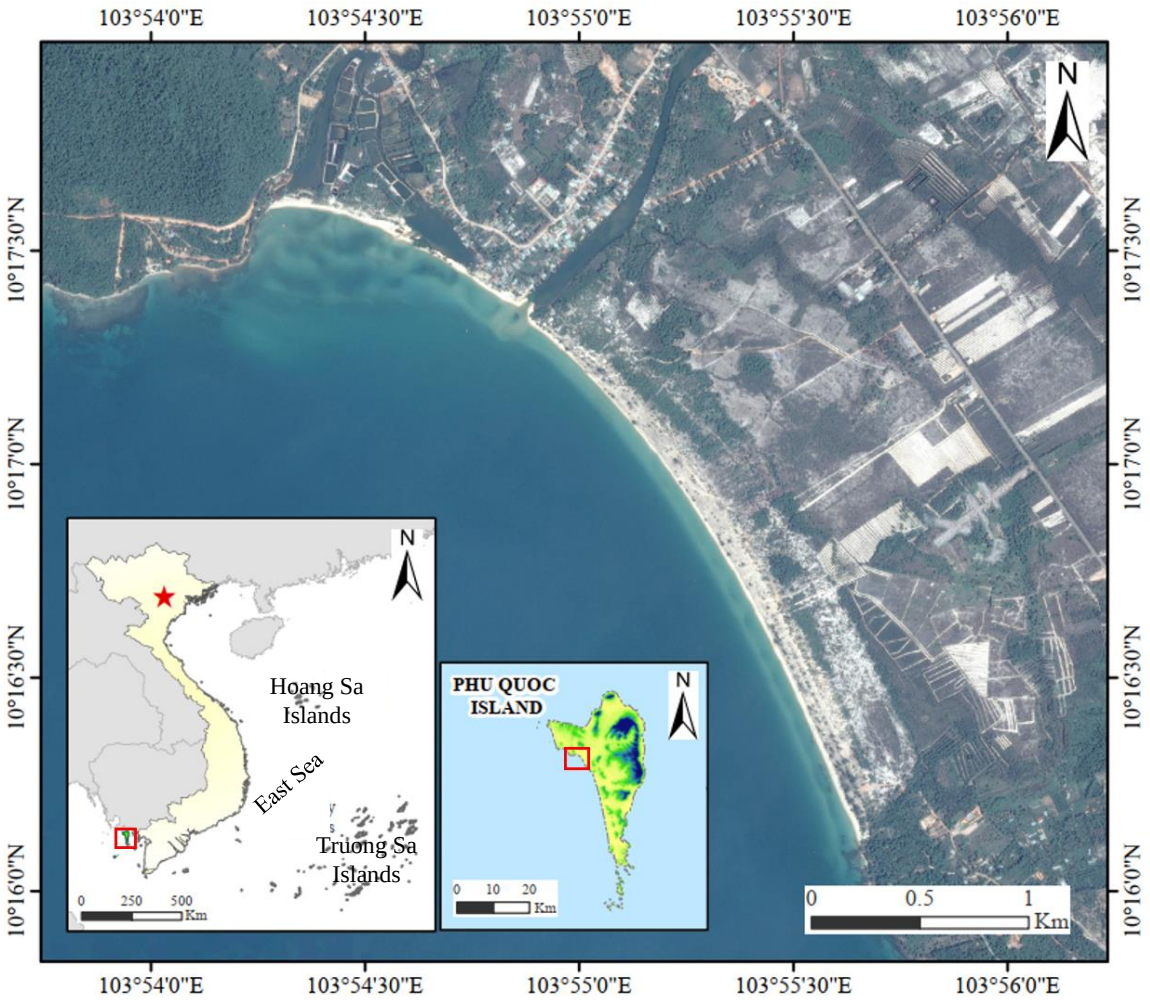

Figure 1. Study area.

2.2. Workflow of the study

The workflow of this study is illustrated in Figure 2. Initially, data collection was undertaken to acquire high-resolution Google Earth images, as well as beach slope and water level measurements. Upon gathering the necessary data, an image analysis, inclusive of tidal correction, was performed to determine the positions of the shoreline. Subsequently, changes in the shoreline and rates of these changes were statistically analyzed, utilizing the tidally corrected shoreline data. Finally, the Longshore Sediment Transport Rates (LSTR) were calculated using the one-line model, based on the determined shoreline change rates.

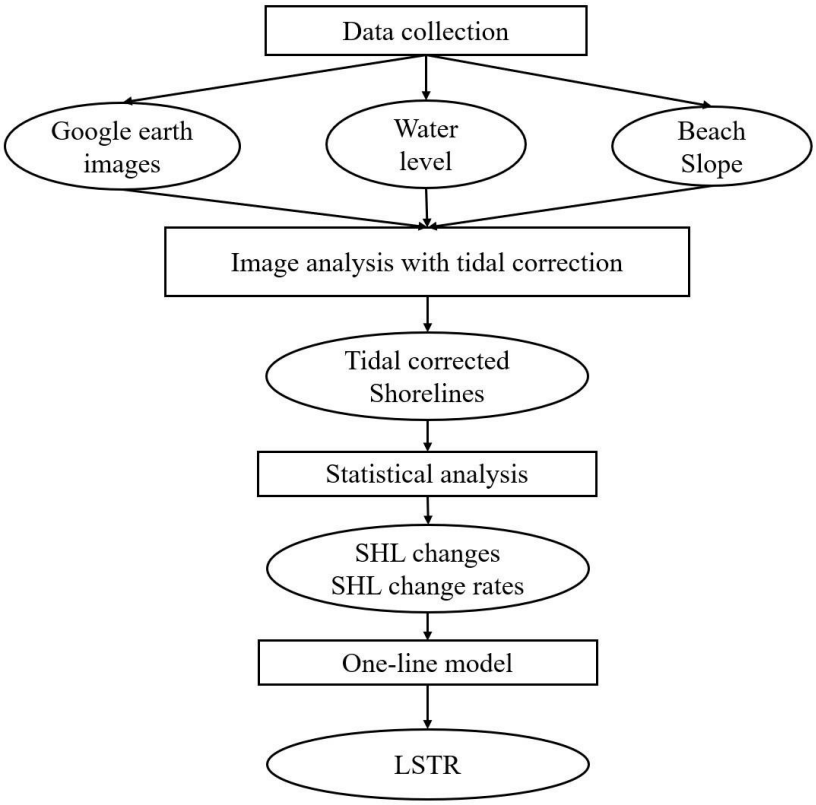

Figure 2. Study flow diagram.

2.3. Satellite image analysis

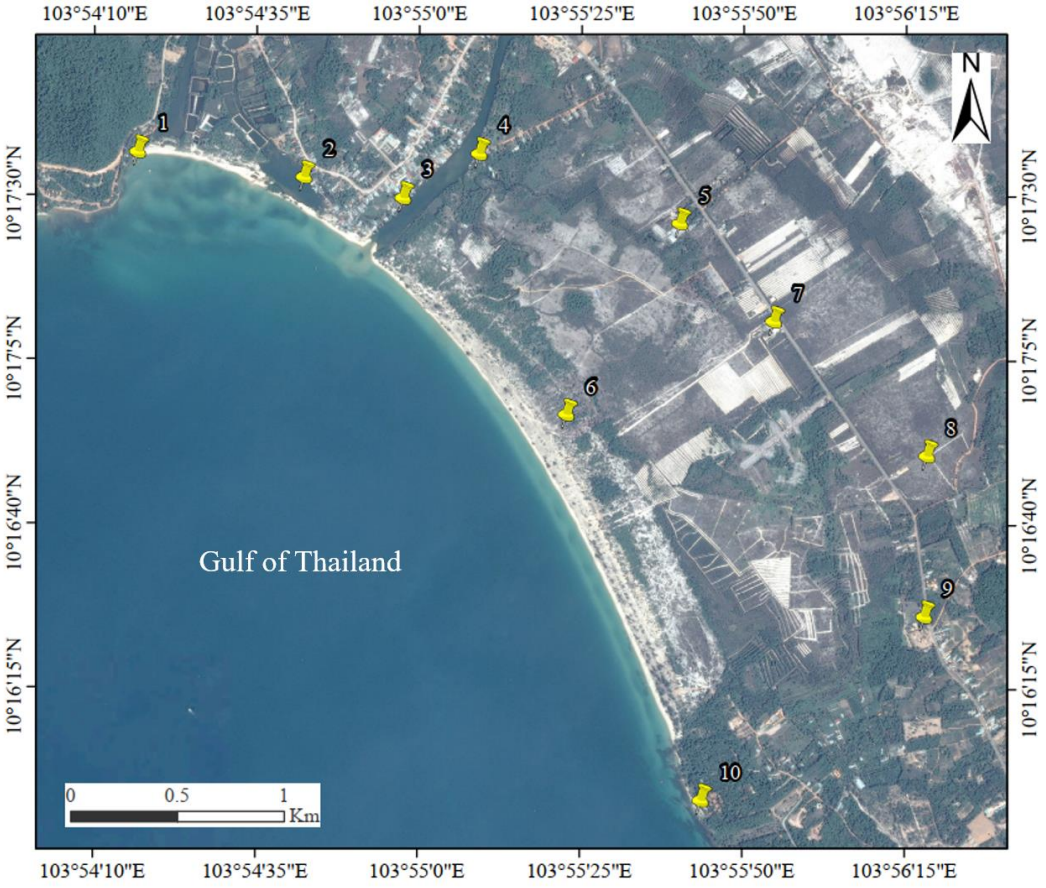

Figure 3. GCPs to geo-correct the Google earth images.

Google Earth images from 2016 to 2020 were used for the analysis. The details of the images are presented in Table 1. Since the free images downloaded from Google Earth are not geometrically corrected, they were geo-corrected using a set of 10 ground control points (GCPs), as shown in Figure 3. After geo-correction, the shoreline positions were extracted using the image segmentation approach [19]. Tidal correction was also applied to the shoreline positions using the method presented by [20], utilizing hourly water levels collected at the Phu Quoc Oceanography Station from 2016 to 2020. The water level data are presented in Figure 4.

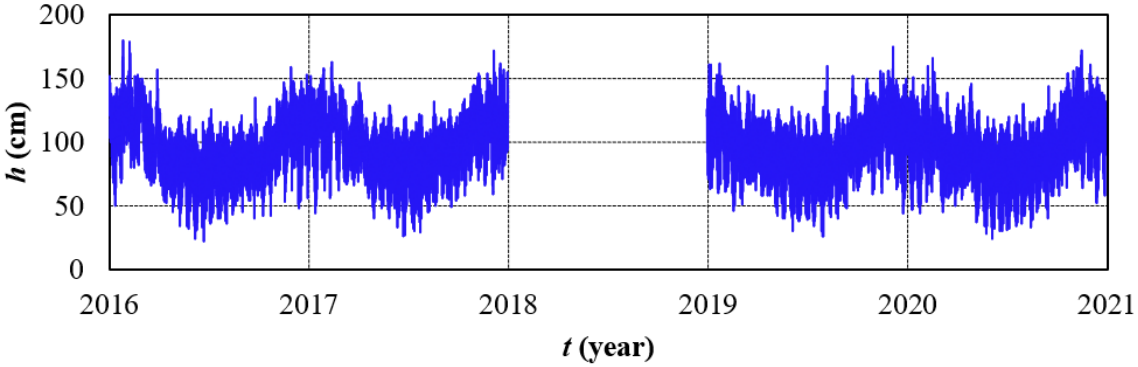

Figure 4. Water levels at Phu Quoc Oceanography station in 2016, 2017, 2019 and 2020.

Table 1. Information of Google earth images.

Captured date	Sources	Resolution (m)	Coordinate system
03 Jan 2016	CNES/Airbus	1.0 m	UTM
10 Dec 2017	Maxar Technologies	1.0 m	UTM
06 Jan 2019	CNES/Airbus	1.0 m	UTM
14 Dec 2019	Maxar Technologies	1.0 m	UTM
19 Feb 2020	Maxar Technologies	1.0 m	UTM

For the purpose of convenience, a local coordinate system was used in this study to facilite the calculation of shoreline change rates as well as integrated the LSTR a long the Cua Can Beach. This local coordinate system is defined by rotating the images in the UTM system at an angle of 132o clockwise as shown in Figure 5.

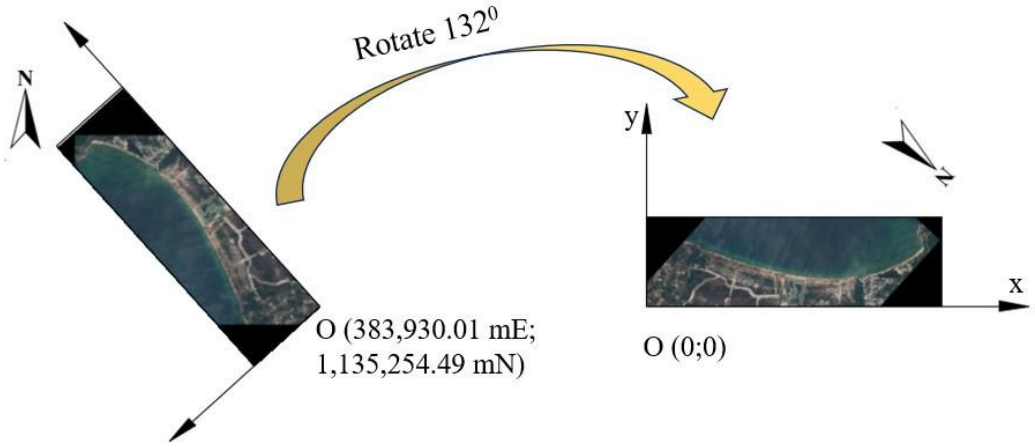

Figure 5. Defining the local coordinate system.

2.4. Shoreline changes and shoreline change rate

The shoreline positions extracted from the images were utilized to calculate the changes in the shoreline relative to the baseline established in 2016. This calculation was performed using the following equation:

$$Dy = y(x_i,t_i) - y(x_i,2016) \quad (1)$$

where $0 \le x_i \le 3800$ m and $2016 \le t_i \le 2020$.

In addition, rates of shoreline change are calculated based on the temporal variations in shoreline positions at each cross-section of the beach. This analysis employs the least squares regression method to quantify changes over time, ensuring a robust statistical foundation for understanding trends. The specific formula used for this calculation is as follows [21]:

$$y = a \times t + b \quad (2)$$

where y represents the shoreline position measured at time t, a is the rate of shoreline change calculated using the least squares regression method, and b is the intercept of the regression line with the y-axis (ordinate).

2.5. Integrated longshore sediment transport rate

The one-line theory was utilized to estimate the LSTR based on long-term shoreline changes [10]. This model states that the beach profile shifts parallel to itself in the cross-shore direction, as illustrated in Figure 7. Developed on the principle of sand conservation within a defined control volume of the shoreline section, the model presupposes the existence of both an offshore limit and an upper limit. These limits define the boundaries beyond which no significant changes occur. Within these confines, the beach profile maintains a constant shape as it moves in the cross-shore direction (Figure 7), suggesting that sediment transport gradients are uniformly distributed across the active portion of the beach [17].

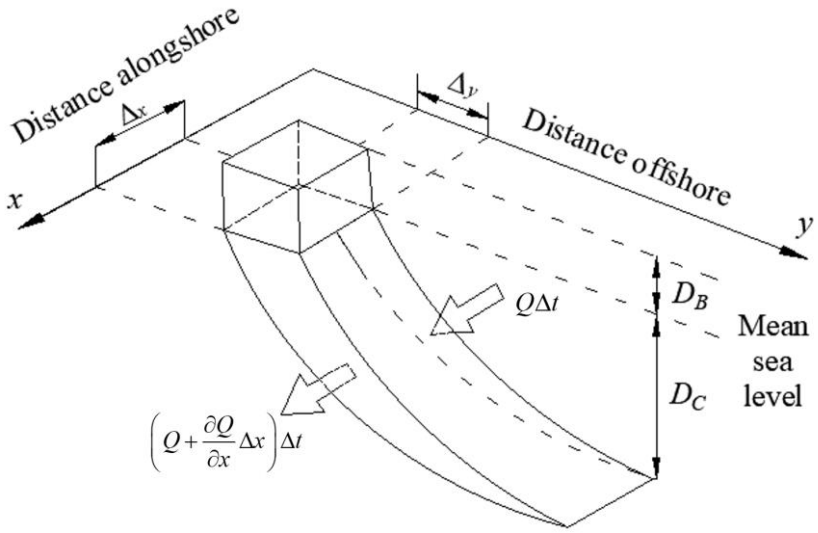

Figure 6. Sketch showing the idea of the one-line model.

The LSTR on the southern and northern coasts of Cua Can Beach were analyzed and integrated as shown in Figure 7, utilizing the theory of the One-line model. In Figure 7, the black solid lines represent the initial shoreline position, while the dashed blue lines depict the shoreline position after a period of time. This model is based on the principle of sediment conservation, which is outlined as follows [17]:

$$\frac{\partial y}{\partial t} + \frac{1}{D}\frac{\partial Q}{\partial x} = 0 \quad (3)$$

In this analysis, D represents the limit height of longshore sediment transport, which is the sum of berm height (D_B) and depth of closure (D_C), expressed as $D = D_B + D_C$. Here, t denotes time, while x and y are the longshore and cross-shore distances, respectively. Q signifies the LSTR. Due to the limited availability of measured data, the values for D_B and D_C were sourced from Song Tranh inlet, located approximately 15 km south of the study area

and sharing the same coastline characteristics. As reported by [22], D_B and D_C are determined to be 4.5 m and 1.5 m, respectively, leading to a total depth (D) of 6 m.

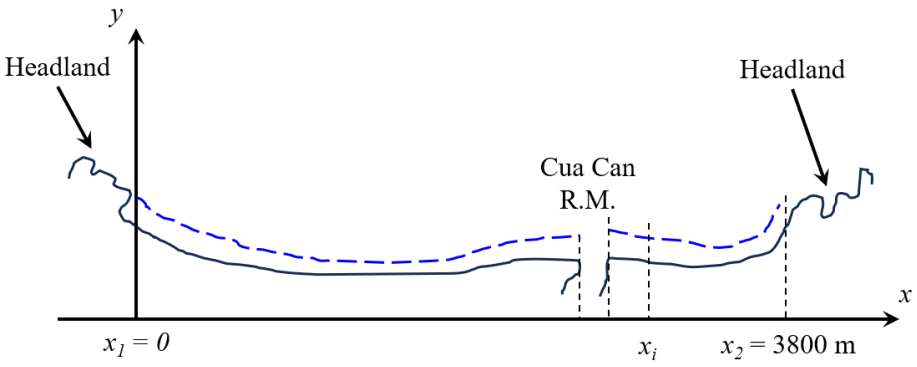

Figure 7. Integrated LSTR along the Cua Can Beach.

From Equation (3) and as illustrated in Figure 7, the integration of LSTRs on the southern and northern coasts of the Cua Can Beach area can be conducted as follows:

- For the southern coastline:

$$Q(x) = D\int_{x_1}^{x} \frac{\partial y}{\partial t} dx \quad (4)$$

- For the northern coastline:

$$Q(x) = -D\int_{x_2}^{x} \frac{\partial y}{\partial t} dx \quad (5)$$

To integrate the Longshore Sediment Transport Rates (LSTRs), it is necessary to define a boundary where the LSTR equals zero. Since Cua Can Beach is a pocket beach, the headlands at both ends are considered the boundaries where the transport rate, Q, is zero. These boundaries are denoted as $x_1 = 0$ and $x_2 = 3800$ m in Figure 7.

3. Results

3.1. Shoreline changes

Shoreline changes, with reference to the year 2016, are presented in Figure 8. As can be seen from the figure, the shoreline along the southern coast of the Cua Can River mouth remained stable from 2016 to 2020, as indicated by the fluctuations of the shoreline around the referenced line. There was a small amount of beach accumulation at the beach section from x = 1000 m to x = 1400 m. On the other hand, significant beach accretion can be observed on the northern coastline, with the maximum buildup of the shoreline approximately 35 m at the end of the beach (x = 3400 m to x = 3800 m). Another notable

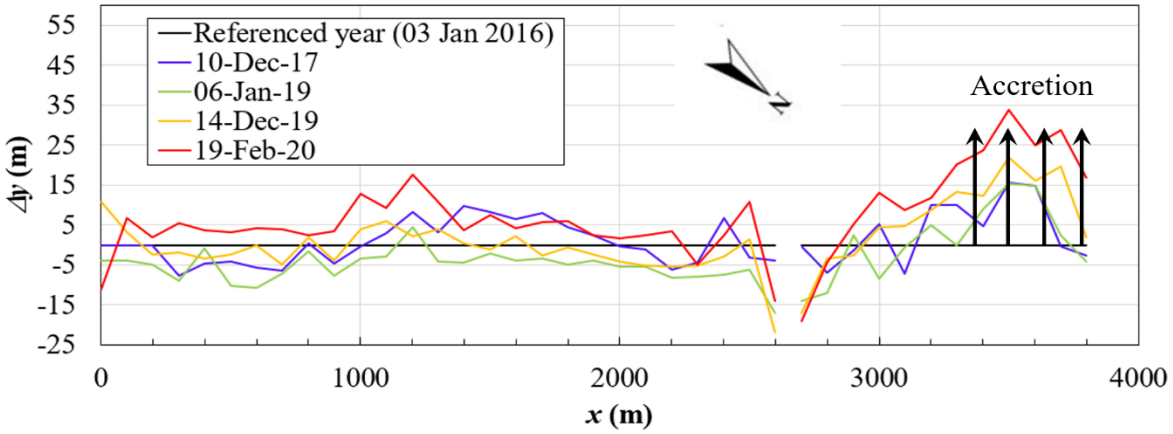

Figure 8. Shoreline changes.

point is the shoreline retreat at the Cua Can River mouth, with the maximum retreat reaching up to -25 m. From this diagram, it can be inferred that sand is being transported to the north of Cua Can Beach.

3.2. Shoreline change rates

The temporal variation of shoreline positions at selected cross-sections of Cua Can Beach is presented in Figure 9, where the blue circles represent the shoreline positions from 2016 to 2020, and the red line is the linear regression line of these positions. As shown in Figure 9, the equations of the regression lines follow the form of Equation (2). Consequently, the rate of shoreline change at each cross-section of Cua Can Beach can be easily determined from Figure 9. For instance, the rate of shoreline change at x = 2700 m is -0.0137 m/day, which equates to approximately -5 m/year. It should be noted that the results are based solely on a series of data from 2016 to 2020. Therefore, the findings of this study should be applied cautiously and must be supplemented with additional data in the future to enhance the reliability of the results. Additional calculated values for the results are presented in Table 2.

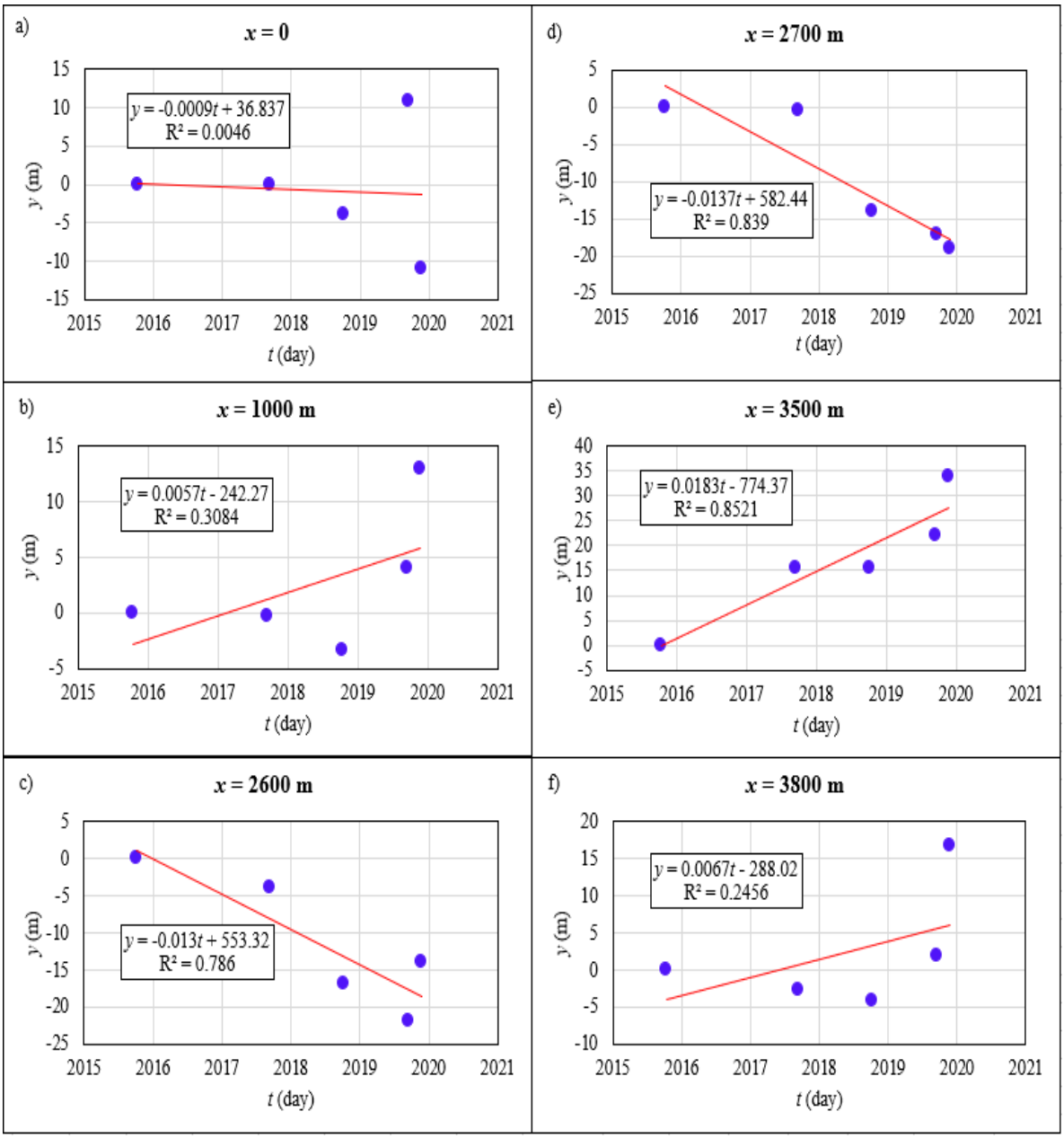

Figure 9. Temporal variations of shorelines at some cross-sections along the Cua Can Beach.

Table 2. Statistical table of additional calculated values for the results.

Cross-section	Distance alongshore x (m)	a (m/day)	a (m/year)	$D = D_B + D_C$ (m)	DA (m^2/year)	DV (m^3/year)	Q (m^3/year)
1	0	-0.0009	-0.32	6	0	0	0
2	100	0.0031	1.13	6	40.77	245	245
3	200	-0.0006	-0.21	6	45.95	276	520
4	300	0.0017	0.61	6	19.98	120	640
5	400	0.0010	0.36	6	48.75	292	933
6	500	0.0001	0.03	6	19.43	117	1,049
7	600	0.0014	0.50	6	26.45	159	1,208
8	700	0.0002	0.07	6	28.64	172	1,380
9	800	0.0013	0.47	6	27.11	163	1,542
10	900	0.0001	0.02	6	24.54	147	1,690
11	1000	0.0057	2.06	6	104.09	625	2,314
12	1100	0.0045	1.66	6	186.11	1117	3,431
13	1200	0.0061	2.23	6	194.65	1168	4,599
14	1300	0.0043	1.56	6	189.62	1138	5,736
15	1400	-0.0005	-0.18	6	69.17	415	6,151
16	1500	0.0008	0.30	6	6.46	39	6,190
17	1600	0.0008	0.30	6	30.09	181	6,371
18	1700	-0.0003	-0.13	6	8.56	51	6,422
19	1800	0.0008	0.28	6	7.51	45	6,467
20	1900	-0.0006	-0.23	6	2.12	13	6,480
21	2000	-0.0012	-0.44	6	-33.90	-203	6,277
22	2100	-0.0011	-0.41	6	-42.74	-256	6,020
23	2200	-0.0002	-0.09	6	-25.00	-150	5,870
24	2300	-0.0035	-1.28	6	-68.25	-410	5,461
25	2400	-0.0019	-0.68	6	-97.70	-586	4,874
26	2500	0.0043	1.58	6	45.19	271	5,146
27	2600	-0.0130	-4.76	6	-158.78	-953	4,193
28	2700	-0.0137	-4.99	6	-487.50	-2925	18,130
29	2800	-0.0027	-1.00	6	-299.67	-1798	19,928
30	2900	0.0015	0.54	6	-22.98	-138	20,066
31	3000	0.0045	1.65	6	109.79	659	19,407
32	3100	0.0058	2.13	6	189.03	1134	18,273
33	3200	0.0060	2.18	6	215.39	1292	16,981
34	3300	0.0100	3.66	6	291.89	1751	15,230
35	3400	0.0126	4.61	6	413.16	2479	12,751
36	3500	0.0183	6.67	6	563.87	3383	9,367
37	3600	0.0133	4.85	6	575.83	3455	5,912
38	3700	0.0170	6.21	6	552.70	3316	2,596
39	3800	0.0067	2.45	6	432.70	2596	0

The diagram in Figure 10 depicts the rate of shoreline change along Cua Can Beach, segmented at 100 m intervals. The rate of change is visually represented by a line graph, with the horizontal axis (x) marking the distance along the beach in meters, and the vertical axis (a) indicating the rate of shoreline change in meters per year (m/year). Upward spikes along the line graph correspond to areas of accretion, while downward spikes indicate erosion.

Noticeably, there is a significant retreat at the river mouth, indicated by a rate of -5 m/year, which signifies erosion. Conversely, along the northern stretch of the beach, there is a substantial advance, with the maximum accretion rate reaching up to 6 m/year. This positive change rate indicates areas of beach growth or accretion.

The majority of the southern shoreline exhibits stability, with no discernible rate of change, marked as 0 m/year on the diagram. This suggests that these areas have neither gained nor lost significant amounts of sand over the observed period. An exception is noted

in the section between 1000 m and 1400 m, where there is evidence of accretion with a change rate of up to 2 m/year.

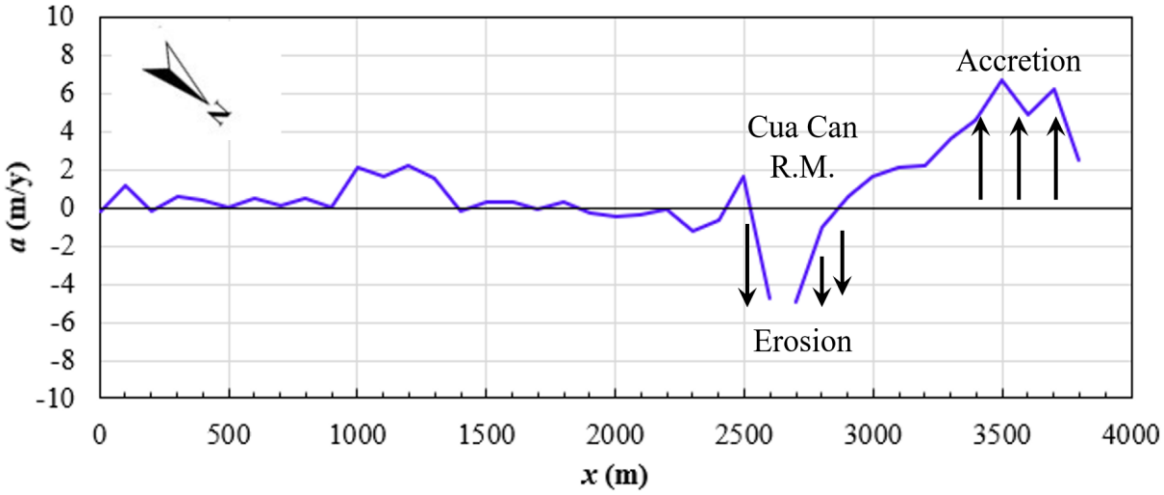

Figure 10. Shoreline change rate at intervel of 100 m along the Cua Can Beach.

3.3. LSTR along the Cua Can Beach

The Longshore Sediment Transport Rate (LSTR) along Cua Can Beach is depicted in Figure 11. The figure reveals that LSTR was substantial along the northern part of Cua Can Beach, with a rate of 20,000 m³/year. In contrast, the LSTR on the southern side of the Cua Can River mouth was much lower, at approximately 5,000 m³/year.

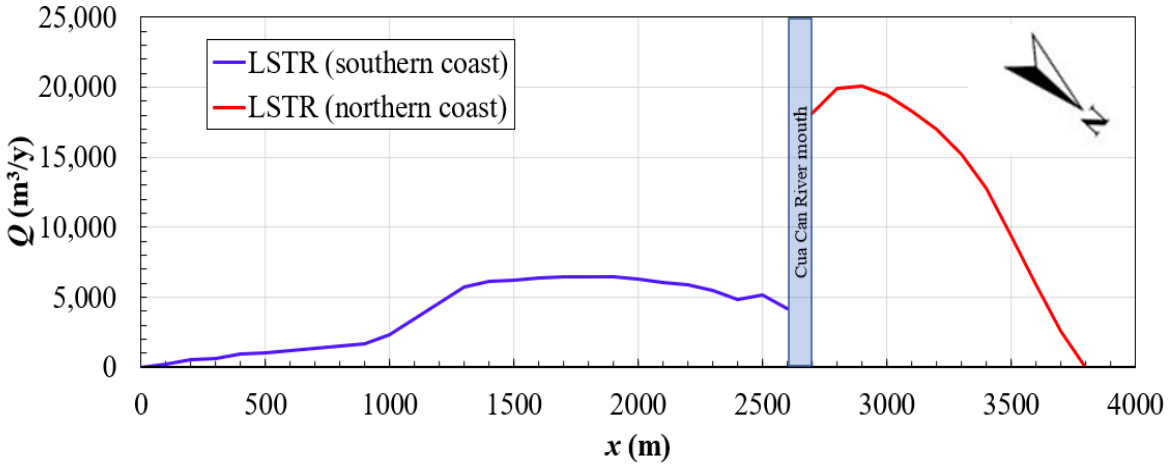

Figure 11. LSTRs along the Cua Can Beach.

4. Discussions

To evaluate the results of this study, the Longshore Sediment Transport Rate (LSTR) estimated herein was compared with LSTRs estimated for the Song Tranh Inlet [22], which is located approximately 15 km south of our study area, along the same coastline on the west coast of Phu Quoc City. This comparison is depicted in Figure 12. In the study at Song Tranh Inlet [22], the LSTR was calculated based on morphological changes of the sand spit at the inlet. The LSTR calculations were segmented into three periods, corresponding to the elongation and breaching of the sand spit. Additionally, a value of LSTR calculated using the CERC formula was also provided. As observed in the figure, the LSTR estimated at Cua Can Beach has the same order of magnitude as that in the Song Tranh Inlet study. This consistency underscores the validity of the methodology employed in our study.

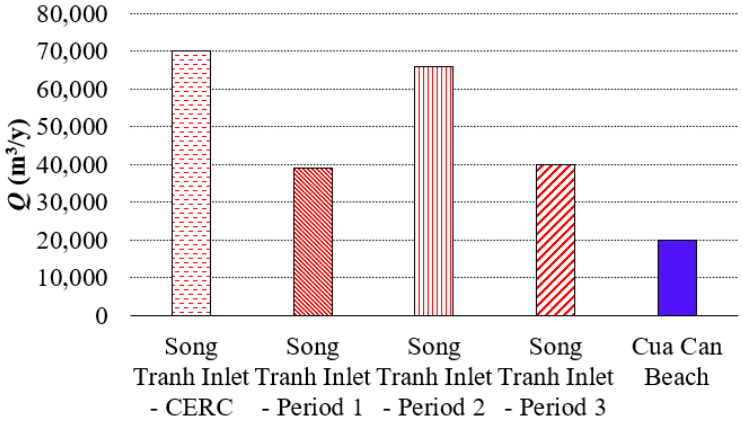

Figure 12. Comparison of LSTR with a study at Song Tranh inlet in the Phu Quoc city [22].

5. Conclusions

Remote sensing and the theory of the one-line model have been applied to rapidly assess the shoreline changes and Longshore Sediment Transport Rates (LSTRs) along Cua Can Beach in Phu Quoc City, Kien Giang Province, Vietnam, from 2016 to 2020. The main findings of this study can be summarized as follows:

- The southern part of Cua Can Beach remained stable during the survey period, while the shorelines at the Cua Can River mouth retreated at a rate of 5 m/year. In contrast, the beach on the northern part accumulated sediment at a rate of 6 m/year.
- The predominant direction of the LSTRs along Cua Can Beach was from south to north.
- The magnitude of LSTR along the southern beach was 5,000 m³/year, and along the northern beach, it was 20,000 m³/year. The maximum LSTR at Cua Can beach is comparable to the LSTRs estimated for the Song Tranh Inlet, located 15 km south of the study area.
- The main drawback of this study is that it is based solely on a series of data from 2016 to 2020. Therefore, the findings of this study should be applied cautiously and must be supplemented with additional data in the future to enhance the reliability of the results.

Author contribution statement: Developing research ideas: D.V.D.; Process data: processing, manuscript writing: D.V.D., T.V.T., P.T.D., T.K.M., N.A.H., Q.V.C.; GIS: P.T.D., P.T.T.D., N.A.H.; Reviewed and completed the manuscript: T.V.T., D.V.D.

Competing interest statement: The authors declare no conflict of interest.

References

1. Tuyet, D.T.; Thuy, N.T.T.; Nhan, D.V.; Hoang, N.T.T.; . The potential and direction for tourism development after Covid-19 in Vietnam. OSF Preprints aduc8, Center for Open Science. 2022.
2. Tin, H.T.; Vinh, B.T. Mechanism of beach erosion at the west of Phu Quoc Island, Southern Vietnam. *VN J. Earth Sci.* **2014**, *36(1)*, 69–74.
3. Sanil Kumar, V.; et al., Longshore sediment transport rate–measurement and estimation, central west coast of India. *Coastal Eng.* **2003**, *48(2)*, 95–109.
4. Van Rijn, L.C. Longshore sand transport, in Coastal Engineering 2002: Solving Coastal Conundrums. World Scientific, 2003, pp. 2439–2451.
5. Kraus, N.C. Application of portable traps for obtaining point measurements of sediment transport rates in the surf zone. *J. Coastal Res.* **1987**, *3(2)*, 139–152.
6. Rosati, J.D.; Kraus, N.C. Hydraulic test of streamer sediment trap. *J. Hydraul. Eng.* **1988**, *114(12)*, 1527–1532.
7. Majewski, W. Field Studies on Sand Movement in the Coastal Zone (A Monograph) Polish Academy of Sciences. Poland, 1989.

8. Miller, H.C. Field measurements of longshore sediment transport during storms. *Coastal Eng.* **1999**, *36(4)*, 301–321.
9. Noujas, V.; Kankara, R.; Rasheed, K. Estimation of longshore sediment transport rate for a typical pocket beach along west coast of India. *Mar. Geod.* **2018**, *41(2)*, 201–216.
10. Oh, J.E.; Chang, Y.S.; Jeong, W.M.; Kim, K.H.; Ryu, K.H. Estimation of longshore sediment transport using video monitoring shoreline data. *J. Mar. Sci. Eng.* **2020**, *8*, 572.
11. Liang, T.Y.; Chang, C.H.; Hsiao, S.C.; Huang, W.P.; Chang, T.Y.; Guo, W.D.; Liu, C.H.; Ho, J.Y.; Chen, W.B. On-site investigations of coastal erosion and accretion for the northeast of Taiwan. *J. Mar. Sci. Eng.* **2022**, *10(2)*, 282.
12. Larson, M.; Kraus, N.C.; Hanson, H. Simulation of regional longshore sediment transport and coastal evolution–the "Cascade" model. *Coastal Eng.* **2002**, pp. 2612–2624.
13. Ellis, J.; Stone, G.W. Numerical simulation of net longshore sediment transport and granulometry of surficial sediments along Chandeleur Island, Louisiana, USA. *Mar. Geod.* **2006**, *232(3)*, 115–129.
14. Nguyen, X.T.; Tran, M.T.; Tanaka, H.; Nguyen, T.V.; Mitobe, Y.; Duong, C.D. Numerical investigation of the effect of seasonal variations of depth-of-closure on shoreline evolution. *Int. J. Sediment Res.* **2021**, *36(1)*, 1–16.
15. Xing, H.; Li, P.; Zhang, L.; Xue, H.; Shi, H.; You, Z. Numerical simulation of the beach response mechanism under Typhoon Lekima: A case study of the Southern Beach of Chudao. *J. Mar. Sci. Eng.* **2023**, *11(6)*, 1156.
16. Parthasarathy, K.; Deka, P.C. Remote sensing and GIS application in assessment of coastal vulnerability and shoreline changes: A review. *ISH J. Hydraul. Eng.* **2021**, *27(sup1)*, 588–600.
17. Pelnard-Considère, R. Essai de theorie de l'evolution des formes de rivage en plages de sable et de galets. *J. de L'hydraulique* **1957**, *4(1)*, 289–298.
18. Nguyen, Q.H.; Xuan, H.L. Trend analysis of rainfall in the Phu Quoc Island. *VNU J. Sci.: Earth Environ. Sci.* **2021**, *37(4)*, 22–32.
19. Pitas, I. Digital image processing algorithms and applications. John Wiley & Sons, 2000.
20. Hoang, V.C.; Tanaka, H.; Mitobe, Y. A method for correcting tidal effect on shoreline position extracted from an image with unknown capture time. *Geosciences* **2017**, *7(3)*, 62.
21. Dolan, R.; Fenster, M.S.; Holme, S.J. Temporal analysis of shoreline recession and accretion. *J. Coastal Res.* **1991**, *7(3)*, 723–744.
22. Duy, D.V.; Ty, T.V.; Thanh, T.N.; Minh, H.V.T.; De, C.V.; Duong, V.H.T.; Dan, T.C.; Viet, N.T.; Tanaka, H. Sand spit morphology at an inlet on Phu Quoc Island, Vietnam. *Water* **2023**, *15(10)*, 1941.

JOURNAL OF
HYDRO-METEOROLOGY

Research Article

Application GIS and remote sensing methods to assess the change in land surface temperature in Ba Ria - Vung Tau province, Vietnam

Nguyen Hai Au[1,2*]

[1] Institute for Environment and Resources; haiauvtn@gmail.com
[2] Vietnam National University Ho Chi Minh City; haiauvtn@gmail.com

*Corresponding author: haiauvtn@gmail.com; Tel.: +84–989115280

Received: 14 March 2024; Accepted: 17 April 2024; Published: 25 June 2024

Abstract: Ba Ria-Vung Tau province is situated in the Southern main economic area with rapid urbanization, industry, and modernization. The expansion of impermeable land cover has grown significantly in response to climate change and global warming, which have resulted in higher surface temperatures in the province in recent years. This study provides an assessment of the impact of increased temperature in Ba Ria - Vung Tau province based on surface temperature values extracted from thermal infrared Landsat image data during the period 2010-2021. The variety of land cover tends to influence the properties of land surface temperature reported by satellite sensing sensors. The results show that the heat island activity is strong, with a decreasing trend from urban to peri-urban areas. The surface temperatures above 30-40^{o}C accounted for just 5% of the study area in 2010, but the rate doubled by 2021. Typical areas with an increase in surface temperature due to the rapid urbanization include Vung Tau city, Ba Ria city, Long Dien district, and Phu My town. This demonstrates that the changes in land cover is a factor contributing to the increase in land surface temperature in the area.

Keywords: Remote sensing; Surface temperature; Land cover change.

1. Introduction

In parallel with population growth, urbanization and industrialization have accelerated rapidly. This has resulted in fast changes in land use which affected the vegetation cover on the Earth surface tremendously. Particularly, this affects the distribution of solar radiation, leading to an increase in atmospheric temperature, especially in urbanizing areas with hotter temperatures than rural areas [1, 2]. Many studies on the effects of land cover change on atmospheric dynamics and climate change have been conducted across the world. The expansion of building causes the shrinkage of green areas, which causes a rise in the Earth's surface temperature [3–6], which may be detected by measuring the emissivity of vegetation and soil.

With the advanced technologies of remote sensing, satellite images are now the best option for analyzing surface cover changes and swiftly collecting data. In particular, Landsat images have been widely utilized in numerous studies to monitor local and global temperature changes. Land cover is one of the primary elements influencing surface temperature as shown in remote sensing images. According to previous studies, the surface temperatures of different land uses have significant differences [6]. Temperatures increase in areas influenced by anthropogenic activities and construction facilities, while being low in areas with vegetation [1]. Remote sensing offers high-resolution data with consistent Earth surface coverage, making it easy to

extract information from satellite data [7]. The combined use of remote sensing with GIS is effective in visualizing extracted information and monitoring land use changes. Climate change and surface changes have led to extensive assessments of land surface temperature changes in various global regions. Studies in Indonesia [3], Nigeria [5], Iran [8], India [9], Egypt [7] evaluated surface temperatures using heat bands in Landsat data using remote sensing and GIS. According to research findings, there is a considerable reduction in the amount of vegetation due to urban expansion, which raises surface temperatures.

In recent years, many Vietnamese researchers have paid their attention and interest in analyzing surface temperature fluctuations in the context of global climate change [10–13]. The study [10] claimed that pressure from the processes of industrialization, modernization, and urbanization in Ho Chi Minh (HCM) city is the main factor of higher surface temperatures and a robust urban heat island phenomenon. Similarly, studies in HCM [13], Binh Duong [11], and Hai Phong [12] analyzed land surface temperature changes based on impermeable surfaces in land cover and thermal infrared images using Landsat imagery.

Ba Ria - Vung Tau (BR-VT) province is located in the Southeast and serves as the entrance to the East Sea of provinces in the region with significant expansion of urbanization, industrialization, and modernization. The average amount of sunlight hours ranges from 170 hours/month in September to 299 hours/month in April. The change in average temperature in months (2015-2021) is around 0.6-2ºC compared to the average annual temperature.

This study aims to determine land use changes through classification and land surface temperature fluctuations in Ba Ria - Vung Tau province using Landsat data through the integration of remote sensing and GIS. In the context of climate change and global warming, this research can also be helpful in regulating and assisting decision-makers with a visual picture of high-temperature areas and urban construction development.

2. Methods and data

2.1. Study area

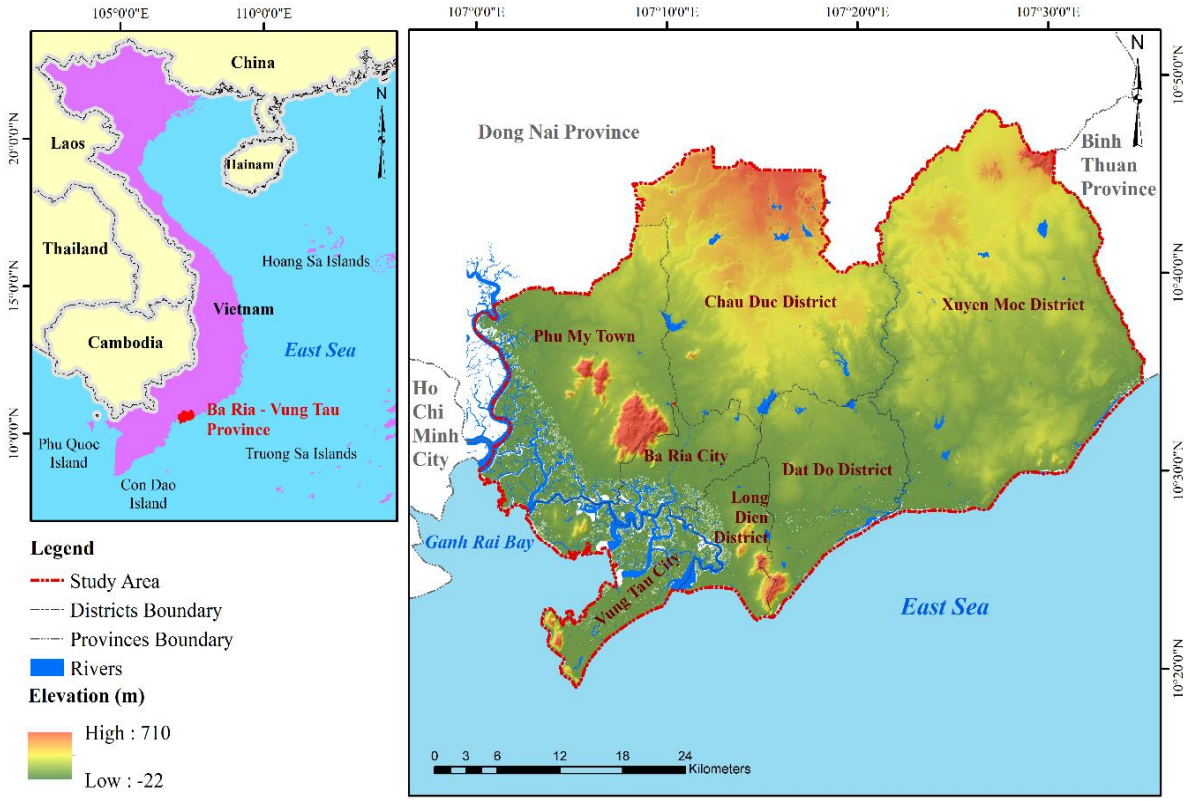

Figure 1. Location of the study area.

BR-VT province is located in the Southern key economic region, at the entrance to the East Sea of the provinces in the Southeast region, with rapid development, with rapid development of urbanization, industry, and modernization including changes in land use and temperature. This study was conducted throughout the province, including Vung Tau and Ba Ria cities, Phu My town, Long Dien district, Dat Do district, and Xuyen Moc district have an area of approximately 1473 km^2 (Figure 1). located in the tropical monsoon zone, with two distinct seasons and high temperatures. The area of urban and concrete land has increased rapidly, leading to rising surface temperatures, and marking urban heat island activity in recent years. This has been contributing a part to the global warming leading to climate change. BR-VT province has abundant radiation sources from sunlight. The study area's average temperature is 28.01°C.

2.2. Data

In the study, the data used is Landsat 7 images (for the period before February 2013) and Landsat 8 images of BR-VT province including 7 districts, cities and town collected from the United States Geological Survey at the earthexplorer.usgs.gov website [14]. The Landsat image data collected has been modified to correct terrain elevation deformation. It was collected twice (16 March 2010; 24 March 2016 and 06 March 2021) during the dry season (December to April of the following year), images have high quality and negligible cloud influence (cloud ratio < 1%), coordinates UTM-WGS-84 zone 48 North (Table 1).

Table 1. Detailed information on Landsat satellite.

No.	Satellite	Acquisition time	Spatial resolution (m)
1	Landsat 7	16/03/2010	30
2	Landsat 8	24/03/2016	30
3	Landsat 8	06/03/2021	30

Landsat 7 is equipped with an enhanced thematic mapper plus (ETM+) map sensor with 185 kilometers scanning range. The TM sensor contains 7 bands for recording electromagnetic spectrum reflections or radiation emitted from the earth's surface and 1 panchromatic band (Table 2) [15].

Landsat 8 improves on previous generations in terms of performance and dependability by carrying two sensors: Operational land imager (OLI) and thermal infrared sensor (TIRS). The scanning band width is 190 kilometers. Landsat 8 picture includes 11 spectral bands (9 shortwave bands and 2 longwave thermal bands) (Table 2) [16]. These three images provide seasonal detail of the Earth's surface with a spatial resolution of 30 m.

Table 2. Landsat satellite specifications [16].

Landsat 7 ETM+ Bands				**Landsat 8 OLI and TIRS Bands**			
Bands		Wavelength (μm)	Resolution (m)	Bands		Wavelength (μm)	Resolution (m)
				Band 1	Coastal/ Aerosol	0.435-0.451	30
Band 1	Blue	0.441-0.514	30	Band 2	Blue	0.452-0.512	30
Band 2	Green	0.519-0.601	30	Band 3	Green	0.533-0.590	30
Band 3	Red	0.631-0.692	30	Band 4	Red	0.636-0.673	30
Band 4	NIR	0.772-0.898	30	Band 5	NIR	0.851-0.879	30
Band 5	SWIR-1	1.547-1.749	30	Band 6	SWIR-1	1.566-1.651	30
Band 6	TIR	10.31-12.36	60	Band 7	SWIR-2	2.107-2.294	30
Band 7	SWIR-2	2.064-2.345	30	Band 8	Pan	0.503-0.676	15
Band 8	Pan	0.515-0.896	15	Band 9	Cirrus	1.363-1.384	30
				Band 10	TIR-1	10.60-11.19	100
				Band 11	TIR-2	11.50-12.51	100
NIR - Near Infrared SWIR - Shortwave Infrared				Pan - Panchromatic TIR - Thermal Infrared			

2.3. Methods

2.3.1. Remote sensing images interpretation

Atmospheric correction will aid in the elimination of confounding variables that alter the image band's reflectance value taken by satellite sensors, boosting the dependability of the analysis results. The procedure for performing land surface temperature calculations and the methods used are shown in Figure 2.

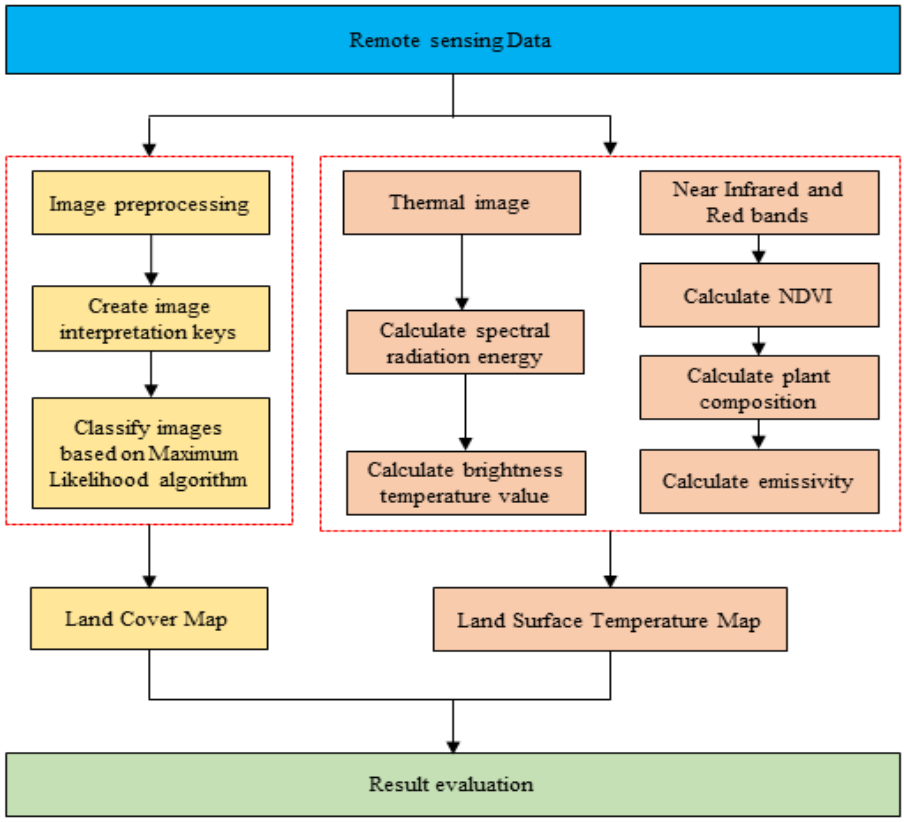

Figure 2. Methodology for land surface temperature assessment.

2.3.2. Land surface temperature from Landsat 8 image data

This study uses the emissivity from normalized difference vegetation index approach to calculate land surface temperature using Landsat 8 image data.

Converting numerical values to spectral radiant energy values: Landsat satellite image data will be modified for radiation after being captured, transforming numerical values to spectral reflected energy values. Because there is no link between the spectral radiation value and Landsat 8 image data, so it should be calculated directly according to the following formula [16, 17]:

$$L_\lambda = M_L \times Q_{cal} + A_L \quad (1)$$

where L_λ is the spectral radiance; M_L is the band-specific multiplicative rescaling factor from the Landsat 8 image metadata file (M_L = 0.0003342); Q_{cal} is the quantized and calibrated standard product pixel values; AL is the band-specific additive rescaling factor from the Landsat 8 image metadata file (AL = 0.1).

Conversion to Top of Atmosphere Brightness Temperature: Using the thermal constants in the metadata file, thermal band data can be converted from spectral radiance to top of atmospheric brightness temperature [10].

$$T_b = \frac{K_2}{\ln\left(\frac{K_1}{L_\lambda} + 1\right)} - 273{,}15 \quad (2)$$

where T_b is the top of atmosphere brightness temperature; L_λ is TOA spectral radiance; K_1, K_2 are the band-specific thermal conversion constant from the Landsat 8 image metadata file (K_1 = 774.88; K_2 = 1321.07).

Normalized difference vegetation index (NDVI): NDVI is a typical technique that uses reflectance measurements at red and near-infrared wavelengths to determine the quality of terrestrial green vegetation. Use the following formula to determine the NDVI value [18]:

$$NDVI = \frac{NIR - RED}{NIR + RED} \quad (3)$$

where NDVI is the normalized Difference Vegetation Index; NIR is the near-infrared band of Landsat 8 remote sensing image; RED is the red band of Landsat 8 remote sensing image.

Proportion of Vegetation: The proportion of vegetation is calculated according to the formula [18]:

$$P_v = \left(\frac{NDVI - NDVI_{min}}{NDVI_{max} - NDVI_{min}} \right)^2 \quad (4)$$

where P_v is the proportion of vegetation; $NDVI_{min}$ and $NDVI_{max}$ are values range from -1 to 1.

Surface emissivity: The emissivity of natural surfaces varies due to different land cover characteristics, such as the distinction between fields, urban areas, and vacant land [10, 19]. Surface emissivity (ε) is calculated based on the following formula [10, 18, 19]:

$$\varepsilon = mP_v + n \quad (5)$$

where $m = \varepsilon_v - \varepsilon_s - (1 - \varepsilon_s)F\varepsilon_v$; $n = \varepsilon_s(1 + \varepsilon_s)F\varepsilon_v$

where ε_v and ε_s are the surface emissivities of the vegetated surfaces and vacant land, respectively. The reference values for ε_v and ε_s are 0.99 and 0.97, respectively [19]. And F is the shape index, assuming a different geometric distribution and F = 0.55 [19, 20]. Therefore, the formula is represented precisely as follows:

$$\varepsilon = 0.004 \times P_v + 0.986 \quad (6)$$

where ε is the surface emissivity; P_v is the proportion of vegetation values.

Land surface temperature (LST): is the radiation temperature calculated from the brightness temperature, wavelength of emitted radiation, and land surface emissivity using the following formula [3, 16, 19]:

$$T_S = \frac{T_b}{1 + \left(\lambda \frac{T_b}{\rho} \right) Ln(\varepsilon)} \quad (7)$$

where T_S is the land surface temperature; T_b is the top of atmosphere brightness temperature; λ is the wavelength of emitted radiation; ε is the surface emissivity.

The wavelength of the radiated heat band $\rho = \frac{hc}{\sigma} = 1,4388 \times 10^{-2} mK = 14388 \mu mK$

2.3.3. Land surface temperature from Landsat 7 image data

Perform calculations to convert pixel values from numerical values to spectral radiant values according to the formula [15]:

$$L_\lambda = \left(\frac{L_{max} - L_{min}}{Q_{cal\,max} - Q_{cal\,min}} \right) \times (Q_{cal} - Q_{cal\,min}) + L_{min} \quad (8)$$

where L_λ is the spectral radiance; Q_{cal} is the quantized and calibrated standard product pixel values; L_{max}, L_{min} are the spectral radiation value is calculated corresponding to each low gain and high gain state (Table 3).

Table 3. L_{max}, L_{min} values for LANDSAT 7 thermal images.

Band	Satellite	Lmax	Lmin
6.1	LANDSAT 7 /ETM+ High gain	17.04	0
6.2	LANDSAT 7 /ETM+ Low gain	12.65	3.2

Convert the value of spectral radiance to temperature: The image is converted from spectral radiance values to physical variables. The satellite's effective temperature (black-body temperature) and conversion using the Planck physics formula [21]:

$$T_S = \frac{K_2}{Ln\left(\frac{K_1}{L_\lambda} + 1\right)} \quad (9)$$

where T_s is the land surface temperature; L_λ is the spectral radiance; K_1, K_2 are the correction factor is provided in the Landsat 7 image metadata file (Table 4).

Table 4. K_1, K_2 values for LANDSAT 7 thermal images.

Band	Satellite	K1	K2
6.1	LANDSAT 7 /ETM+ High gain	666.09	1282.71
6.1	LANDSAT 7 /ETM+ Low gain	666.09	1282.71

2.3.4. Evaluate accuracy after classification

The Kappa index (K) is often used to evaluate the dependability of remote sensing image classification maps [9], which is calculated according to the following formula:

$$K = \frac{(T - E)}{(1 - E)} \quad (10)$$

where T is an overall accuracy by digital matrix; E is the quantity representing the expectation of predictable classification accuracy.

The following table 5 illustrates the correlation between the accuracy of the classification map and the range of the Kappa coefficient.

Table 5. Ranges for the Kappa Coefficient [9].

Kappa Coefficient	Classification
< 0.4	Poor
0.41 - 0.60	Moderate
0.61 - 0.75	Good
0.76 - 0.80	Excellent
> 0.81	Almost perfect

3. Results and discursion

3.1. Component parameter

To determine the surface temperature in Ba Ria - Vung Tau province in 2010-2021, the collected remote sensing data is processed and calculated, respectively: Spectral Radiation values; Surface emissivity; Brightness temperature; NDVI index; Value of proportion of vegetation. These values are calculated from Landsat 7 and Landsat 8 images, using the Raster Calculator tool of ArcMap 10.4.1 software (shown in Figure A1, A2, A3 in the Appendix section).

3.2. Land cover classification

The land cover classification map illustrates that BR-VT province has many types of cover, including construction areas, residential areas, traffic areas (impervious surfaces); vacant land; fields, forests, plantations (vegetation), and networks of reservoirs and rivers (Figure 3). From 2010 to 2021, the impervious surface cover in Phu My town, Ba Ria and

Vung Tau cities and Long Dien district increased significantly, rising from 596.22 km^2 to 680.58 km^2. Meanwhile, the area of vacant land and vegetation tends to decrease (Table 6).

The classification results in 2010, 2016 and 2021 both have Kappa coefficients above 0.8 and overall accuracy above 90% (Table 7) according to the range of the Kappa coefficient in Table 5.

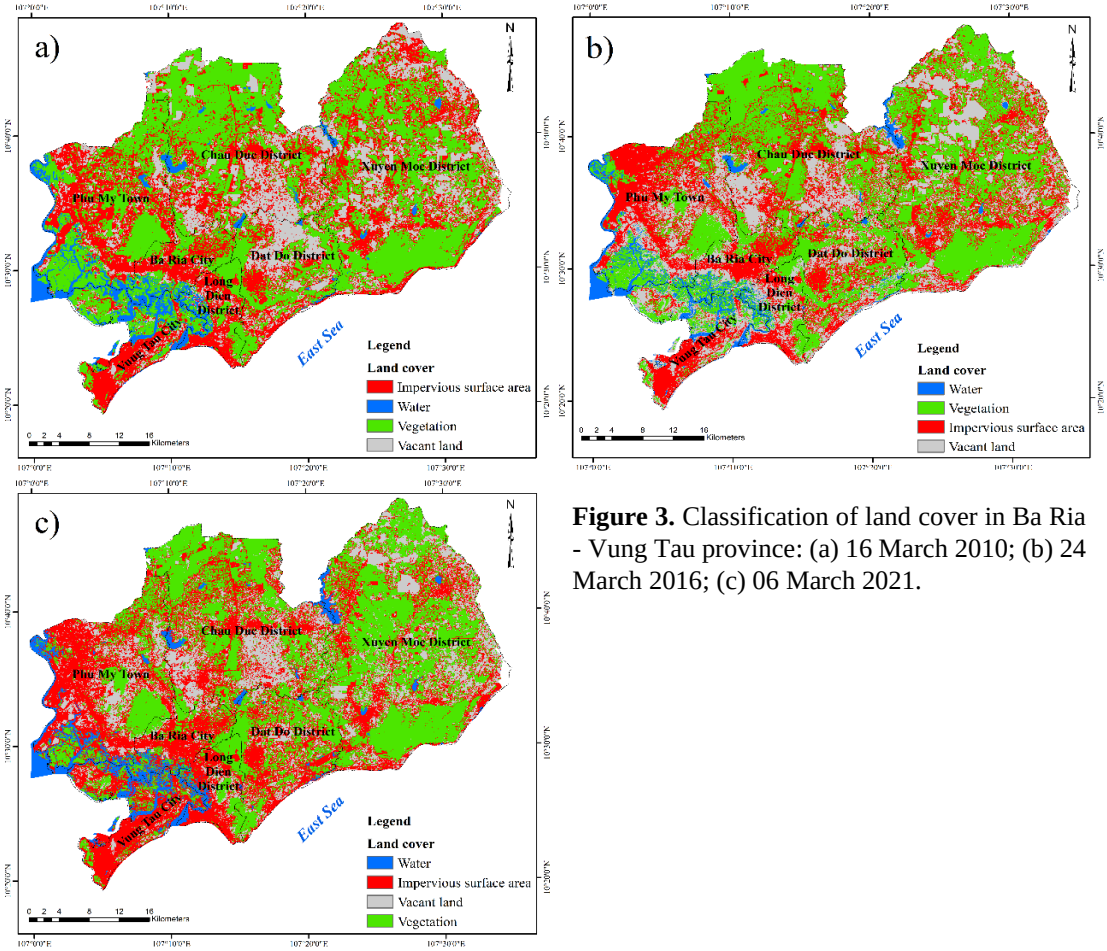

Figure 3. Classification of land cover in Ba Ria - Vung Tau province: (a) 16 March 2010; (b) 24 March 2016; (c) 06 March 2021.

Table 6. Area of land cover in Ba Ria - Vung Tau province.

Types of land cover	16 March 2010		24 March 2016		06 March 2021	
	Area (km^2)	%	Area (km^2)	%	Area (km^2)	%
Impervious surface area	596.22	17.547%	57.23	16.843%	680.58	20.071%
Vacant land	373.99	11.006%	46.85	13.788%	368.60	10.870 %
Vegetation	841.86	24.776%	79.22	23.315%	763.12	22.505 %
Water	94.27	2.774%	7.78	2.289%	94.65	2.791 %

Table 7. Classification accuracy.

Accuracy	2010	2016	2021
Overall Accuracy	97.55%	98.38%	98.57%
Kappa Coefficient	0.9658	0.9773	0.9805

3.2. Land surface temperature

The results of NDVI on 16 March 2010 (Figure 4a); 24 March 2016 (Figure 4b) and 06 March 2021 (Figure 4c) demonstrate that areas with low NDVI values are located mostly in hydro-system objects, including the Thi Vai River, Dinh River, Ray River, system of rivers, small streams, and lakes in BR-VT province. Low to medium NDVI values are seen in residential areas, construction works, and vacant land. Areas with forests and trees are places with medium to high NDVI values.

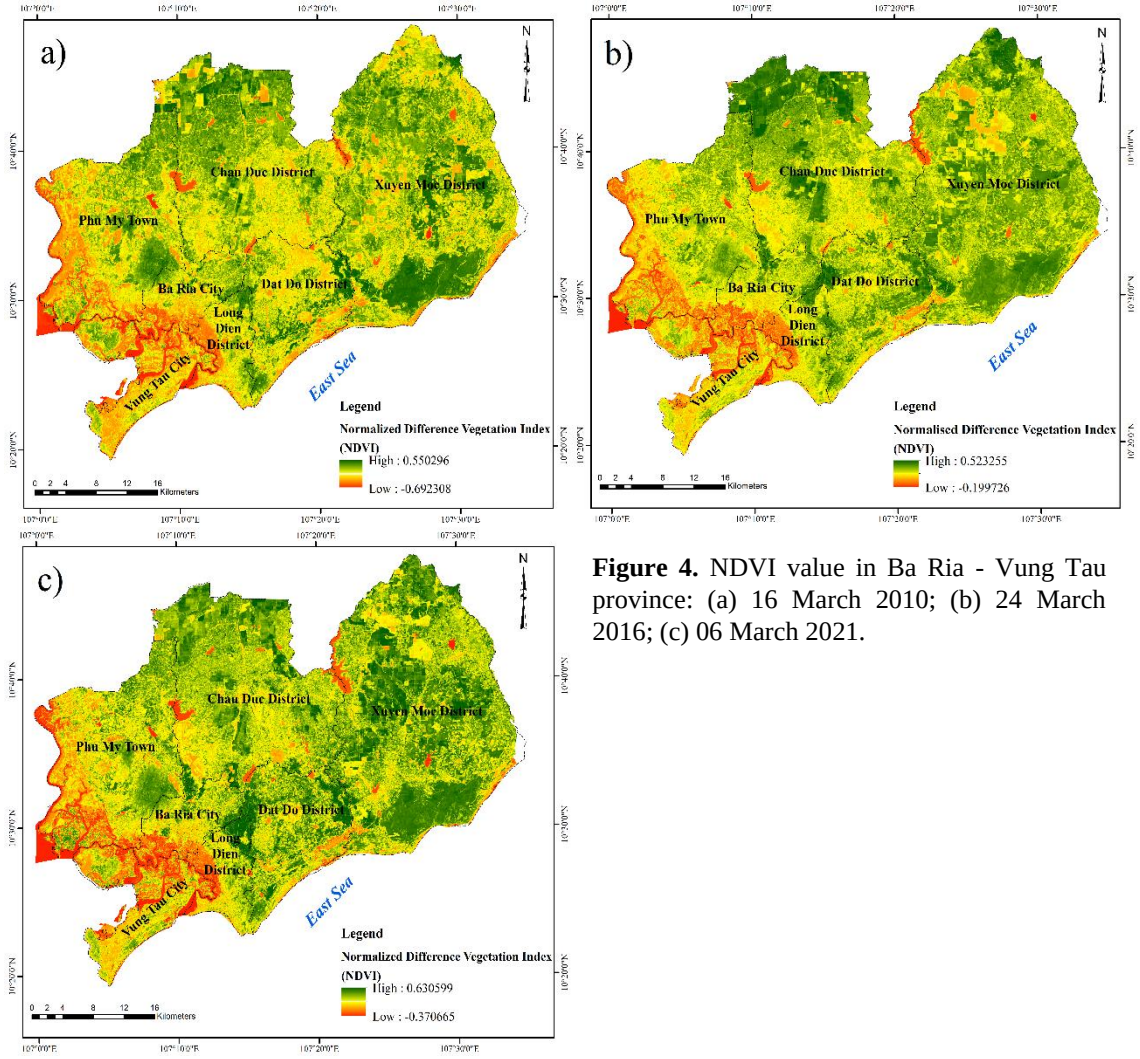

Figure 4. NDVI value in Ba Ria - Vung Tau province: (a) 16 March 2010; (b) 24 March 2016; (c) 06 March 2021.

From the results of analyzing remote sensing images, the area and surface temperature distribution in Ba Ria - Vung Tau province have been determined during the dry season on 16 March 2010; 24 March 2016 and 06 March 2021.

Table 8. Area of temperature levels in Ba Ria - Vung Tau province.

Temperature levels	16 March 2010		24 March 2016		06 March 2021	
	Area (km^2)	%	Area (km^2)	%	Area (km^2)	%
< 24	213.24	11.18	21.95	1.15	0.04	0.0021
24 - 27	769.89	40.38	240.49	12.61	224.13	11.75
27 - 30	726.33	38.09	589.68	30.93	472.94	24.80
30 - 33	190.13	9.97	693.24	36.36	819.45	42.98
33- 37	7.08	0.37	340.41	17.85	380.60	19.96
> 37	0.000616	0.000032	20.94	1.10	9.55	0.50

The surface temperature map shows that in 2010, areas with high temperatures above 30^{o}C only accounted for 10.35% of the area (197.21 km^2); the majority of the areas had temperatures below 30^{o}C, accounting for 1,709.46 km^2 (89.65% area) (Figure 6a). Surface temperature map reveal that the study area has a substantial temperature change by 2016 and 2021. Areas with temperatures below 30^{o}C only account for 44.96% and 36.56% of the area, respectively. Whereas areas with temperatures over 30^{o}C increased five times and six times compared to 2010, accounting for 55.31% and 63.44% of the area, respectively (Figures 6b, 6c).

Surface temperatures rise in regions with poor vegetation, such as construction areas, as well as high mountain areas exposed to sunshine. The results show that temperatures exceeding 37^{o}C in BR-VT province tend to steadily rise during the dry season. According to Table 8 and

Figure 5, the image analysis results in 2010 almost did not reveal a temperature above 37°C, but this temperature existed with an area of 20.94 km^2 by 2016 and 9.55 km^2 by 2021. In contrast, areas with temperatures below 24°C tend to decrease sharply in the dry season, from 213.24 km^2 in 2010 to 21.95 km^2 in 2016 and 0.04 km^2 in 2021. Temperatures of 24-30°C are expected to fall from 1,496.22 km^2 to 697.07 km^2 between 2010 and 2021. While the temperature level from 30 to 37°C gradually increases, the area increased from 197.21 km^2 in 2010 to 1,054.59 km^2 and 1,200.05 km^2 in 2016 and 2021, respectively. The majority of the area is concentrated in Ba Ria and Vung Tau cities, Long Dien district, Phu My town. The Xuyen Moc and Dat Do districts also have an increase in heat, but not much, mainly coming from the formation of many housing projects for residents or coastal tourism regions.

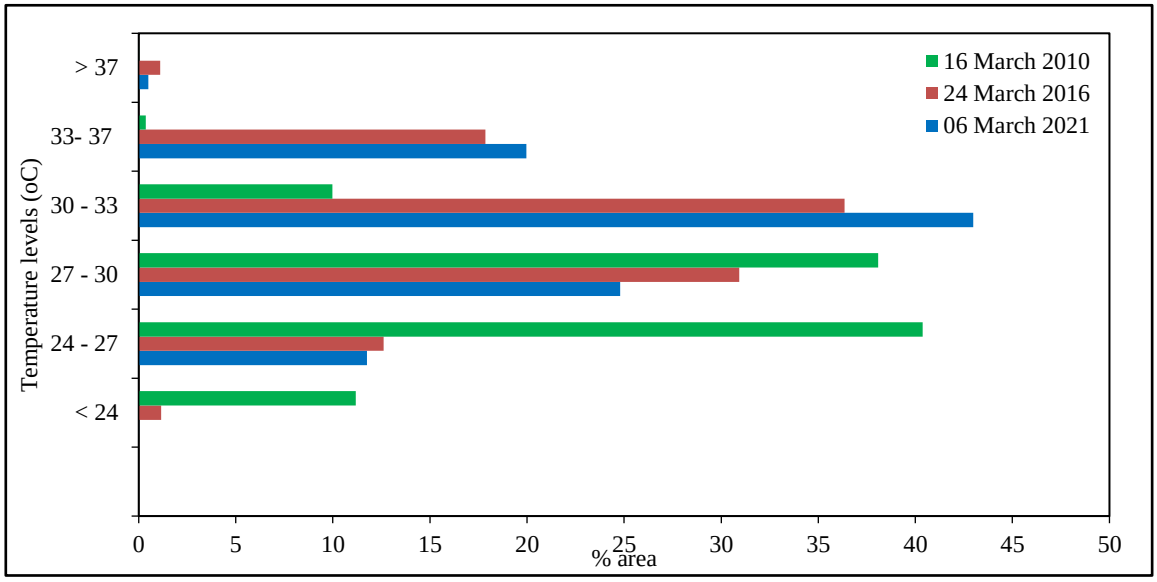

Figure 5. Comparison chart of land surface temperature analysis results.

From the results of land surface temperature, NDVI, and the land cover classification maps of the study area from 2010 to 2021, it shows that vegetation has definitely declined in most districts in the province within 11 years (except Chau Duc and Xuyen Moc districts). The reason is that since 2010, the area's population growth rate has expanded significantly along with the growth of the economy, with the formation of many factories, enterprises, or industrial zones, leading to a large demand for human resources and a large amount of labor. This results in a strong trend of industrialization, urbanization, and tourism services in coastal districts and cities, causing the vegetation area to be converted to residential land and construction land.

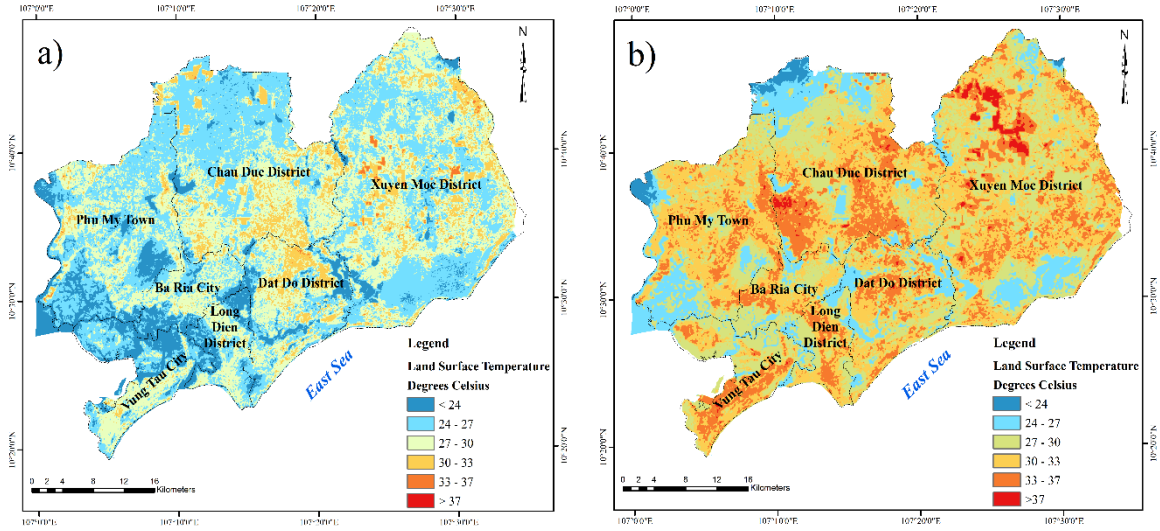

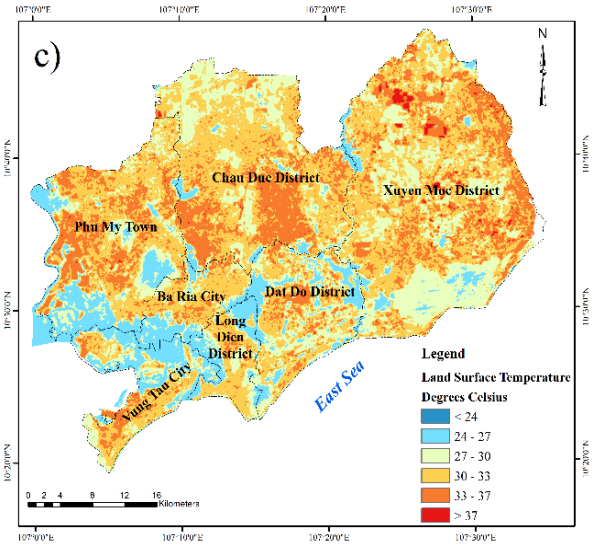

Figure 6. Land surface temperature of Ba Ria - Vung Tau province: (a) 16 March 2010; (b) 24 March 2016; (c) 06 March 2021.

4. Conclusion

This study used Landsat images taken during the dry season to classify surface cover and survey surface temperature by estimating Normalised Difference Vegetation Index (NDVI).

The study's findings indicate that there was a notable increase in the BR-VT area's surface temperature between 2010 and 2021. In particular, in the dry season of 2021, the majority of the study region has a temperature of roughly 30-37ºC, a sixfold increase over 2010, concentrated in building zones, residential areas, roadways (impervious surfaces), and vacant land. Meanwhile, compared to 2010, areas with fields, forests, plantations (vegetation), and networks of reservoirs and rivers with temperatures ranging from 24 to 30ºC account for only 36.55% of the area.

According to these findings, the land surface temperature in BR-VT province has fluctuated significantly over the years. At the same time, it demonstrates that vegetation cover and activity by humans have a significantly affect the surface temperature in the area. The study provides to giving information to assist managers in taking suitable actions in sustainable urban planning and development, therefore reducing the impact of rising surface temperatures on the urban environment in the context of climate change.

Author contribution statement: Conceptualization, methodology, analyzed and interpreted the data, writing - review, editing and project administration: N.H.A.

Acknowledgements: This research is funded by Vietnam National University Ho Chi Minh City (VNU-HCM) under grant number: TX2024-24-01.

Competing interest statement: The author declare no conflict of interest.

References

1. Hu, W.; Zhou, W.; He, H. The effect of land-use intensity on surface temperature in the Dongting Lake area, China. *Adv. Meteorol.* **2015**, 1–11.
2. Bokaie, M.; Zarkesh, M.K.; Arasteh, P.D.; Hosseini, A. Assessment of urban heat island based on the relationship between land surface temperature and land use/ land cover in Tehran. *Sustainable Cities Soc.* **2016**, *23*, 94–104.
3. Himayah, S.; Ridwana, R.; Ismail, A. Land surface temperature analysis based on land cover variations using satellite imagery. *IOP Conf. Ser.: Earth Environ. Sci.* **2020**, *500(1)*, 012019.
4. Jiang, J.; Tian, G. Analysis of the impact of land use/land cover change on land surface temperature with remote sensing. *Procedia Environ. Sci.* **2010**, *2*, 571–575.
5. Igun, E.; Williams, M. Impact of urban land cover change on land surface temperature. *Global J. Environ. Sci. Manage.* **2018**, *4(1)*, 47–58.

6. Kayet, N.; Pathak, K.; Chakrabarty, A.; Sahoo S. Spatial impact of land use/land cover change on surface temperature distribution in Saranda Forest, Jharkhand. *Model. Earth Syst. Environ.* **2016**, *2(3)*, 1–10.
7. Mohamed, A.; Bernard, A.E. Application of remote sensing techniques and geographic information systems to analyze land surface temperature in response to land use/land cover change in greater Cairo region, Egypt. *J. Geogr Inf. Syst.* **2018**, *10*, 57–88.
8. Mehdi, B.; Mirmasoud, K.Z.; Peyman, Daneshkar A.; Ali, H. assessment of urban heat island based on the relationship between land surface temperature and land use/land cover in Tehran. *Sustainable Cities Soc.* **2016**, *23*, 94–104.
9. Shivakumar, B.R.; Rajashekararadhya, S.V. An investigation on land cover mapping capability of classical and fuzzy based maximum likelihood classifiers. *Int. J. Eng. Technol.* **2018**, *7(2)*, 939–947.
10. Huy, N.A.; Trang, N.T.D.; Nguyen, N.T.T; Trong, T.V.; Son, T.V. Application of remote sensing of Ho Chi Minh city's surface temparature in period 2016–2020. *VN J. Hydrometeorol.* **2021**, *729(9),* 29–39.
11. Tuyet, N.H.A.; Than, N.H. Application of remote sensing to assess the variation of land surface temperature in Dau Tieng District, Binh Duong province in the context of Climate change in the phase of 2004-2019. Proceeding of Earth and environmental sciences, **2019**, 357–360.
12. Anh, L.V.; Tuan, T.A. Estimation of land surface temperature using emissivity calculated from normalized difference vegetation index. *VN J. Earth Sci.* **2014**, *36(2)*, 184–192.
13. Van, T.T; Bao, H.D.X. Study of the impact of urban development on surface temperature using remote sensing in Ho Chi Minh City, Southern Vietnam. *Geogr. Res.* **2010**, *48(1)*, 86–96.
14. United States Geological Survey. Online available: earthexplorer.usgs.gov.
15. Department of the Interior U.S. Geological survey 2019 Landsat 7 (L7) data users handbook, USA.
16. Department of the Interior U.S. Geological survey 2019 Landsat 8 (L8) data users handbook, USA.
17. LANDSAT Conversion to Radiance. Reflectance and at-Salittite brightness temperature (NASA).
18. Carlson, T.N.; Ripley, D.A. On the relation between NDVI, fractional vegetation cover, and leaf area index. *Remote Sens. Environ.* **1997**, *62(3)*, 241–252.
19. Vo, M.Q; Varnakovida, P.; Iabchoon, S.; Nguyen, D.T.H.; Nguyen, C.T. Analysis of factors affecting urban heat island phenomenon in Bangkok metropolitan area, Thailand. *VNU J. Sci.: Earth Environ. Sci.* **2019**, *35(1)*, 53–62.
20. Sobrino, J.A.; Jiménez-Muñoz, J.C.; Paolini, L. Land surface temperature retrieval from LANDSAT TM 5. *Remote Sens. Environ.* **2004**, *90(4)*, 434–440.
21. Nugraha, A.S.A.; Gunawan, T.; Kamal, M. Comparison of land surface temperature derived from Landsat 7 ETM+ and Landsat 8 OLI/TIRS for drought monitoring. *IOP Conf. Ser.: Earth Environ. Sci.* **2019**, *313(1)*, 012041.

Appendix

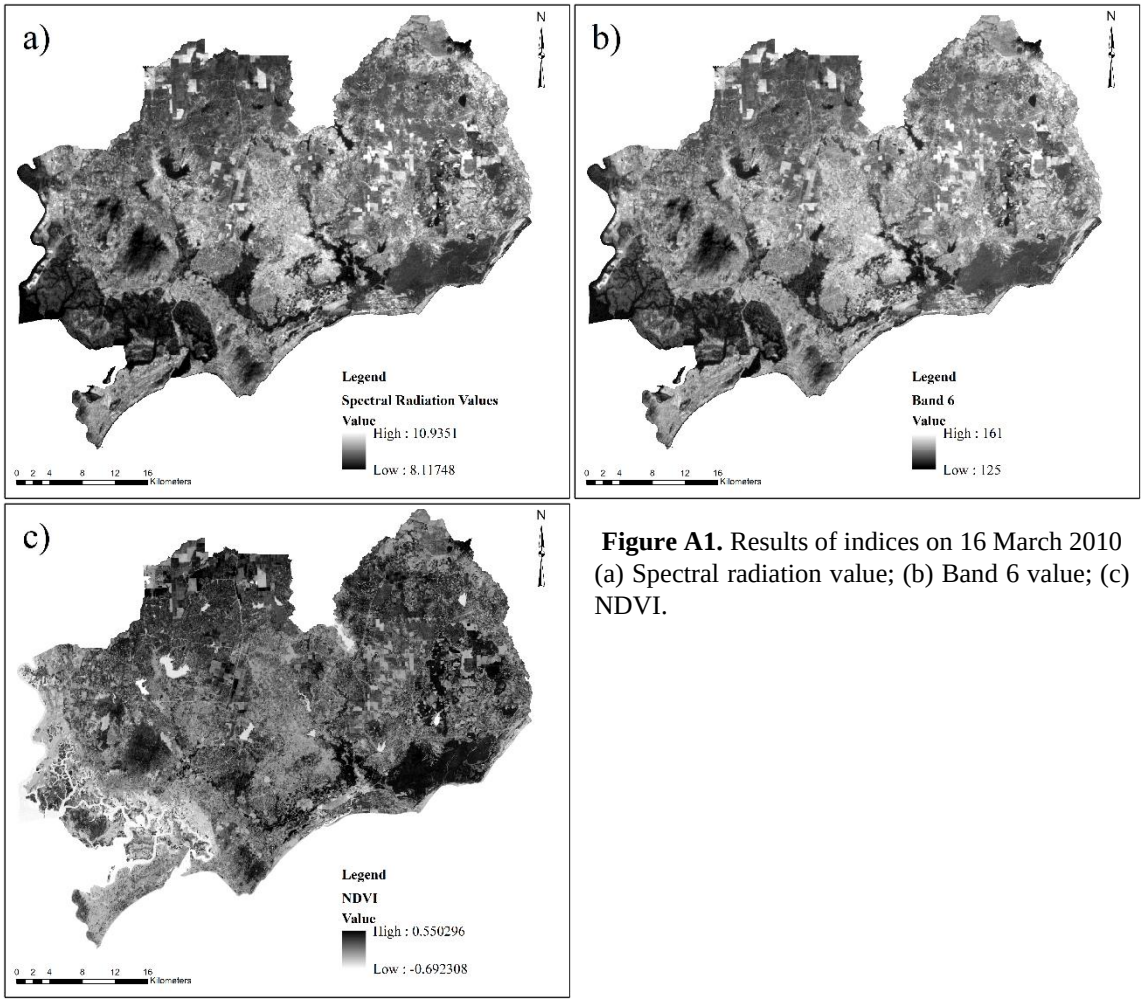

Figure A1. Results of indices on 16 March 2010 (a) Spectral radiation value; (b) Band 6 value; (c) NDVI.

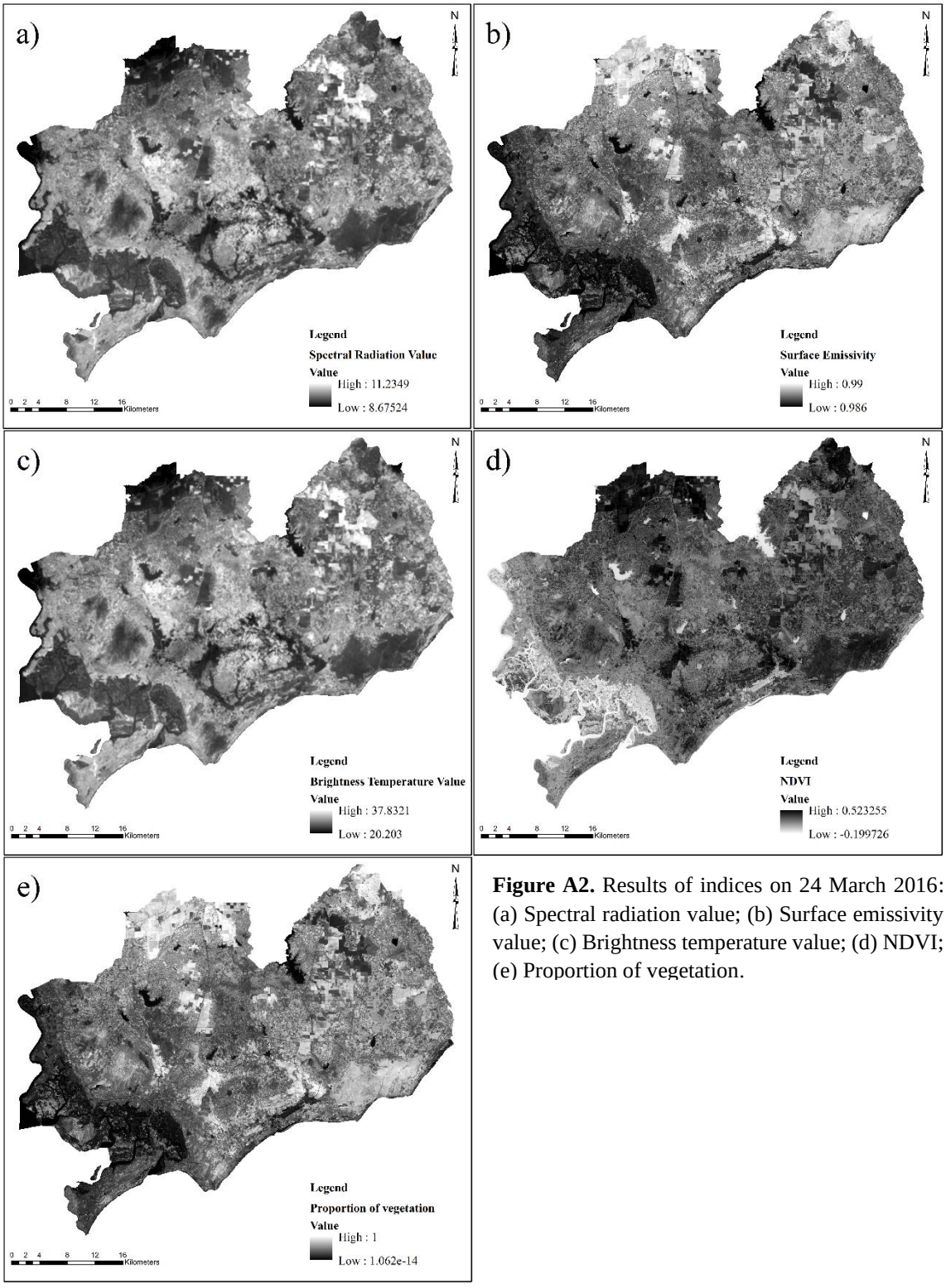

Figure A2. Results of indices on 24 March 2016: (a) Spectral radiation value; (b) Surface emissivity value; (c) Brightness temperature value; (d) NDVI; (e) Proportion of vegetation.

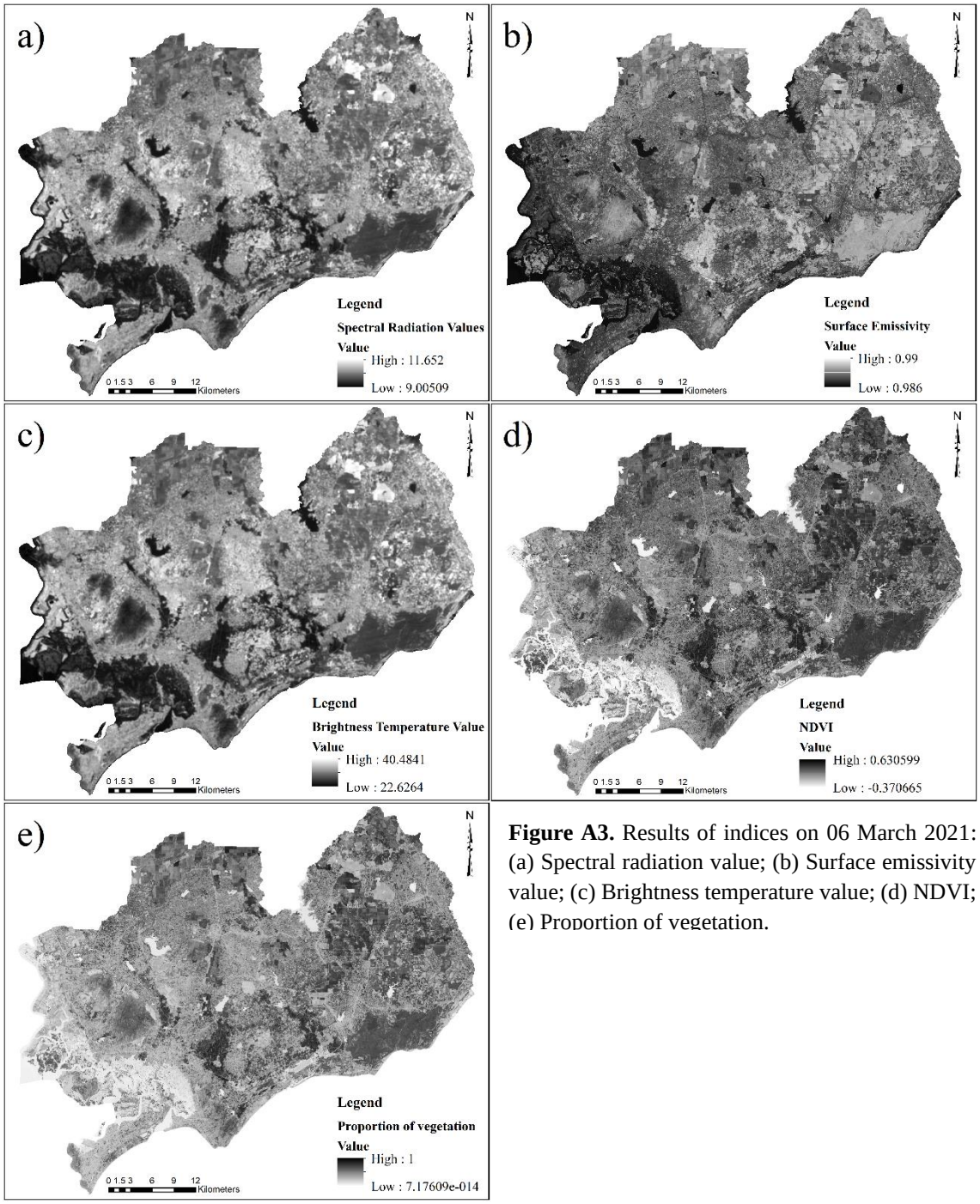

Figure A3. Results of indices on 06 March 2021: (a) Spectral radiation value; (b) Surface emissivity value; (c) Brightness temperature value; (d) NDVI; (e) Proportion of vegetation.

JOURNAL OF
HYDRO-METEOROLOGY

Research Article

Assessment of household adaptive capacity to disasters: Two comparative case studies in Central Vietnam

Nguyen Thao Ly[1,2], Tran Thi Huong[1], Yuki Ishikawa - Ishiwata[1,3], Nguyen Thuy Duong[1], Nguyen Thu Hien[4], Yeshus Umesh[1], Nguyen Thi Hoang Ha[1]*

[1] VNU Vietnam Japan University, Vietnam; thaolyn97@gmail.com; huongtt.vngecc@gmail.com; yuki.ishikawa.ga@vc.ibaraki.ac.jp; nt.duong@vju.ac.vn; yashuscc@gmail.com
[2] The Deutsche Gesellschaft für Internationale Zusammenarbeit (GIZ) GmbH; thaolyn97@gmail.com
[3] Global and Local Environment Co-creation Institute (GLEC), Ibaraki University; yuki.ishikawa.ga@vc.ibaraki.ac.jp
[4] Department of Climate Change, Ministry of Natural Resources and Environment; thuhien7585@gmail.com

*Corresponding author: nth.ha@vju.ac.vn; hoangha.nt@vnu.edu.vn; Tel.: +84–968046008

Received: 15 March 2024; Accepted: 20 April 2024; Published: 25 June 2024

Abstract: This paper presents comparative case studies between an ancient town in Quang Nam province (QN town), and a commune in Da Nang city (DN commune) in order to quantitatively assess the adaptive capacity of households in response to natural disasters. An indicator-based assessment with a set of 13 indicators is applied in this study. The results of 85 interviewed households in two study areas revealed that despite the higher probabilities of disaster occurrence, the households in QN town demonstrated better adaptive capacity compared to those in DN commune. The quantitative assessment (on a 0–1 scale) of adaptive capacity in the QN town and DN commune showed the values of 0.61 and 0.55, respectively. QN town had higher adaptive capacity than DN commune due to higher income stability, better preparedness measures for disasters, higher percentages of households receiving disaster warning information, better accessibility to clean water, healthcare service, food, and financial support during and after disasters. Conversely, DN commune demonstrated higher insurance coverage, higher percentages of households participating in social organizations, and receiving social support during and after disasters. Drawing from the findings that influence the difference in adaptive capacity levels between households in QN town and DN commune, the study subsequently proposes the recommendations for policymakers and individuals in both areas to improve their long-term prevention and preparedness strategies, enabling them to effectively respond to natural disasters.

Keywords: Adaptive capacity; Disaster; Indicator; Household; Vietnam; Vulnerability.

1. Introduction

Natural hazards are defined as environmental phenomena that pose possible impacts on societies and the human environment, especially in developing countries where the community faces greater exposure and vulnerability to climate-driven disasters [1]. As the threat of climate change continues to grow, it is imperative for human society to prioritize both mitigation and adaptation strategies in response to disasters [2]. Furthermore, it is recognized that natural disasters increase vulnerability to climate change, simultaneously

diminishes the ability to withstand risks, shocks, and stresses. Therefore, it is essential to enhance adaptive capacity by promoting and supporting adaptive measures, contributing to reduction of climate change vulnerability [3]. Adaptation entails developing the capacity to adjust system components, structures, and processes in response to anticipated or observed long-term changes, such as alterations in the frequency of hazardous events [4]. It is, therefore, crucial to comprehend, evaluate, and enhance adaptive capacity in order to facilitate adaptive measures and mitigate climate change impacts [5].

A variety of studies assessed the adaptive capacity to disasters using both secondary data and primary data (e.g., interviews, surveys, and focus group discussion) [6]. Specifically, Bossio et al. [7] identified the adaptive capacities in urban areas, underscoring the significance of governance and social institutions in shaping urban adaptive capacity. Recognizing the limitations of existing investments in improving the understanding of adaptive capacity in tropical coastal communities, Cinner et al. [8] proposed an approach that encompassed five key domains to build adaptive capacity, including assets for resilience, flexibility in strategies, collective organization, and action, learning and responsiveness to change, and agency in decision-making, while also highlighting strategies for their development. Nguyen et al. [9] identified significant variations in adaptive capacity across different regions in Vietnam, highlighting specific areas that require urgent attention to enhance their resilience to typhoons, which can inform national disaster risk reduction initiatives and guide the development of effective mitigation strategies for long-term sustainability. Aalst [10] also supported Nguyen et al. [9] that even though the households were highly vulnerable due to climate change, it is possible to enhance the resilience of the households by targeting the policy measures for the specific socioeconomic groups.

Gaining insights into and evaluating the adaptive capacity at the local level is necessary to initiate an understanding of how it can be fostered through broader development initiatives at both local and national scales [6]. Furthermore, households play a critical role within the intricate socio-natural system and are susceptible to the impacts of climate change. Therefore, conducting research on climate change adaptation at the household level is crucial for developing effective strategies to enhance adaptation and reduce vulnerability [11]. However, despite the critical role that household-level decisions play in shaping local and systemic vulnerability, there is a scarcity of research focused on assessing adaptive capacity to historical disaster events, particularly at the household level [6, 12].

Vietnam ranks among the world's most vulnerable countries to natural hazards [13]. Due to its geographic location and geographical conditions with a long coastline of 3,240 km, Vietnam has unique climate features, causing severe and diverse disasters in this area [14]. Accordingly, the country experiences high levels of exposure to disasters [3, 14]. Typhoons and floods are the most frequent hazards, impacting roughly 59% of Vietnam's landmass and affecting around 71% of its population [15]. Located downstream of the Vu Gia–Thu Bon River system in the South-Central Coast areas, Da Nang city and Quang Nam province have experienced several severe typhoons, floods, and inundation [16]. Meanwhile, the occurrence and severity of natural disasters have recently risen because of the influence of climate change [16]. The heightened frequency of intense rainstorms poses a significant threat of devastating floods to urban communities in Da Nang city, causing exacerbated social and physical damage in this area [16]. Despite reports of relatively high adaptive capacity among Da Nang city's urban households [11, 17], the historical typhoon-induced inundation that struck the city in October 2022 caused severe damage to human lives and properties [18]. This fact highlights the understanding of how households can adapt to exceptional disasters. Meanwhile, the increasing occurrence of severe floods in Quang Nam province has also significantly impacted communities' livelihoods and socio-economic development [19]. Additionally, within Quang Nam province, roughly 1.3% of the area is susceptible to flooding, with Hoi An city facing the highest risk (25.4% of the area), followed by Tam Ky (17.7% of the area) if the sea level rises

by 100 cm [20]. This climate-driven impact could exacerbate the annual inundation in these areas. The comparison of adaptive capacity to disasters between areas affected by high and low frequency of serious inundation may provide important implications for enhancing adaptive capacity of households.

This study aims to assess the adaptive capacity of households in response to natural disasters, focusing on typhoons, floods, and inundation in one of the most affected communes in Da Nang province and an ancient town in Quang Nam province, hereafter DN commune and QN town, respectively. The findings from this research are expected to provide valuable insights to inform the development of adaptation policies and guide municipal governance in these specific areas.

2. Materials and methods

2.1. Study areas

DN commune, located in the northwest of Da Nang city (Figure 1), is home to an average population of 47,338 people [21]. It is subjected to a tropical monsoon climate, with a rainy season from August to December and a dry season from January to July [17]. Furthermore, being part of Da Nang city, the commune is characterized by diverse topography, including mountains in the west and lowlands in the east, which contributes to increased flooding due to the proximity of the mountains to the coastline [22]. As a result, the study area frequently experiences severe disasters and extreme weather events [17, 22].

QN town is located on a coastal plain at the estuary of the Thu Bon River basin, in central Vietnam. The town's altitude varies from 70 to 517 meters above sea level, situated within a hot and humid tropical monsoon climate characterized by rainy seasons [23]. Accordingly, QN town, positioned in a low-lying delta near an estuary and coastal environment (Figure 1), is vulnerable to various natural impacts, with the primary threat being floods during rainy seasons due to changes in land use in the town and surrounding areas which are exacerbated by approximately 25% of Vietnam's typhoons affecting the area [23, 24].

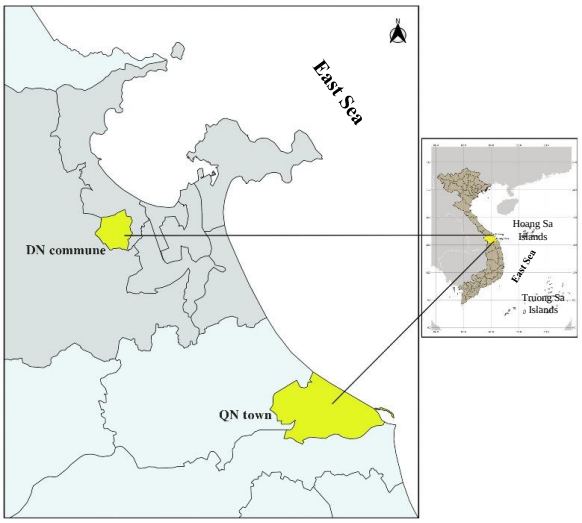

Figure 1. The study areas in DN commune and QN town.

2.2. Theoretical framework and indicator-based assessment

Adaptive capacity refers to the capability of systems, institutions, humans, and other organisms to adapt and respond to potential damages, capitalize on opportunities, and address the consequences of change [25]. The process of adaptation necessitates the ability to learn from past experiences in order to effectively manage the current climate conditions and apply those lessons to cope with future climate changes, even in the face of unexpected events. Therefore, to assess the preparedness and adaptation of systems to climatic events, it would

be necessary to examine multiple time periods encompassing the period before, during, and after the event [26]. According to Engle [27], if the system underwent adaptation or adjustment, regardless of whether it suffered negative consequences from the prior event, it implies the presence of inherent capacity to do so. Consequently, examining the factors that either facilitated or hindered these adaptations, as well as where they occurred or did not occur, can enhance comprehension of adaptive capacity dynamics.

However, our understanding of adaptive capacity is continuously evolving, and there is currently a lack of consensus regarding its distinct characteristics and determinants at the national, community, or household level [28]. In addition, the successful implementation of adaptation strategies necessitates various resources, such as financial, social, human, and natural capitals. The specific types of required resources, and their relative significance depend on the context in which adaptation is pursued, the nature of the hazards faced, and the characteristics of the adaptation strategy itself [29]. To tackle this challenge, various methods have been developed to assess adaptive capacity, utilizing an indicator-based approach. Ramieri et al. [30] assessed coastal vulnerability using a range of independent variables, merged into a composite index covering drivers, risks, hazards, exposure, sensitivity, impacts, adaptive capacity, and damage. It enables a thorough evaluation of various coastal vulnerability aspects within a unified assessment framework. In addition, 19 indicators, emphasizing diverse aspects such as economic resources, infrastructure, social capital, institution, were identified and considered crucial elements in measuring adaptive capacity to assess the adaptive capacity of farmers in Mexico [31]. Mai et al. [11] developed a set of 17 indicators to assess the socio-economic status of urban households, focusing on inherent capacity and municipal services for urban area stability and security.

In this paper, a composite indicator framework [32] using 13 indicators for quantitative assessment of adaptive capacity was proposed (Table 1; Figure 2). Indicators were selected based on their relevance, methodological soundness, and data reliability, availability and accessibility [32]. Indicators (AC2–AC7) were referenced from Mai et al. [11], other indicators were proposed to measure the adaptive capacity in a timely manner for the historical disaster event in October 2022 affecting the study areas for proactive adaptation of future events (Figure 2).

Table 1. Indicators for adaptive capacity assessment in two study areas.

Code	Indicators	Descriptions	Calculation
AC1	Income stability	Accessibility to income stability during disasters	Equation (1)
AC2*	Livelihood diversity	Number of livelihood sources per household	Equation (1)
AC3*	Housing condition	Categories of housing conditions based on structure, permanence, and number of floors	Equation (1)
AC4*	Insurance coverage	Percentage of households with health insurance Percentage of households with property insurance	Ratio (%)
AC5*	Education	Number of people who have graduated above secondary level	Equation (1)
AC6*	Preparedness measures	Number of disaster mitigation tools equipped by households	Equation (1)
AC7*	Social organizations	Number of social organizations that household members are affiliated	Equation (1)
AC8	Social support	Percentage of households receiving support during and post-disasters	Ratio (%)
AC9	Disaster warning information	Percentage of households receiving disaster warning information	Ratio (%)
AC10	Accessibility to clean water	Accessibility to clean water during and post-disasters	Equation (1)
AC11	Accessibility to healthcare service	Accessibility to healthcare service during and post-disasters	Equation (1)
AC12	Accessibility to food	Accessibility to food during and post-disasters	Equation (1)
AC13	Accessibility to financial support	Accessibility to financial support during and post-disasters	Equation (1)

Note: *Mai et al. [11].

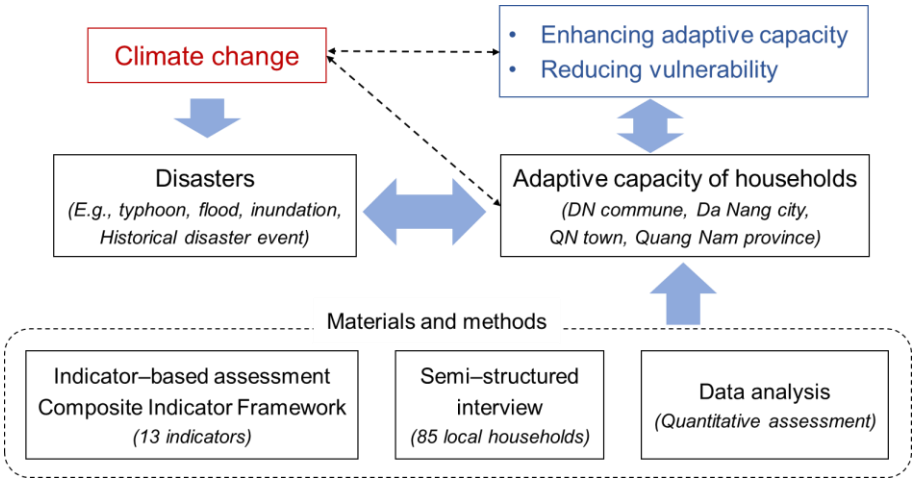

Figure 2. Framework for indicator-based assessment of adaptive capacity to disasters.

2.3. Sociological survey

The questionnaire was developed in accordance with the proposed indicators for assessing adaptive capacity (Table 1). A semi-structured interview using a face-to-face method was conducted in the case study areas (Figure 2). A total of 85 households in DN commune and QN town were randomly selected to ensure a relatively even spatial distribution, various levels of impacts by disasters, and diversity of livelihoods.

2.4. Data analysis

The data corresponding to the indicators were coded, normalized by the Min-Max method (on a 0–1 scale) [33] using Eq. (1) as follows:

$$x_{ij} = \frac{X_{ij} - MinX_{ij}}{MaxX_{ij} - MinX_{ij}} \quad (1)$$

where, x_{ij} is the normalized value of indicator i of the household j; X_{ij} is the value of the indicator i corresponding to household j; Max and Min denote the maximum and minimum scaled values of indicator i, respectively.

Adaptive capacity of households to disasters in each study area was measured as follows:

$$AC = \frac{\sum_1^n AC_i}{n} \quad (2)$$

where, AC is the adaptive capacity of households to disasters; AC_i is the adaptive capacity measured by indicator i; n is the number of indicators.

The quantitative adaptive capacity levels of households to disasters in each study area were evenly classified based on a Likert scale (1–5) and a categorical scale by the OECD [32], as shown in Table 2 [34].

Table 2. Adaptive capacity assessment scale.

No.	Adaptive capacity level	Score
1	High adaptive capacity	0.81 – 1.00
2	Relatively high adaptive capacity	0.61 – 0.80
3	Medium adaptive capacity	0.41 – 0.60
4	Relatively low adaptive capacity	0.21 – 0.40
5	Low adaptive capacity	0.00 – 0.20

Quantitative assessment of adaptive capacity of households to disasters was conducted using Excel. A correlation coefficient was performed for correlation among 13 indicators using the SPSS 20.0 package.

3. Results

3.1. Adaptive capacity of households to disasters

Income stability (AC1): The results from interviews showed that over 39.5% of households located in DN commune were unable to access income stability during disasters, while 31.6% of interviewees in QN town encountered similar difficulties (Figure 3). Moreover, approximately 34.2% of households in QN town had full access to stable income. In contrast, only 9.3% of those in DN commune had a fully stable income during disasters.

Livelihood diversity (AC2): A majority of households in two study areas had one livelihood (88.6–92.5%) (Figure 4). QN town had a slightly higher percentage of households with at least two types of livelihoods compared to DN commune, corresponding to 5% and 4.5%, respectively (Figure 4). However, there was a larger proportion of households with no income source in DN commune, accounting for about 6.8% of total interviewees in that area, compared to QN town, where only 2.5% of households reported unstable income sources (Figure 4).

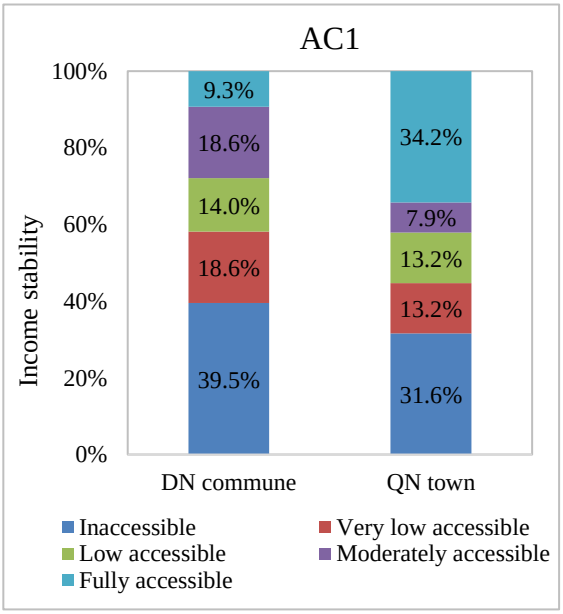

Figure 3. Percentage of households accessible to income stability during disasters (%).

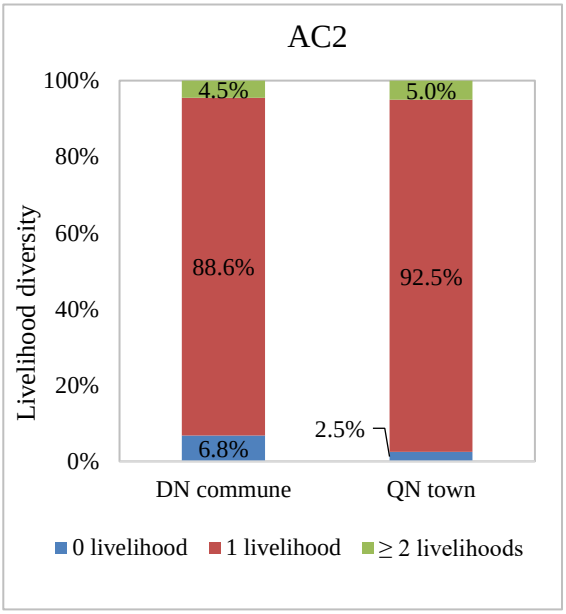

Figure 4. Percentage of households with number of livelihoods (%).

Housing condition (AC3): As located in the ancient heritage area, households in QN town were prohibited from renovating their houses, resulting in a significant proportion of IV-type houses and III-type houses, accounting for 62.5% and 32.5%, respectively (Figure 5). Meanwhile, despite being situated in the economic development and urbanization area, the proportion of IV-type houses among the interviewed households in DN commune was higher than that in QN town, accounting for 72.7% of interviewees. Additionally, the rate of temporary houses was also significantly higher in DN commune compared to QN town, with approximately 13.6% and 2.5%, respectively.

Insurance coverage (AC4): Most interviewees in DN commune and QN town participated in health insurance, with 84.1% and 77.5%, respectively (Figure 6). Meanwhile, none of the interviewees in both areas participated in property insurance, possibly due to a lack of awareness and understanding about the importance and benefits of property insurance, particularly regarding the risks associated with potential property damage or loss from natural disasters.

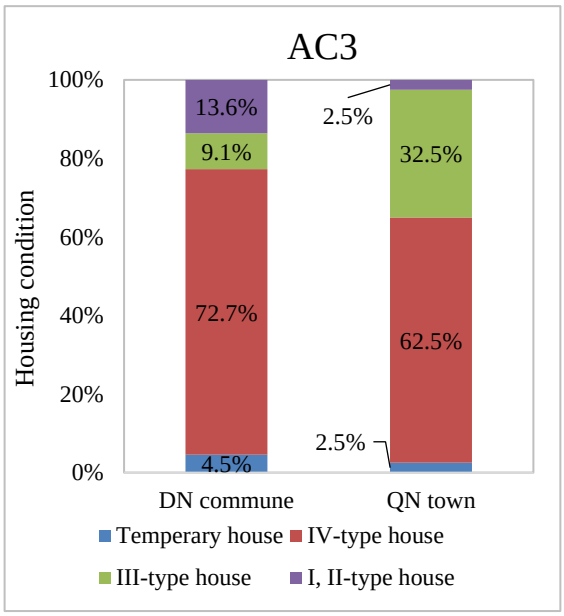

Figure 5. Percentage of households with various housing condition categories (%).

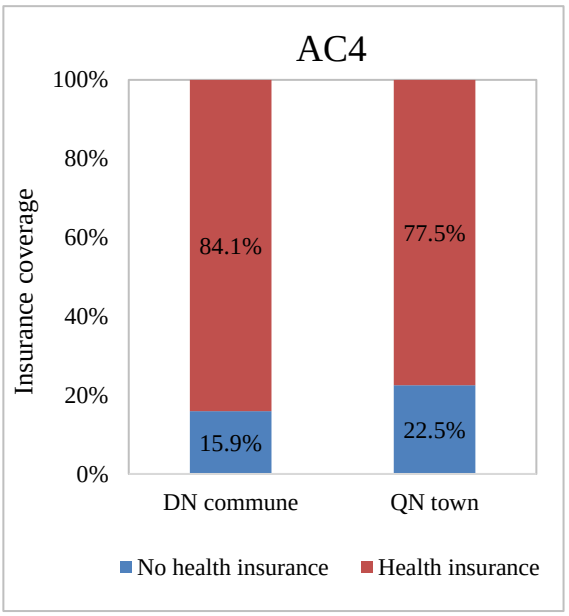

Figure 6. Percentage of households with health insurance coverage (%).

Education (AC5): Most of the interviewees in DN commune and QN town had a secondary degree or higher (Figure 7). The percentage of interviewees who have graduated above the secondary level in QN town was only 18.4%, while in DN commune, the figure was slightly higher at about 20.9% (Figure 7).

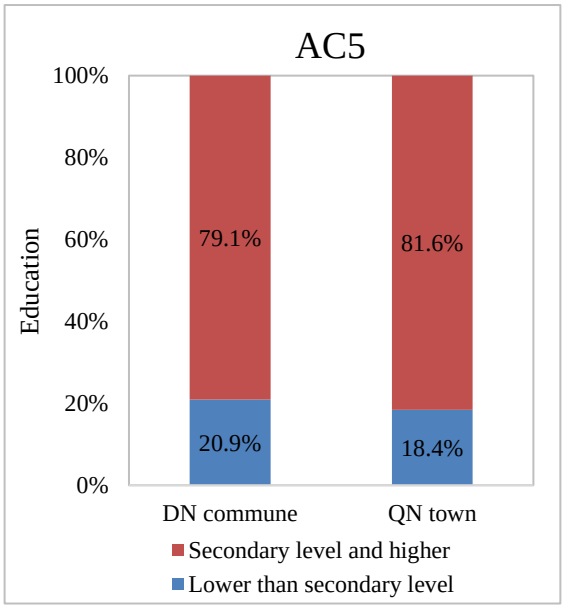

Figure 7. Percentage of interviewed people with education level (%).

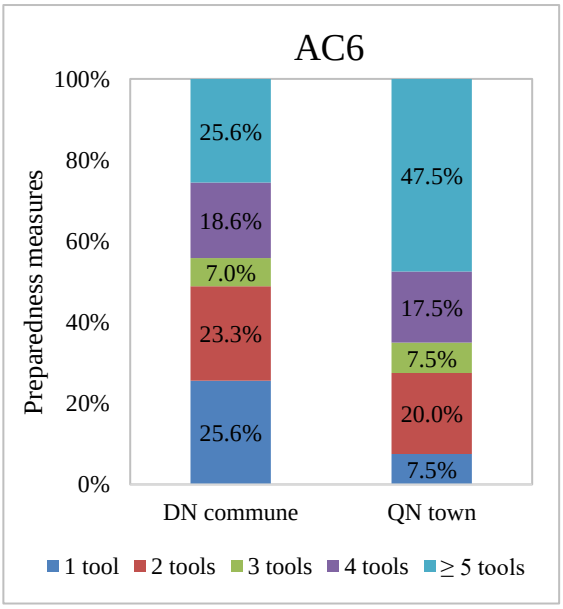

Figure 8. Percentage of households equipped with disaster mitigation tools (%).

Preparedness measures (AC6): Approximately 47.5% of interviewed households in QN town were equipped with more than 05 disaster adaptation tools, while in DN commune, only 25.6% of interviewees had the same level of preparedness (Figure 8). According to the interview results, it is notable that a large majority of the interviewees have been long-term residents of QN town with nearly 98% residing there for over a decade. In contrast, in DN commune, around 40% of the households interviewed had a relatively shorter period of residency, being residents for less than 10 years (Figure 8). It could be seen that the sampled

households living in their current residence for a longer duration were more likely to have a higher possibility of taking better preparedness measures.

Social organization (AC7): The survey results showed that most of the interviewees in QN town did not participate in social organizations (83.8%), whereas in DN commune, the participation rate was higher, with more than 32.6% of the total interviewed households being involved in social organizations (Figure 9).

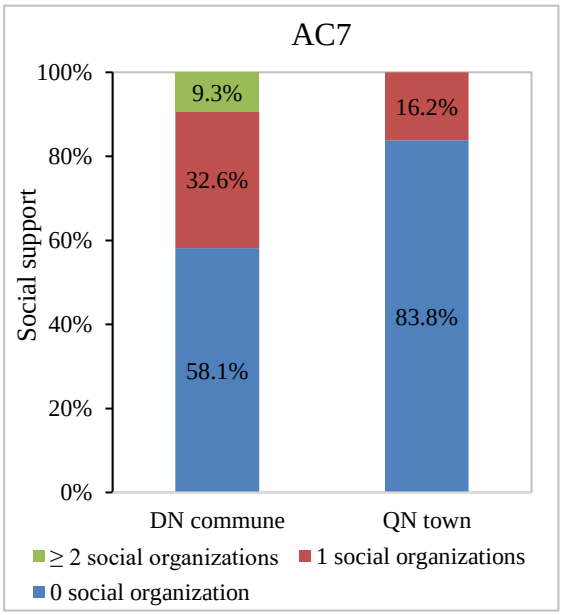

Figure 9. Percentage of households participated in social organizations (%).

Social support (AC8): In DN commune, 68.3% of households reported receiving no social support during disasters (Figure 10), causing a lack of preparedness and resources to cope with the challenges posed by disasters. On the other hand, in QN town, a higher percentage of households, which accounted for 85%, indicated a similar absence of social support. In addition, in terms of social support after disasters, DN commune had a higher percentage of households with access to support after disasters, accounting for 53.7% of interviewees, compared to QN town, where only 32.5% of households had access to support (Figure 10). The interview indicated that in QN town, where floods occur frequently, both the local government and people were experienced in dealing with extreme weather events, reducing the need for extensive support. However, in DN commune, where inundation was less common, local authorities may be less proactive in their response due to lower frequency.

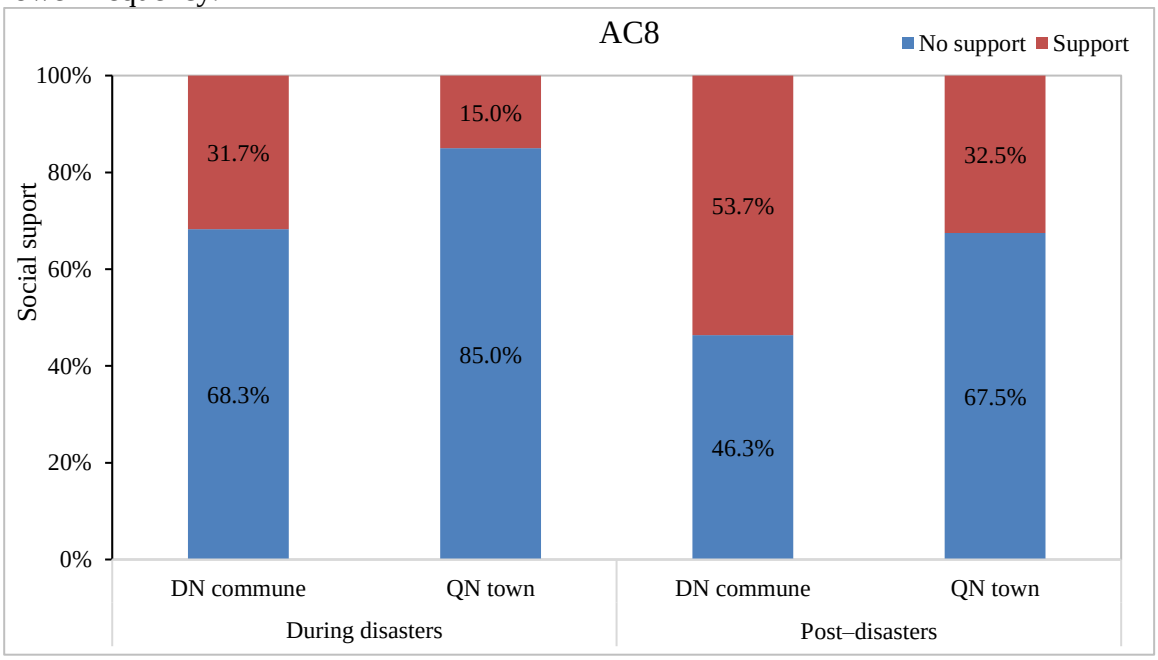

Figure 10. Percentage of households receiving support during and post-disasters (%).

Disaster warning information (AC9): Most interviewees in both DN commune and QN town, approximately 85.2% and 97.1% respectively, reported receiving disaster warning information (Figure 11).

Accessibility to clean water (AC10): 57.5% of interviewees had full access to clean water, the percentage in DN commune was dramatically lower, with only 18.2% having full access to clean water during disasters (Figure 12). After the disasters, the percentages of households fully accessible to clean water increased to 64.7% and 29.7% in QN town and DN commune, respectively (Figure 12). The difference in access to clean water between QN town and DN commune may be attributed to various factors. In QN town, houses with additional garrets provide shelter and minimize damage during disasters. However, households in DN commune lacked renovation options and faced challenges in disaster response. Timely information and disaster response experience also differed between the two areas.

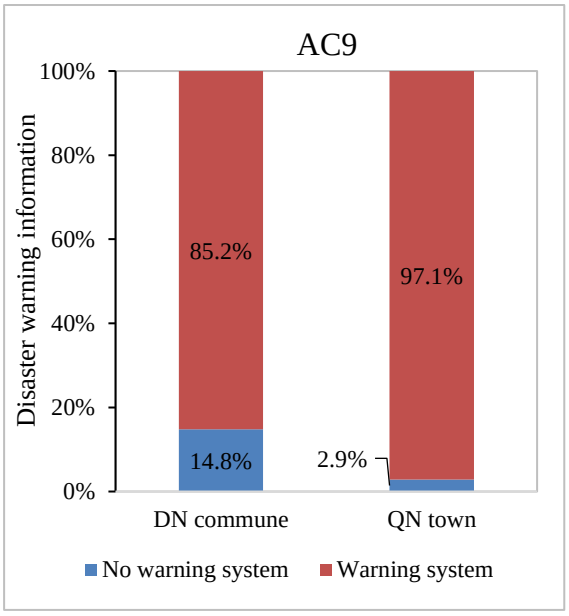

Figure 11. Percentage of households receiving disaster warning information (%).

Accessibility to healthcare service (AC11): The percentage of households in QN town and DN commune fully accessible to healthcare service during the disasters were 65.0% and 25.6%, respectively (Figure 13). We also found a high percentage of households in DN commune inaccessible to healthcare service during the disasters (37.2%), mainly resulting from the historical disaster in October 2022. Approximately 76.5% of interviewees located in QN town had full access to healthcare (AC11) after natural disaster events. Meanwhile, in DN commune, the figure was significantly lower, with only 47.1% having access to healthcare. The interview indicated that the households in QN town were well-acquainted with the flood situation in the region. Consequently, they prepared by stocking up on food and taking steps to relocate the elderly or vulnerable family members to hospitals nearby.

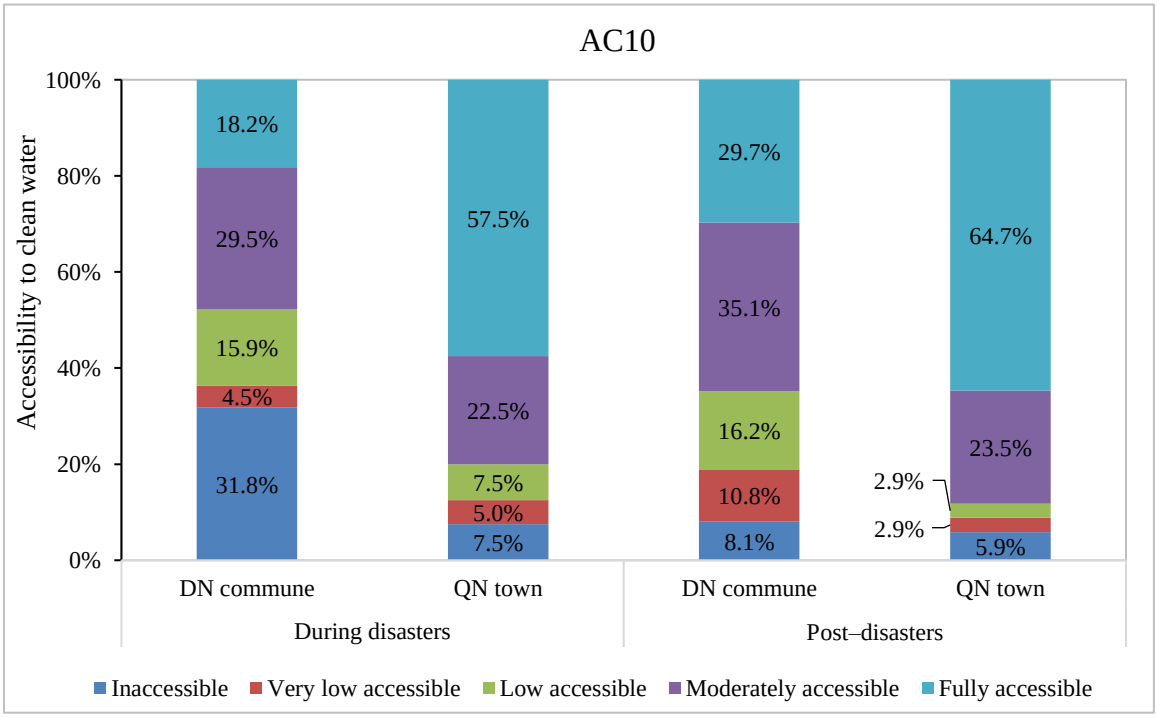

Figure 12. Percentage of households accessible to clean water during and post-disasters (%).

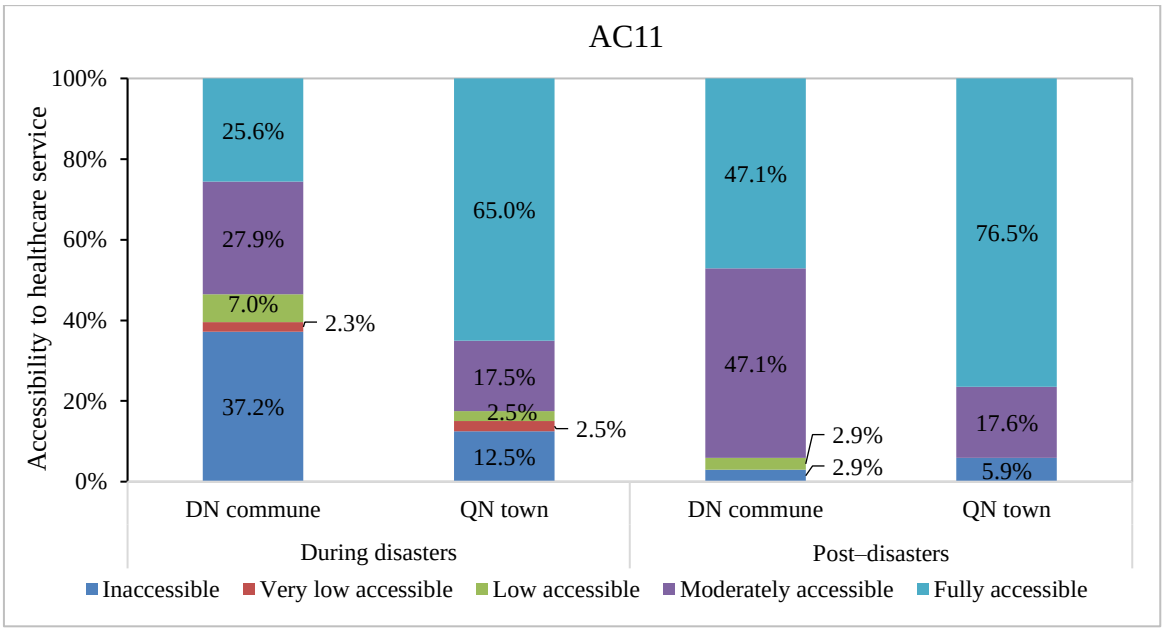

Figure 13. Percentage of households accessible to healthcare service during and post-disasters (%).

Accessibility to food (AC12): The interview results of this study showed a high percentage of households (72.5–78.1%) in QN town having full accessibility to food during and after disasters, implying a good response to high frequency of disaster in this area (Figure 14). In DN commune, percentages of households that had moderate and full accessibility to food during and after disasters were 64.5% and 87.5%, respectively (Figure 14).

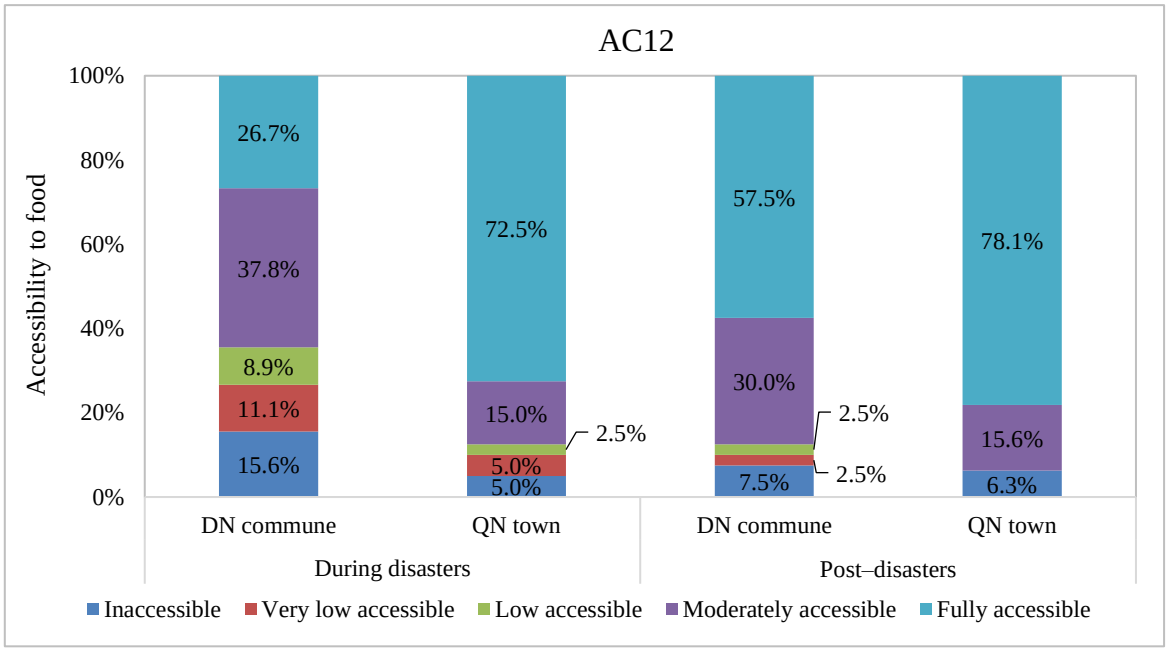

Figure 14. Percentage of households accessible to food during and post-disasters (%).

Accessibility to financial support (AC13): The result demonstrated high percentages of households in DN commune (65.8%) and QN town (52.8%) who were not accessible to financial support during disasters (Figure 15). After the disasters, 50% of interviewees in DN commune reported not receiving any financial support, while the figure for QN town was lower at 29% (Figure 15). Furthermore, only about 9.4% of households in DN commune fully accessed financial support, while in QN town, the percentage was higher at 19.4% (Figure 15).

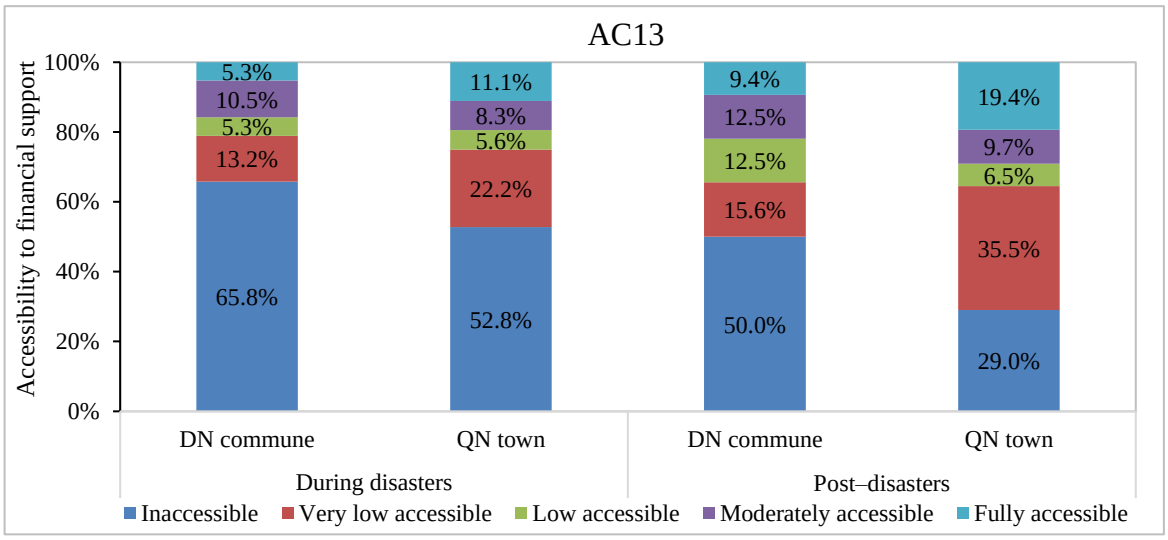

Figure 15. Percentage of households accessible to financial support during and post-disasters (%).

The averages of adaptive capacity variables are shown in Figure 16 for households in two study areas. In which, QN town was assessed at relatively high adaptive capacity with an average value of 0.61, while DN commune stands at medium adaptive capacity with an average value of 0.55. The data showed that both study areas stated the relatively same level of adaptive capacity in livelihood diversity (AC2), housing condition (AC3), and education (AC5) (Figure 16). Meanwhile, QN town had a higher adaptive capacity level compared to DN commune in terms of income stability (AC1), preparedness measures (AC6), disaster warning information (AC9), accessibility to clean water (AC10), healthcare service (AC11), food (AC12), and financial support (AC13) (Figure 16). In contrast, DN commune demonstrated higher adaptive capacity than QN town in terms of insurance coverage (AC4), social organizations (AC7), and social support (AC8) (Figure 16).

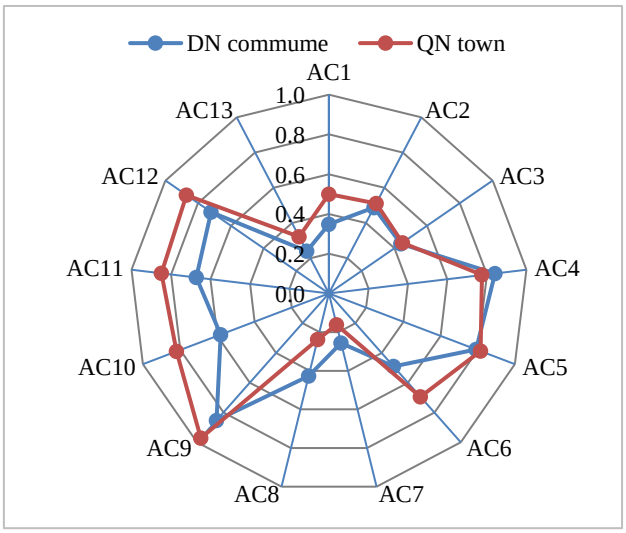

Figure 16. Adaptive capacity of households to disasters.

3.2. Correlation among adaptive capacity indicators

Table shows the correlations among adaptive indicators in DN commune and QN town. The income stability (AC1) was significantly correlated with education (AC5; $r = 0.33$, $p < 0.05$), preparedness measures (AC6; $r = 0.35$, $p < 0.05$), accessibility to clean water (AC10; $r = 0.40$, $p < 0.05$), healthcare service (AC11; $r = 0.43$, $p < 0.05$), and food (AC12; $r = 0.37$, $p < 0.05$). The significant correlation between preparedness measures (AC6) and accessibility to clean water (AC10; $r = 0.31$, $p < 0.05$), healthcare service (AC11; $r = 0.35$, $p < 0.05$) and

food (AC12; r = 0.33, p < 0.05) were also observed. Similarly, insurance coverage (AC4) and financial support during and post–disaster accessibility (AC13) were correlated (r = 0.23, p < 0.05). In addition, accessibility to clean water (AC10) were correlated with accessibility to healthcare service (AC11; r = 0.77, p = 0.05), food (AC12; r = 0.7, p < 0.05) and financial support during and post-disaster accessibility (AC13; r = 0.36, p < 0.05).

Table 3. Correlation coefficients among adaptive capacity indicators of DN commune and QN town.

	AC1	AC2	AC3	AC4	AC5	AC6	AC7	AC8	AC9	AC10	AC11	AC12	AC13
AC1	1.00												
AC2	0.14	1.00											
AC3	0.00	0.00	1.00										
AC4	-0.11	-0.10	0.15	1.00									
AC5	**0.33**	0.20	0.00	0.00	1.00								
AC6	**0.35**	0.15	0.13	0.02	0.15	1.00							
AC7	-0.02	0.06	-0.02	0.22	0.03	0.03	1.00						
AC8	-0.20	-0.05	-0.13	0.15	0.00	0.04	-0.01	1.00					
AC9	0.16	-0.19	-0.06	-0.01	0.01	0.07	**-0.31**	0.14	1.00				
AC10	**0.40**	-0.08	0.14	-0.10	-0.09	**0.31**	**-0.23**	-0.19	0.08	1.00			
AC11	**0.43**	0.04	0.15	-0.05	0.06	**0.35**	-0.13	**-0.23**	0.13	**0.77**	1.00		
AC12	**0.37**	0.02	0.14	0.00	0.08	**0.33**	-0.15	-0.16	0.24	**0.70**	**0.84**	1.00	
AC13	0.23	-0.03	0.16	**0.23**	0.02	-0.07	0.07	-0.16	0.02	**0.36**	**0.25**	**0.30**	1.00

*Pearson correlation significance (p < 0.05) is bold.

4. Discussion

This study utilized an indicator-based method with 13 indicators to evaluate the adaptive capacity of DN commune and QN town to natural disasters, especially typhoons, floods, and inundation. Accordingly, results from the analysis of semi-structured interviews from a total of 85 households in two study areas revealed the complex and complementary interaction among identified adaptive indicators and adaptive capacity of households to respond to typhoons, floods, and inundation. A comparison between DN commune and QN town enhances the understanding of which concepts shaped the ability to deal with climate risks and minimize the loss, thereby contributing effectively to the disaster prevention strategies for the regions.

The results from interviews indicated the low adaptive indicator score in income stability, and a medium average value of livelihood diversity and housing conditions in both study areas. Despite being located in areas of economic development and urbanization, the percentage of households with unstable income was high, leading to a reduction in the ability of households in response to and recovery from the impacts of natural disasters. Meanwhile, the findings of previous studies showed that the lack of economic resources in households leads to susceptibility to disasters due to the difficulties in accessing resources and ability to recover from disasters [35]. Furthermore, an increased level of households with stable income offers greater opportunities for enhancing housing conditions and acquiring durable assets [36]. However, people living in flood-and storm-affected areas in DN town, who often belong to low-income groups, frequently allocate a significant amount of their household income towards housing repairs or reconstruction after the annual floods and storms [37]. Houses situated in low-lying regions often lack safeguards against flooding, such as the absence of upper levels for storing valuable items during floods or the presence of sturdy and weighty roofs that are challenging to open for emergency escape [38]. Moreover, according to the results of interviews, it has been found that due to ongoing local railway construction plans over the past 18 years in DN commune have led to a prohibition on construction or renovation of houses for households living in the surrounding area, making them more vulnerable to natural disaster. A previous study found that individuals with unstable income tend to have a short-term perspective due to urgent and immediate issues that restrict their ability to invest

in housing resilient to typhoons [39]. Furthermore, renovations of houses in QN town are not permitted due to the area's significant historical value and commitment to preserving its ancient character. Thus, these previous findings support the explanation of the results from interviews regarding the medium adaptive indicator score of income stability and housing conditions. However, QN town usually experienced extended bouts of rain and deluges from upstream. When the water level of the Thu Bon River rises, this area is inevitably flooded. Households in QN town, accustomed to these conditions, have proactively implemented adaptation measures, including the construction of additional stories for shelter during floods. In contrast, the interview results indicated that the well-established urban environment and an advanced drainage system in DN commune contribute to a complacent attitude among residents towards inundation, leading to frequent neglect of precautionary actions against this natural calamity.

Previous research indicates that households with education levels beyond secondary are more likely to take preparedness measures [40]. Specifically, individuals with advanced education are increasingly likely to engage in preparedness measures such as their exposure to disasters, involvement in evacuation drills, knowledge about disasters, and the quantity of information sources they access [41]. Based on the findings of research, in comparison to DN commune, households located in QN town possess greater capacity to receive and absorb information and policies from local authorities due to a higher percentage of households having completed education beyond the secondary level. In addition, according to research findings, households located in QN town demonstrated a greater level of experience and higher probability of adopting preparedness measures against disasters than those who located in DN commune. One significant finding of previous research is that the duration of the current residence and the number of past disasters positively influence the probability of adopting preparedness measures [40]. Moreover, past flood experiences are the primary motivators for undertaking preparedness actions [42]. In QN town, the majority of households have resided there for over a decade, with some living in the community for up to 40 years, indicating a strong sense of long-term residency and stability. In contrast, in the DN commune, a significant number of households have relocated from other provinces and are deemed temporary residents. Consequently, DN commune exhibits a low adaptive capacity for preparedness measures, whereas QN town displays a high adaptive capacity of this indicator.

Social networks play a crucial role during the various phases of hazard and disaster events [43]. Sharing experiences among household members and community participation in flood risk reduction can encourage households to adopt proactive preparedness measures [42]. Furthermore, engaging in social networks can enhance knowledge and the capacity to prepare for future natural disasters [44]. Despite receiving warnings about typhoons and floods, households in both study areas demonstrated low to very low adaptive capacity for participating in social organizations, as indicated by their scores. However, the results revealed varying attitudes among households in QN town when discussing this information. They said that due to their extensive experience in flood and inundation preparedness, allowed both households and local authorities to be well-prepared and self-sufficient, eliminating the need for additional support. Conversely, the DN commune's households displayed a passive attitude towards flood prevention due to inadequate preparedness and limited knowledge sharing, leading to greater losses. Therefore, promoting awareness and sharing knowledge and experiences of the impacts and adaptation measures is essential to improve urban households' capacity to manage natural disasters [45].

Moreover, lack of infrastructure maintenance can lead to unsafe conditions and diminish the adaptive capacity to floods [46]. However, households in DN commune have lower adaptive capacity scores regarding food supply, healthcare service and clean water access compared to those in QN town. Interviews revealed that QN town's households adopt

proactive strategies during floods, such as stockpiling food and promptly evacuating vulnerable individuals' elderly, sick, and children to safe areas upon receiving government warnings. Furthermore, sanitary facilities have been installed on the upper floors, demonstrating a high level of accessibility to essential resources, particularly clean water, during flood events. In contrast, households in DN commune face challenges in accessing these resources due to an inadequate drainage system that fails to account for the highest levels of flood risk. Consequently, water is not drained promptly, which exacerbates the situation and hampers rescue and support operations during floods. Beyond the lack of preparedness, households in DN commune endure frequent risks and substantial damage from flooding and inundation, unlike their counterparts in QN town. It is evident in urban areas, characterized by extensive concrete paving, effective floodwater management depends on well-maintained drainage systems, operational pumps, and the availability of water retention areas crucial elements for efficient urban floodwater management [47].

The study findings provide crucial insights for the planning and development policies of both areas, especially DN commune, by identifying following measures to enhance the adaptive capacity of households to natural disasters, thereby reducing vulnerability and curtailing losses, including: (i) Developing flood risk maps, identifying vulnerable regions, and implementing supportive measures such as assisting in the relocation of residents from high-risk zones, enhancing housing as necessary, and assisting low-income households living in temporary houses; (ii) Improving community awareness and practices on climate change and disaster response; (iii) Enhancing support effectiveness via social organizations and training courses on climate change and disaster response; and (iv) Developing concrete provincial urban planning and disaster prevention action plan, that considers varying levels of disaster risks to enhance the efficiency and quality of provincial infrastructures, with particular attention on the drainage system. In addition, DN commune should contemplate aiding local residents in constructing well-designed houses that are adapted for flood resilience and preparedness for historical inundation events.

5. Conclusions

Households in QN town, Quang Nam province, demonstrated relatively high adaptive capacity to natural disasters with a score of 0.61 (on a 0–1 scale), while households in DN commune, Da Nang city, exhibited lower adaptive capacity with a score of 0.55. It is recommended that the adaptive capacity of households located in both areas should be enhanced by implementing strategies, planning, and supportive measures, improving community awareness and practices, and enhancing support effectiveness. Subjectivity in indicator selection, number of indicators, and number of households interviewed were limitations of this research. The survey conducted 3 months after the historical inundation affecting the study areas may underestimate adaptive capacity to normal disaster events. Further studies should be conducted to understand key indicators and key drivers of households' adaptive capacity to disasters.

Author contribution statement: Conceptualization, N.T.L., N.T.H.H.; Investigation, N.T.L., T.T.H., N.T.H.H., N.T.D.; Methodology, N.T.L., N.T.H.H.; Data analysis, N.T.L., T.T.H., N.T.H.H.; Writing-original draft preparation, N.T.L.; Review and editing, N.T.H.H., Y.I.I., N.T.D., N.T.H., Y.U. All authors have read and agreed to the published version of the manuscript.

Acknowledgements: We would like to express our gratitude to the officers and households in the study areas for their valuable support. We also acknowledge the valuable guidance and advice provided by Prof. Dr. Mai Trong Nhuan. Sincere thanks are extended to the students of the Master's Program in Climate Change and Development batch 6 for their cooperation and assistance in facilitating the research. This research is supported by Vietnam Japan University under the VJU.CS.23.01 project.

Competing interest statement: The authors declare no conflict of interest.

References

1. Natural Hazards. National risk index. (Ed.). Available online: https://hazards.fema.gov/nri/natural-hazards.
2. Solecki, W.; Leichenko, R.; O'Brien, K. Climate change adaptation strategies and disaster risk reduction in cities: connections, contentions, and synergies. *Curr. Opin. Env. Sust.* **2011**, *3(*3), 135–141. https://doi.org/10.1016/j.cosust.2011.03.001.
3. Pham, N.T.T.; Nong, D.; Sathyan, A.R.; Garschagen, M. Vulnerability assessment of households to flash floods and landslides in the poor upland regions of Vietnam. *Clim. Risk Manag.* **2010**, 28, 100215. https://doi.org/10.1016/j.crm.2020.100215.
4. Birkmann, J.; Garschagen, M.; Kraas, F.; Quang, N.M. Adaptive urban governance: new challenges for the second generation of urban adaptation strategies to climate change. *Sustain. Sci.* **2010**, *5*(2), 185–206. https://doi.org/10.1007/s11625-010-0111-3.
5. Mesfin, D.; Simane, B.; Belay, A.; Recha, J.; Schmiedel, U. Assessing the adaptive capacity of households to climate change in the central rift valley of Ethiopia. *Climate* **2020**, *8*(10), 106. https://doi.org/10.3390/cli8100106.
6. Vallury, S.; Smith, A.P.; Chaffin, B.C.; Nesbitt, H.K.; Lohani, S.; Gulab, S.; Banerjee, S.; Floyd, T.M.; Metcalf, A.L.; Metcalf, E.C.; Twidwell, D.; Uden, D.R.; Williamson, M.A., Allen, C.R. Adaptive capacity beyond the household: a systematic review of empirical social-ecological research. *Environ. Res. Lett*. **2022**, *17(6)*, 063001. https://doi.org/10.1088/1748-9326/ac68fb.
7. Bossio, C.F.; Ford, J.D.; Labbé, D. Adaptive capacity in urban areas of developing countries. *Clim. Change.* **2019**, *157*(2), 279–297. https://doi.org/10.1007/s10584-019-02534-2.
8. Cinner, J.E.; Adger, W.N.; Allison, E.H.; Barnes, M.L.; Brown, K.; Cohen, P.J.; Morrison, T.H. Building adaptive capacity to climate change in tropical coastal communities. *Nat. Clim. Change* **2018**, *8*(2), 117–123.
9. Nguyen, K.A.; Liou, Y.A.; Terry, J.P. Vulnerability of Vietnam to typhoons: A spatial assessment based on hazards, exposure and adaptive capacity. *Sci. Total Environ.* **2019**, *682*, 31–46.
10. van Aalst, M. A.; Koomen, E.; de Groot, H. L. F. Vulnerability and resilience to drought and saltwater intrusion of rice farming households in the Mekong Delta, Vietnam. *Econ. Disaster Clim. Change*. **2023**, *7*, 407–430.
11. Mai, T.N.; N, T.T.; Nguyen, T.H.H.; Tran, D.Q. An indicator-based approach to quantifying the adaptive capacity of urban households: The case of Da Nang city, Central Vietnam. *Urban Clim.* **2016**, *15*, 60–69.
12. Elrick-Barr, C.E.; Preston, B.L.; Thomsen, D.C.; Smith, T.F. Toward a new conceptualization of household adaptive capacity to climate change: applying a risk governance lens. *Ecol. Soc.* **2014**, *19(4)*, 12. http://www.jstor.org/stable/26269698.
13. Asian Development Outlook 2019. Asian Development Outlook, 2019. https://doi.org/10.22617/fls190070-3.
14. Huong, T.T.L.; Van Anh, D.T.; Dat, T.T.; Truong, D.D.; Tam, D.D. Disaster risk management system in Vietnam: progress and challenges. *Heliyon* **2022**, *8*(10), e10701. https://doi.org/10.1016/j.heliyon.2022.e10701.
15. Kerblat, Y.; Nguyen, D.H., Chinh, N.C.; Wilderspin, I.F.; Baca, A.C.; Hanumappa, M.; Chia, B.M.; Srivastava, J.P. Toward integrated disaster risk management in Vietnam: recommendations based on the drought and saltwater intrusion crisis and the case for investing in longer-term resilience, The World Bank, 1818 H Street NW, Washington DC 20433, USA, 2017, pp. 23.
16. Kamei, M.; Nguyen, A.T.; Guibrunet, L.; Davide, M.; Fennell, P.; Jones, P.; Hoang

Son, L.; Rivero-Villar, A.; Boenigk, L.; Josset, L.; Hamel, P.; Davies, K.; Mac, T.H.T.; Dang, N.M.; Viet, D.B. Da Nang City Climate Action Plan - A conceptual framework for sectoral climate actions. IGES, 2023.

17. Mai, T.N.; Nguyen, T.H.H.; Nguyen, T.T.; Tran, M.L. Assessing the adaptive capacity of coastal urban households to climate change (Case study in Liên Chiểu district, Đà Nẵng city, Vietnam). *VNU J. Sci.: Earth Environ. Sci*. **2015**, *31(2)*, 23–35.
18. Ward People's Committee. Summarizing natural disaster prevention, search, and rescue work in 2022 and implementing plans for 2023. Available online: https://hoakhanhnam.danang.gov.vn/view.aspx?ID=227 (Accessed on 25 December 2023).
19. Le, A.D.; Vu, L.T.T. Climate change's impact on natural hazards in Quang Nam province, Mid-Central Vietnam. In: Bruun, O., Casse, T. (eds) On the Frontiers of Climate and Environmental Change. *Environ. Sci. Eng.* **2013**, pp. 91–98. https://doi.org/10.1007/978-3-642-35804-3_5.
20. Ministry of Natural Resources and Environment. Climate change scenario. Viet Nam Publishing House of Nature Resources, Environment and Cartography, 2021. Available online: http://www.imh.ac.vn/files/doc/2020/KB%20BDKH%202912.pdf.
21. Statistical Yearbook of Lien Chieu district. Statistical publishing house Statistics Department of Thanh Khe - Lien Chieu. Da Nang City Statistics Department, 2022.
22. Tran, T.A.; Saizen, I.; Tsutsumida, N.; Venkatesh, R.; Le, N.H.; Nguyen, V.A.; Nguyen, V.L.; Ngo, T.T.; Truong, P.M. Flood vulnerability assessment at the local scale using remote sensing and GIS techniques: A case study in Da Nang City, Vietnam. *J. Water Clim. Change* **2022**, *13(9)*, 3217.
23. Nguyen, T.D.M.; Do, T.N.; Nghiem, V.S.; Jiwnath, G.; Dang, B.K.; Giang, V.T.; Vu, K.C.; Pham, V.M. Flood inundation assessment of UNESCO World Heritage Sites using remote sensing and spatial metrics in Hoi An city, Vietnam. *Ecol. Inf.* **2024**, *79*, 102427. https://doi.org/10.1016/j.ecoinf.2023.102427.
24. Nguyen, T.L.; Asahi, C.; Tran, T.A.; Le, N.H. Indicator-based approach for flood vulnerability assessment in ancient heritage city of Hoi An, Central Region of Vietnam. *Nat. Hazards* **2022**, *114(2)*, 2357–2385.
25. Intergovernmental Panel on Climate Change (IPCC). Climate Change 2014 – Impacts, Adaptation and Vulnerability: Part B: Regional Aspects: Working Group II Contribution to the IPCC Fifth Assessment Report. Cambridge University Press, 2014.
26. Ford, J.D.; Keskitalo, E.C.H.; Smith, T.; Pearce, T.; Berrang-Ford, L.; Duerden, F.; Smit, B. Case study and analogue methodologies in climate change vulnerability research. *Wiley Interdiscip. Rev. Clim. Change* **2010**, *1(3)*, 374–392.
27. Engle, N.L.; Lemos, M.C. Unpacking governance: Building adaptive capacity to climate change of river basins in Brazil. *Global Environ. Change* **2010**, *20*, 4–13.
28. Hahn, M.B.; Riederer, A.M.; Foster, S.O. The livelihood vulnerability index: A pragmatic approach to assessing risks from climate variability and change–A case study in Mozambique. *Global Environ. Change* **2009**, *19*, 74–88.
29. Brooks, N.; Adger, W.N. Assessing and enhancing adaptive capacity. *Adapt. Policy Frameworks Clim. Change: Dev. Strategies Policies Meas.* 2005, 165–181.
30. Ramieri, E.; Hartley, A.; Barbanti, A.; Santos, F.D.; Gomes, A.; Hilden, M.; Santini, M. Methods for assessing coastal vulnerability to climate change. *ETC CCA Technical Paper* **2011**, *1(2011)*, 1–93.
31. Maldonado-Méndez, M.d.L.; Romo-Lozano, J.L.; Monterroso-Rivas, A.I. Determinant indicators for assessing the adaptive capacity of agricultural producers

to climate change. *Atmosphere* **2022**, *13(7)*, 1114. https://doi.org/10.3390/atmos13071114.

32. OECD. Handbook on Constructing Composite Indicators and User Guide, 2008. https://www.oecd-ilibrary.org/economics/handbook-on-constructing-composite-indicators-methodology-and-user-guide_9789264043466-en (accessed on 15 March 2023).
33. Han, J.; Kamber, M.; Pei, J. Data mining concepts and techniques third edition. University of Illinois at Urbana-Champaign Micheline Kamber Jian Pei Simon Fraser University, 2012.
34. Nguyen, T.H.H.; Nguyen, D.L.; Nguyen, T.A.H. Sustainability of traditional vermicelli production in Minh Hong village, Ba Vi district, Hanoi, Vietnam. *IOP Conf. Ser.: Earth Environ. Sci.* **2019**, *266(1)*, 012015.
35. Adger, W.N. Social vulnerability to climate change and extremes in coastal Vietnam. *World Dev.* **1999**, *27*(2), 249–269.
36. Fothergill, A.; Peek, L. A. Poverty and disasters in the United States: A review of recent sociological findings. *Nat. Hazards* **2004**, *32*, 89–110.
37. Norton, J.; Chantry, G. Vaccinate your home against the storm-reducing vulnerability in Vietnam. *Open House Int.* **2008**, *33*(2), 26–31.
38. Tuan, T.H.; Tran, P.; Hawley, K.; Khan, F.; Moench, M. Quantitative cost-benefit analysis for typhoon resilient housing in Danang city, Vietnam. *Urban Clim.* **2015**, *12*, 85–103.
39. Kunreuther, H.; Meyer, R.J.; Michel-Kerjan, E. Strategies for better protection against catastrophic risks. Risk Management and Decision Processes Center, The Wharton School of the University of Pennsylvania, 2007.
40. Nasreen, M.; Hossain, K.M.; Khan, M.M. Coastal disaster risk management in Bangladesh. *Routledge eBooks* 2023, pp. 540. https://doi.org/10.4324/9781003253495.
41. Muttarak, R.; Pothisiri, W. The role of education on disaster preparedness: case study of 2012 Indian ocean earthquakes on Thailand's Andaman coast. *Ecol. Soc.* **2013**, *18(4)*, 51. https://doi.org/10.5751/es-06101-180451.
42. Atreya, A.; Czajkowski, J.; Botzen, W.; Bustamante, G.; Campbell, K.; Collier, B.; Ianni, F.; Kunreuther, H.; Michel-Kerjan, E.; Montgomery, M. Adoption of flood preparedness actions: A household level study in rural communities in Tabasco, Mexico. *Int. J. Disaster Risk Reduct.* **2017**, *24*, 428–438.
43. Pelling, M.; High, C. Understanding adaptation: What can social capital offer assessments of adaptive capacity? *Global Environ. Change* **2005**, *15*(4), 308–319. https://doi.org/10.1016/j.gloenvcha.2005.02.001.
44. Thathsarani, U.; Gunaratne, L. H. P. Constructing and index to measure the adaptive capacity to climate change in Sri Lanka. *Procedia Eng.* **2018**, *212*, 278–285. https://doi.org/10.1016/j.proeng.2018.01.036.
45. Füssel, H. Adaptation planning for climate change: concepts, assessment approaches, and key lessons. *Sustain. Sci.* **2007**, *2*(2), 265–275.
46. López-Marrero, T.; Yarnal, B. Putting adaptive capacity into the context of people's lives: a case study of two flood-prone communities in Puerto Rico. *Nat. Hazards* **2009**, *52*(2), 277–297. https://doi.org/10.1007/s11069-009-9370-7.
47. Chu, A.; Lin, Y.; Chiueh, P. Incorporating the effect of urbanization in measuring climate adaptive capacity. *Land Use Policy* **2017**, *68*, 28–38. https://doi.org/10.1016/j.landusepol.2017.07.019.

JOURNAL OF HYDRO-METEOROLOGY

Rerearch Article

Exploiting the results of running the GEOS-CF model to evaluate $PM_{2.5}$ concentration in near real-time in Vietnam

Uyen Khanh Le[1], Binh Quoc Pham[2], Long Ta Bui[1]*

[1] Faculty of Environment and Natural Resources, University of Technology, Vietnam National University, Ho Chi Minh City; uyen.le02@hcmut.edu.vn; longbt62@hcmut.edu.vn

[2] Envim Lab, University of Technology, Vietnam National University, Ho Chi Minh City; phamquocbinh2018@gmail.com

*Correspondence: longbt62@hcmut.edu.vn; Tel.: +84–918017376

Received: 12 March 2024; Accepted: 01 May 2024; Published: 25 June 2024

Abstract: Near real-time information about global atmospheric composition, including $PM_{2.5}$ fine dust, is valuable because it helps forecast air quality and manage environmental disasters. Recently, NASA's Global Modeling and Assimilation Office has released a set of near real-time Goddard Earth Observing System models that help analyze and forecast global air quality, named GEOS-CF (GEOS Composition Forecast). In particular, GEOS-CF can simulate the transport from the stratosphere to the troposphere (the stratosphere to troposphere transport) which is technically very difficult. In Vietnam's challenging conditions, research and application of GEOS-CF output results must be made. In this study, the authors developed a tool named ENAR (Envim Nasa Analysis Result) to help interpret GEOS-CF results provided free of charge by NASA to form $PM_{2.5}$ pollution maps for each area hourly across the entire territory of Vietnam. ENAR was applied to build pollution maps for the first three months 2024. The results were analyzed to clarify the range of pollution levels for each area, including the Hoang Sa and Truong Sa archipelagos, Vietnam. These results allow scientific agencies to obtain reliable information for studies predicting this type of pollution.

Keywords: $PM_{2.5}$; GEOS-CF; ENAR tool; NASA; Vietnam.

1. Introduction

Air quality forecasts have recently become increasingly important for Vietnam. Over the past years, rapid economic growth in cities in Vietnam, such as Ho Chi Minh City and Hanoi, has significantly increased the amount of man-made emissions, affecting people's health [1–4]. Among pollutants, fine particulate matter (PM) $PM_{2.5}$ is a significant public health concern [5–7]. Adverse health effects have been associated with short- and long-term exposure to $PM_{2.5}$ [8]. $PM_{2.5}$ is associated with morbidity, mortality, [9] cardiovascular disease, respiratory disease, myocardial infarction, increased hospitalization rates [10] and other diseases [11]. Accurate exposure assessment of $PM_{2.5}$ is a prerequisite for investigating its adverse health effects. Initial studies estimated $PM_{2.5}$ at the nearest monitoring station [12]. However, the closest monitoring devices cannot capture all variations in $PM_{2.5}$ concentrations, and non-differential misclassification occurs [13].

It is essential to predict the scope and level of impact of this type of pollution to protect human health. In recent years, several studies have been conducted on some large urban areas of the country, including the city. Ho Chi Minh city, using models that take into account

chemical reactions and regional scales [14–16]. In the study [17], $PM_{2.5}$ pollution forecasts for Southeast Asia, including Cambodia, Laos, Thailand and Vietnam, were made by comparing emission database scenarios for two years, 2019 and 2050. An overview of the research shows that existing studies have not yet produced $PM_{2.5}$ distribution maps for Vietnam at any level. To assess the damage caused by this type of pollution, it is necessary to build a distribution map of this type of pollution [2], which is also why this study was conducted.

In recent times, air pollution modelling research agencies such as universities space research association, goddard earth sciences technology and research, NASA's global modeling and assimilation office, goddard space flight center, TOLNet - tropospheric ozone lidar network ground-based profiling of tropospheric ozone has launched many scientific products, especially the NASA goddard earth observing system composition forecast (GEOS-CF). This product provides users free of charge with 5-day near real-time calculation results of air pollutants, including fine particulate matter ($PM_{2.5}$) [18]. This model combines the GEOS weather analysis and forecasting system with the state-of-the-art GEOS-Chem chemistry module [19, 20]. The complete model and simulation features for the troposphere are given in [21] and provided in [22] for the stratosphere. These models have been calibrated and validated against satellite, balloon, lidar observations of stratospheric composition, including ozone (O_3) measurements and related essential nitrogen and chlorine species related to O_3 recovery in the stratosphere [22]. These products support NASA field missions and evaluate the impact of NASA observations on environmental prediction [22].

In conditions where there are still many difficulties in investment funding, exploiting these results is necessary because they are provided for free, and these results allow research agencies and organizations to access them. latest to quantify the damage caused by pollution and provide long-term plans to reduce pollution. This study aims to exploit the results from running the GEOS-CF model to build $PM_{2.5}$ pollution maps across the entire territory of Vietnam. On that basis, initial assessments are made about the level and scope of impact on different areas of the country.

2. Materials and Methods

2.1. GEOS-CF model

In 2019, NASA's global modeling and assimilation office released a suite of near real-time goddard earth observing system models (GEOS) for analysis and forecasts with delays from one month to two months. This product realizes NASA's field mission, helping the agency predict the global environment. This product is widely available to many users. Version 1.0 was released in September 2019, followed by version 1.1 in March 2020, version 1.2 in February 2022 and version 1.3 in December 2022 [18]. The GEOS-CF system uses the GEOS-Chem chemical scheme version 12.0.1 (http://geos chem.org) [19]. GEOS-Chem includes detailed stratospheric chemistry fully coupled with tropospheric chemistry described in [23]. GEOS-Chem calculated the photolysis rate online using the Fast-JX code [24] implemented in GEOS-Chem [25]. The gas phase mechanism includes 250 chemicals and 725 reactions and is solved using the KPP Rosenbrock Kinetic Preprocessor solver [26].

GEOS-CF uses two independent aerosol schemes run in parallel. The first scheme is the goddard chemistry, transport, aerosol, radiation [27, 28]. The second diagram - mechanism GEOS-Chem aerosol, simulates the mass concentrations of significant aerosol components - dust, black carbon , organic carbon, sea salt, sulfate, nitrate and ammonium and provides up-to-date information on secondary organic aerosol (SOA) chemistry [28].

GEOS-CF uses emissions data from NASA-Harvard, HEMCO [20]. Anthropogenic emissions are monthly averages from HTAP v2.2 [29] and RETRO [30], broken down into hourly values using weekday and day-specific scale factors by industry [31]. Calculations in

GEOS-CF are performed on a cubed-sphere c360 grid [32] (resolution 25 km × 25 km) with 72 vertical layers with pressure values. At the highest level, the pressure is 0.01 hPa. Input data files are provided at ¼ degree horizontal resolution. This global grid has 1440 longitudinal and 721 latitudinal points, corresponding to a resolution of 0.25° × 0.25°. Model output with 1-hour time resolution. The output result is at the altitude closest to the ground at level 72, corresponding to an altitude with a pressure of 985 hPa, equivalent to about 1.2 km [18]. This distance is located in the troposphere, so it directly affects the concentration of $PM_{2.5}$ near the ground and is also the subject of environmental research.

The GEOS-CF model is calibrated, verified, validated by data from NASA, including Satellite, including ACE-FTS v4.1, MLS v5, SAGE III/ISS v5.1, Ozone Watch, OMI "TOMS-like" v3 level 3 products, SBUV Merged Ozone product v8.6; Balloon, including Ozonesondes; Ground-based, including TOLNet Lidar [1].

2.2. Methods and implementation steps

To achieve the set goals, this study uses ENAR software (Envim Nasa Analysis Result), developed by the authors using Python programming, which includes 11 steps. Step 1: perform downloading files, download Netcdf files from the website: https://portal.nccs.nasa.gov/datashare/gmao/geos-cf/v1/ana/Y{year}/M{month}/D{day}. Step 2, the step to search for 24 netCDF files (corresponding to 24 hours) has the following form:GEOS-CF.v01.rpl.htf_inst_15mn_g1440x721_x1.{year}{month}{day}{hour}00.nc4 is performed. After downloading 31×24=744 netCDF files corresponding to 31 days, 24 hours per day, the conversion step from netCDF file (.nc) → geoTIFF file (.tif) is performed (using tools in arcpy to process physical). Step 3: convert the map from this (.tif) format to a point shapefile (Extracting Tif → Points). Step 4: performs interpolation with the IDW Interpolation method, which helps smooth the map. Step 5: cut and merge this Tiff file with the Vietnam map. After the Extracting Map step (the result is that the Tif files have been interpolated and interpolated with the Vietnam map), they are converted into a .png file. Step 6 performs a colour change to identify the level of pollution.

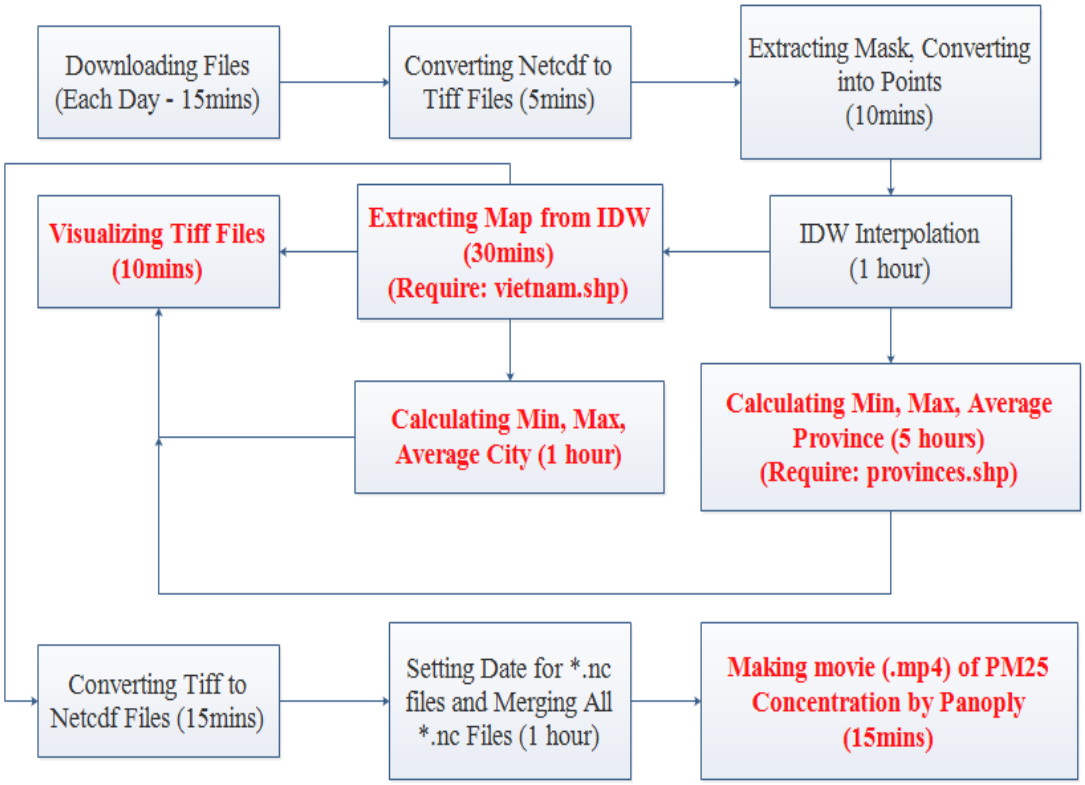

Figure 1. Method and processing steps.

Step 7 calculates the pollution level of the entire Vietnam with three quantities: minimum value, maximum value, and average value (Min, Max, Average); the results are exported as Excel files. Step 8 exports the necessary quantities for each province/city and islands (Con Dao, Truong Sa Islands, Hoang Sa Islands). After cutting and collaging, we will continue to change the colour to make it easier to see their pollution level (visualize GEOTiff File) (Step 9). Finally, to see the level of $PM_{2.5}$ pollution in Vietnam through each day of that month, we will take the .tif files from step 5 to convert them to NetCDF (.nc) files (Step 10) and use the tool cdo tool to set the minute, hour, day, month, year for each .nc file. All are merged into January.nc file. The book also uses the tool from Panoply (require: Java 11) to convert .nc files into a movie file (.mp4) of hourly $PM_{2.5}$ pollution values (Step 11) (Figure 1).

3. Results and discussion

3.1. Pollution distribution in January 2024

The average daily $PM_{2.5}$ concentration in January 2024 has a complex spatiotemporal distribution, but it is clear that the highest pollution concentration occurs in the North. From January 1 to January 2, the concentration decreased slightly, then increased sharply until January 5 and gradually decreased until January 7, then continued to increase and decrease unevenly until the peak on January 1 to January 30. The highest concentration reached 390.12 µg/m^3, and the lowest reached 4.16 µg/m^3. In most provinces in the Red River Delta, it is very high. In the two archipelagos of Hoang Sa and Truong Sa Islands, $PM_{2.5}$ pollution concentration is always at the allowable threshold ranging from 3.94-51.24 µg/m^3. Figure 2 shows the average daily $PM_{2.5}$ concentration variation in January 2024. Figure 3 shows the average daily distribution map of $PM_{2.5}$. Analysis results show that Hanoi and neighbouring provinces such as Bac Ninh, Vinh Phuc, and Phu Tho are most affected by pollution. On 4-5 January 2024, from Quang Binh to the Northern provinces, $PM_{2.5}$ concentrations reached high values. By 6 January 2024, the North and parts of the Southern provinces, such as Long An, An, Giang, Dong Thap, and Kien Giang, also had high concentrations. From 15-19 January 2024, Hanoi, surrounding provinces, Yen Bai, and Hoa Binh,... are greatly affected. On 23 January 2024, the entire North stretching to Quang Ngai and part of the Central Highlands and Southeast regions had high concentrations. From 24-31 January 2024, the scope of influence stretches across the entire northern region to Quang Ngai.

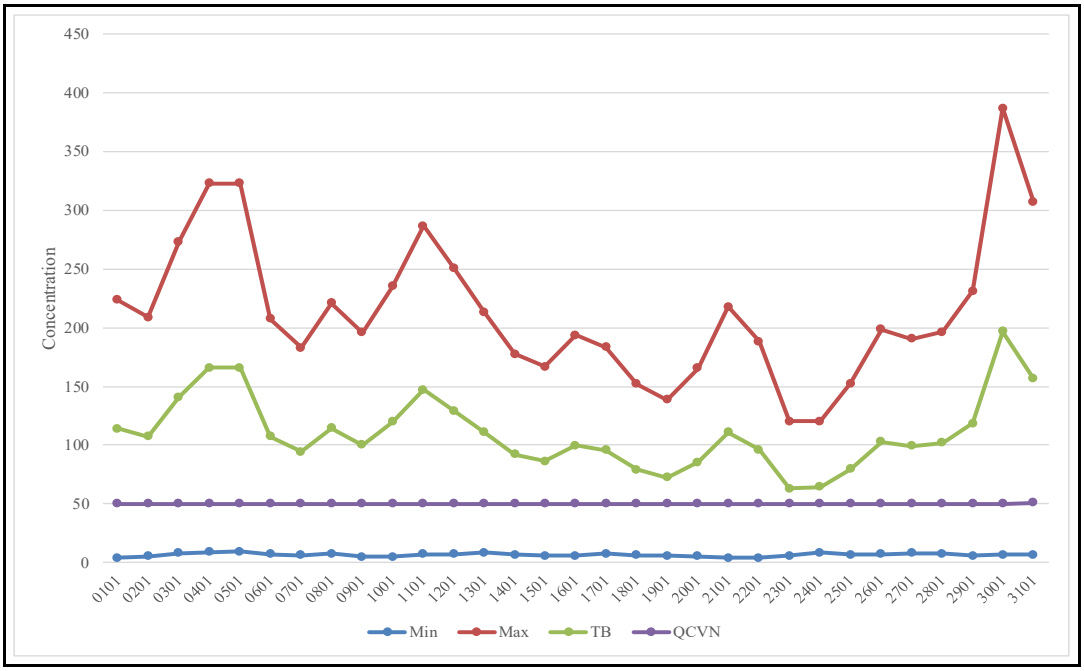

Figure 2. Average daily $PM_{2.5}$ (µg/m^3) concentration in January 2024.

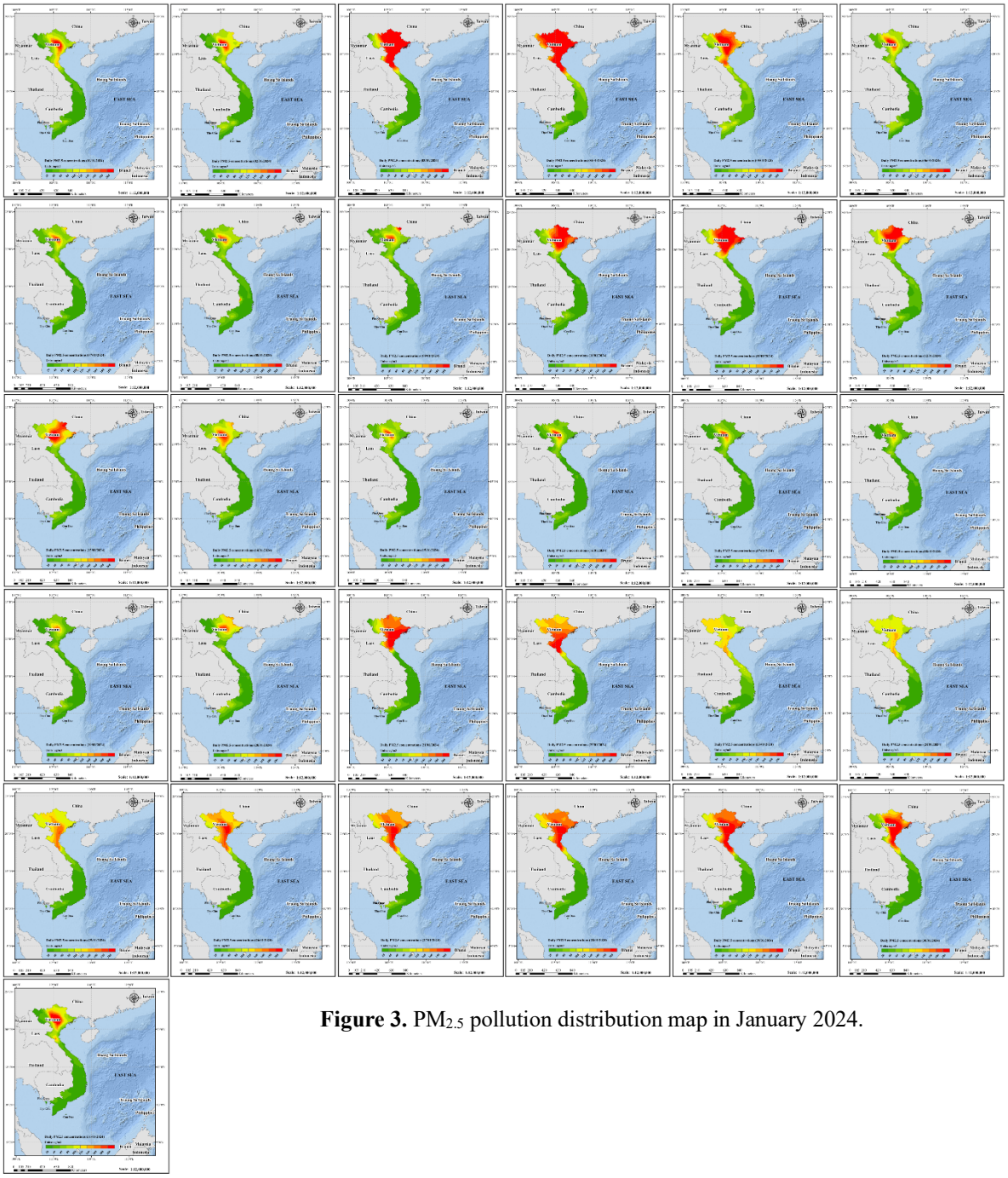

Figure 3. $PM_{2.5}$ pollution distribution map in January 2024.

3.2. Pollution distribution in February 2024

The average daily $PM_{2.5}$ concentration in February 2024 has a complex spatiotemporal distribution, and high pollution levels always occur in the country's North. From 1 February to 5 February, the concentration gradually decreased, then increased sharply until February 8 and progressively decreased unevenly over the days, after which the concentration increased or decreased steadily. With average monthly concentrations ranging from 5.02-151.75 µg/m^3. Figure 4 below shows the average $PM_{2.5}$ concentration variation of days in February 2024. The $PM_{2.5}$ concentration distribution map for each day is shown in Figure 5.

Hanoi capital and surrounding provinces still have alarming pollution levels (Figure 5). In the first three days of February 2024, most of the Red River Delta, the Northeast, part of the Northwest, and the provinces of Nghe An, Ha Tinh, and part of the South Central coastal region will be affected. of pollution. On 4 February 2024, provinces from Quang Nam to the North were affected by pollution. On 5-7 April 2024, the North Central region, Northeast,

Northwest and Red River Delta, and part of the South Central coastal provinces will be affected. From 9-12 February 2024, provinces from Binh Dinh to the North will be highly affected. From 12-29 February 2024, the area of influence from central provinces such as Quang Tri, Quang Nam, Quang Ngai, and Binh Dinh extended to the North. In February 2024, the high-impact area has little impact on the Central Highlands, Southeast, and South.

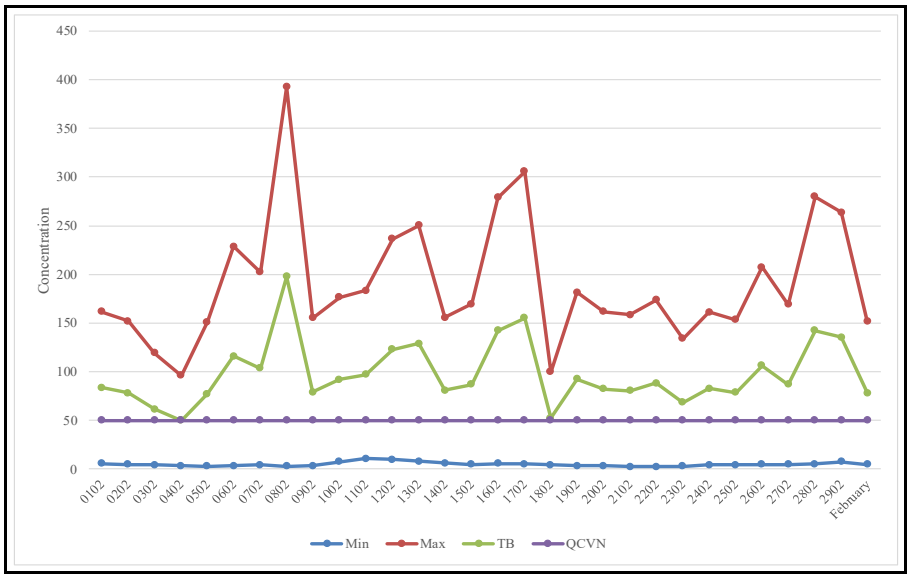

Figure 4. Average daily $PM_{2.5}$ (μg/m^3) concentration in February 2024.

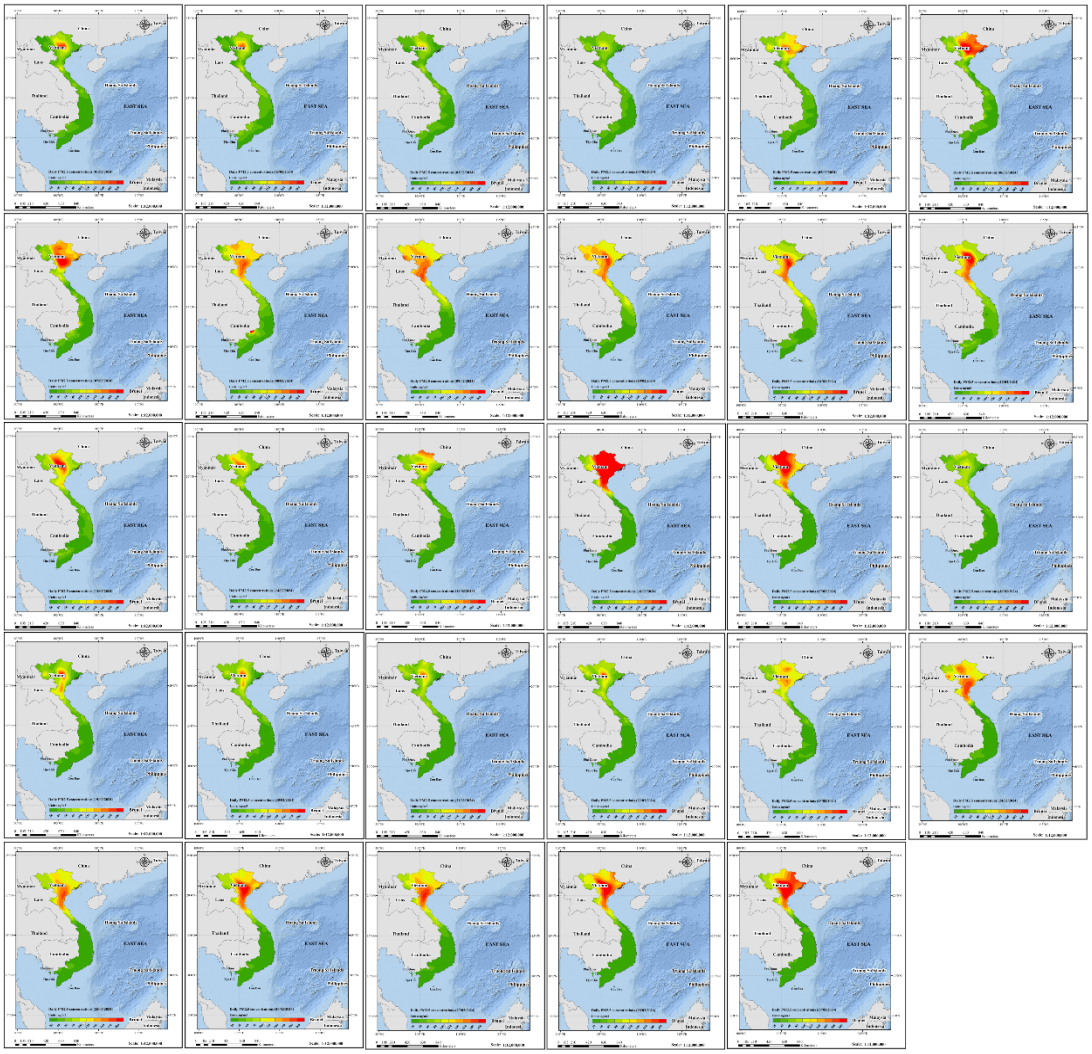

Figure 5. $PM_{2.5}$ pollution distribution map in February 2024.

3.3. Pollution distribution in March 2024

Like the previous two months, the average daily $PM_{2.5}$ concentration in March 2024 has a complex spatiotemporal distribution. The average concentration of this product ranges from 7.48-187.24 µg/m^3. Figure 6 shows the $PM_{2.5}$ pollution distribution map for the whole of Vietnam. Figure 7 shows the variation in average $PM_{2.5}$ concentration of days in March 2024. In the first two days of March 2024, the Red River Delta region, the Northeast, part of the Northwest and provinces such as Nghe An and Ha Tinh were severely affected by $PM_{2.5}$ pollution. On 3 March 2024, provinces from Quang Binh to the North, by 4 March 2024, most provinces from Binh Dinh to the North will be significantly affected. Especially on 5 March 2024, all of Vietnam will be affected. Hanoi, Hoa Binh, Yen Bai, and parts of the Northeast provinces, Phu Yen and Nghe An, are affected. From 9-12 March 2024, the area of influence will be from Nghe An-Ha Tinh, extending to the North. From 13-15 March, the area of influence covers the Mekong Delta, such as An Giang and Long An. In the remaining days of March, the northern region to Nghe An is most affected.

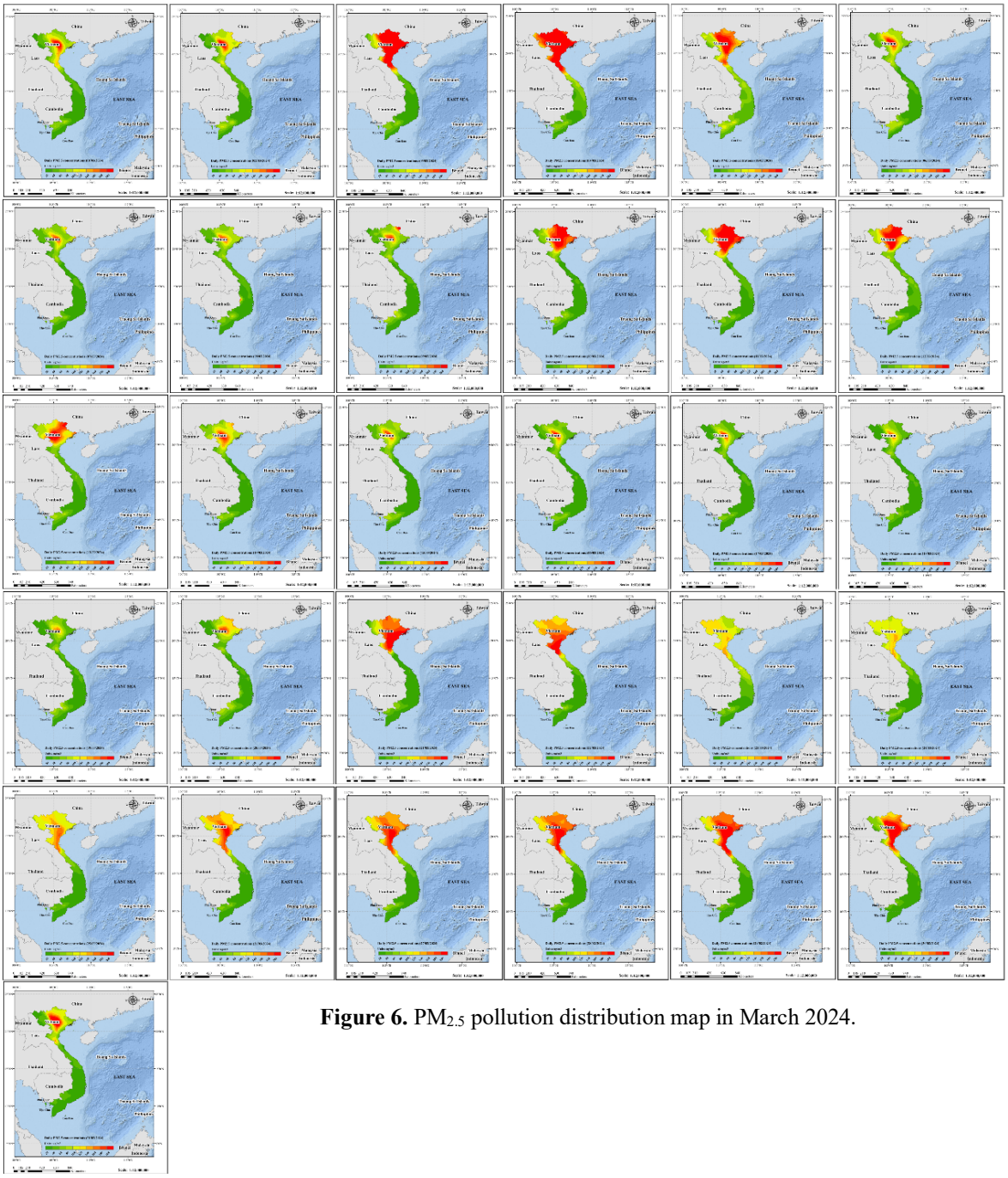

Figure 6. $PM_{2.5}$ pollution distribution map in March 2024.

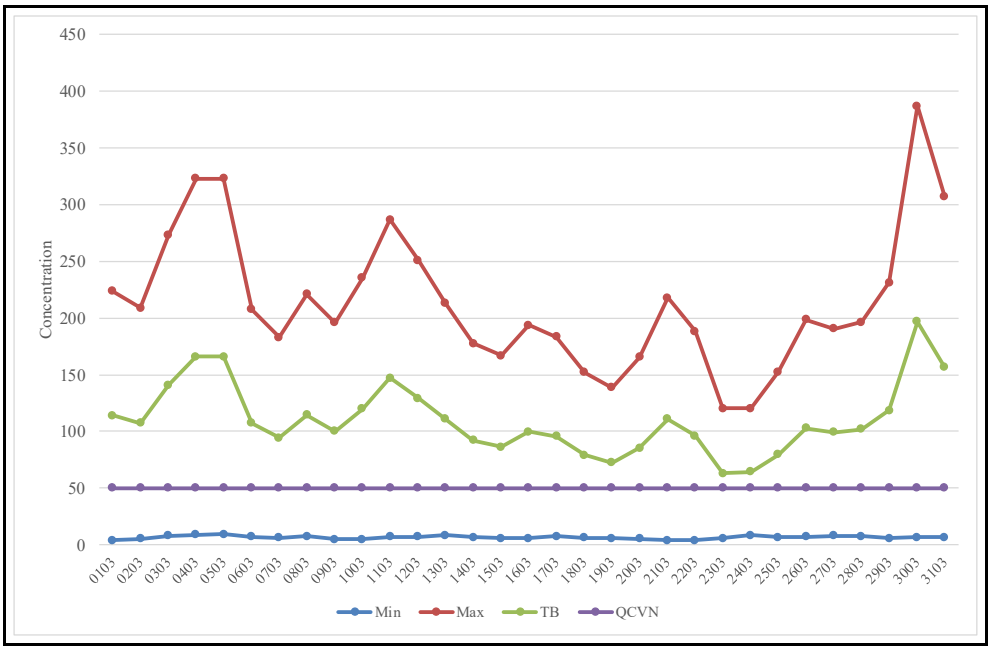

Figure 7. Average daily $PM_{2.5}$ (µg/m^3) concentration in March 2024.

3.4. Results of pollution distribution by region

ENAR software allows exporting tabular results of min/max concentrations and monthly averages for seven regions of the country, along with the country's two Islands of Hoang Sa and Truong Sa. The average results for January 2024 are shown in Table 1, Figure 8. It can be seen that the three Northern Delta regions, including Northwest, Northeast, and Red River Delta, all have much higher min and max concentrations compared to Vietnamese standard, followed by North Central, Southeast, Mekong Delta, and South Central Coast. The Central Highlands region, Hoang Sa, and Truong Sa Islands are still within allowed limits. Compared to January 2024, concentrations in February 2024 in areas improved (concentrations decreased significantly). In March 2024, the concentration increased compared to February, but it was generally smaller than January 2024.

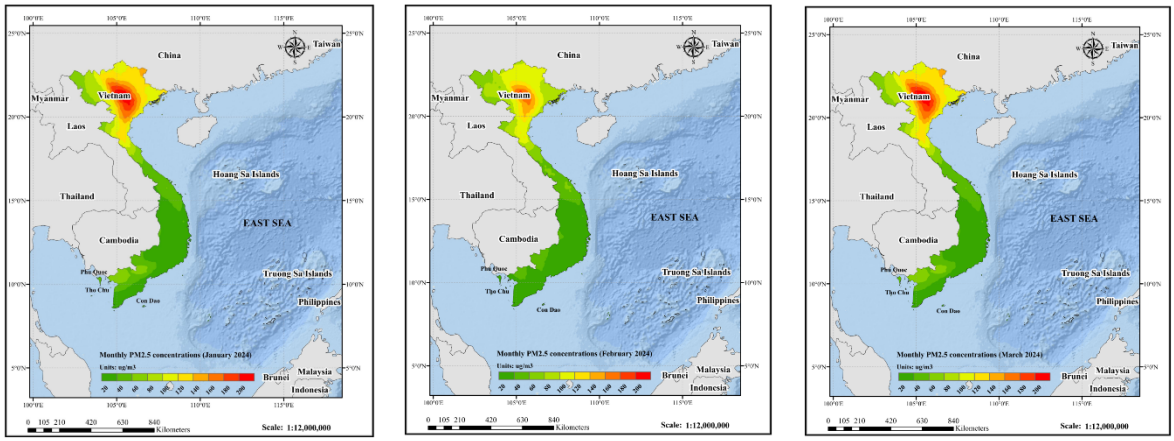

Figure 8. Average monthly $PM_{2.5}$ pollution distribution map from January to March 2024.

Table 1. Concentration by seven regions, Hoang Sa and Truong Sa Islands in January 2024.

Region	Concentration (µg/m^3)	
	Min	Max
Northwest	40.69	174.27
East Northern	87.37	187.29
Red river delta	72.56	186.07

Region	Concentration (μg/m^3)	
	Min	**Max**
Mekong Delta	8.79	54.83
South Central Coast	9.73	39.24
North Central	23.49	140.05
South East	9.42	56.01
Highlands	9.36	27.43
Hoang Sa	14.16	14.21
Truong sa	7.5	7.82

Table 2. Concentration by seven regions, Hoang Sa and Truong Sa Islands in February 2024.

Region	Concentration (μg/m^3)	
	Min	**Max**
Northwest	41.95	131.57
East Northern	65.72	149.25
Red river delta	63.94	151.78
Mekong Delta	6.2	29.22
South Central Coast	5.02	44.63
North Central	27.23	114.92
South East	6.5	36.05
Highlands	9.54	28.97
Hoang Sa	9.86	9.87
Truong sa	5.02	5.14

Table 3. Concentration by seven regions, Hoang Sa and Truong Sa Islands in March 2024.

Region	Concentration (μg/m^3)	
	Min	**Max**
Northwest	86.41	141.71
East Northern	65.51	160.29
Red river delta	60.90	164.68
Mekong Delta	6.56	26.25
South Central Coast	8.62	53.13
North Central	35.37	118.40
South East	7.15	25.73
Highlands	14.08	40.32
Hoang Sa	11.16	11.19
Truong sa	6.68	7.17

In the first three months of 2024, the Northeast region is always in the first position, with average monthly min/max concentrations ranging from 65.51-187.29 μm/m^3. This area has the highest exposure risk, often higher than allowed standards. Next is the Northwest region, with average monthly min/max concentrations ranging from 40.69-174.27 m/m^3 and very high exposure risk. On the territory of Vietnam, the Truong Sa and Hoang Sa islands have the lowest min/max level of 5.02-7.82 μm/m^3. Next is the Central Highlands region, which is still relatively "clean" with a min/max of 9.36-27.43 m/m^3 and the Mekong Delta, with a min/max of 6.2-54.83 μm/m^3. The Mekong Delta region still has times when it exceeds standards different from the Highlands, Hoang Sa, and Truong Sa Islands.

4. Conclusion

NASA's GEOS Composition Forecast System now provides near real-time estimates of the closest atmospheric composition. Five-day daily forecasts at high spatial resolution (0.25° latitude × 0.25° longitude up to the lower mesosphere) and high temporal frequency (hourly and 3-hourly) published entirely free of charge. For surface air quality, GEOS-CF simulates the stratosphere to troposphere transport. The results of running this model have been tested

based on NASA's satellite image processing and monitoring system, so they are reliable. This study focuses on exploiting $PM_{2.5}$ concentration results output from GEOS-CF software. However, to exploit these results for Vietnam, it is necessary to process the results output from GEOS-CF automatically. The research has successfully built an ENAR automation module using the Python language, integrating many packages such as Arcpy, Arcgis scripting, netCDF4, pandas,... and software such as ArcGIS Pro, OSGeo4W, Cygwin, and Panoply. This tool allows the processing of GEOS-CF run results and exporting charts and maps to analyze the distribution of $PM_{2.5}$ pollution throughout the country.

The results of GEOS-CF validated were analyzed using continuously updating by NASA as satellite images, Balloons, and TOLNet Lidar. However, that does not mean that this result is reliable in Vietnam, but the authors hope to find colleagues and state agencies to provide data to further improve the result of this research. The authors will also continue to conduct further research to apply GEOS-CF to Vietnam. The next research directions include finding the relationship between $PM_{2.5}$ pollution levels at an altitude corresponding to a pressure of 985 hPa and ground-level pollution levels. Next is $PM_{2.5}$ pollution prediction based on deep learning algorithms.

Author contribution statement: Developing research ideas, drawing up a draft writing plan, writing and editing the manuscript: L.T.B.; processing data, GIS: U.K.L.; processing data, software: B.Q.P.

Acknowledgements: The authors would like to express their sincere gratitude to Dr K. E. Knowland from the Universities Space Research Association (USRA)/GESTAR, Columbia, MD, USA, NASA Goddard Space Flight Center (GSFC) and Global Modeling and Assimilation Office (GMAO) for valuable discussions. This research was funded by the Viet Nam National University, Ho Chi Minh City (VNU-HCM), grant No: B2023-20-23. We acknowledge the support of time and facilities from Ho Chi Minh City University of Technology (HCMUT) and Vietnam National University Ho Chi Minh City (VNU-HCM) for this study.

Competing interest statement: The authors declare no conflict of interest.

References

1. Bui, L.T.; Nguyen, N.T.H.; Nguyen, P.H. Chronic and acute health effects of - $PM_{2.5}$ exposure and the basis of pollution control targets. *Environ. Sci. Pollut. Res*. **2023**, *30(33)*, 1–23. doi: 10.1007/s11356-023-27936-9.
2. Nguyen, T.H.; Nagashima, T.; Van Doan, Q. Air quality modelling study on the controlling factors of fine particulate matter ($PM_{2.5}$) in Hanoi: A case study in December 2010. *Atmosphere* **2020**, *11(7)*, 733. doi: 10.3390/atmos11070733.
3. Hieu, V.; Quynh, L.X.; Ho, P.N.; Hens, L. Health Risk Assessment of Mobility-Related Air Pollution in Ha Noi, Vietnam. *J. Environ. Prot.* **2013**, *04(10)*, 1165–1172. doi: 10.4236/jep.2013.410133.
4. Di, Q.; Kloog, I.; Koutrakis, P.; Lyapustin, A.; Wang, Y.; Schwartz, J. Assessing PM2.5 Exposures with High Spatiotemporal Resolution across the Continental United States. *Environ. Sci. Technol.* **2016**, *50(9)*, 4712–4721. doi: 10.1021/acs.est.5b06121.
5. Lim, S.S.; et al. A comparative risk assessment of burden of disease and injury attributable to 67 risk factors and risk factor clusters in 21 regions, 1990-2010: A systematic analysis for the Global Burden of Disease Study 2010. *Lancet* **2012**, *380*, 2224–2260. doi: 10.1016/S0140-6736(12)61766-8.
6. Slama, R.; et al. Traffic-related atmospheric pollutants levels during pregnancy and offspring's term birth weight: A study relying on a land-use regression exposure model. *Environ. Health Perspect.* **2007**, *115(9)*, 1283–1292. doi: 10.1289/ehp.10047.

7. Halonen, J.I.; Lanki, T.; Yli-Tuomi, T.; Kulmala, M.; Tiittanen, P.; Pekkanen, J. Urban air pollution, and asthma and COPD hospital emergency room visits. *Thorax* **2008**, *63(7)*, 635–641. doi: 10.1136/thx.2007.091371.
8. Jia Y.; et al. Effect of Air Pollution on Heart Failure: Systematic Review and Meta-Analysis. *Environ. Health Perspect*. **2023**, *131(7)*, 76001. doi: 10.1289/EHP11506.
9. Dominici, F.; et al. Fine particulate air pollution and hospital admission for cardiovascular and respiratory diseases. *Jama* **2006**, *295(10)*, 1127–1134. doi: 10.1001/jama.295.10.1127.
10. Peng, R.D.; et al. Emergency admissions for cardiovascular and respiratory diseases and the chemical composition of fine particle air pollution. *Environ. Health Perspect.* **2009**, *117(6)*, 957–963. doi: 10.1289/ehp.0800185.
11. Laden, F.; Schwartz, J.; Speizer, F.E.; Dockery, D.W. Reduction in fine particulate air pollution and mortality: Extended follow-up of the Harvard six cities study. *Am. J. Respir. Crit. Care Med*. **2006**, *173(6)*, 667–672. doi: 10.1164/rccm.200503-443OC.
12. Pinto, J.P.; Lefohn, A.S.; Shadwick, D.S. Spatial variability of $PM_{2.5}$ in urban areas in the United States. *J. Air Waste Manag. Assoc.* **2004**, *54(4)*, 440–449. doi: 10.1080/10473289.2004.10470919.
13. Ho, B.Q.; Clappier, A.; François, G. Air pollution forecast for Ho Chi Minh City, Vietnam in 2015 and 2020. *Air Qual. Atmos. Heal.* **2011**, *4(2)*, 145–158. doi: 10.1007/s11869-010-0087-2.
14. Bui, L.T.; Nguyen, P.H.; My Nguyen, D.C. Linking air quality, health, and economic effect models for use in air pollution epidemiology studies with uncertain factors. *Atmos. Pollut. Res.* **2021**, *12(9)*, 101118. doi: 10.1016/j.apr.2021.101118.
15. Le, T.N.; Nguyen, C.M.D.; Nguyen, H.P.; Bui, T.L. Assessment of public health impacts associated with short-term $PM_{2.5}$ pollution exposure: A case study in Binh Duong province, Vietnam. *VN J. Hydrometeorol*. **2023**, *746*, 70–87. doi: 10.36335/vnjhm.2023(746).70-87.
16. Nguyen, G.T.H.; Shimadera, H.; Uranishi, K.; Matsuo, T.; Kondo, A. Numerical assessment of $PM_{2.5}$ and O_3 air quality in continental Southeast Asia: Impacts of future projected anthropogenic emission change and its impacts in combination with potential future climate change impacts. *Atmos. Environ*. **2020**, *226*, 117398. doi: 10.1016/j.atmosenv.2020.117398.
17. Knowland, K.E. Global modeling and assimilation office file specification for MERRA-2 climate statistics products, 2020.
18. Bey, I.; et al. Global modelling of tropospheric chemistry with assimilated meteorology: Model description and evaluation. *J. Geophys. Res. Atmos*. **2001**, *106(D19)*, 23073–23095. doi: https://doi.org/10.1029/2001JD000807.
19. Keller, C.A.; Long, M.S.; Yantosca, R.M.; Da Silva, A.M.; Pawson, S.; Jacob, D.J. "HEMCO v1.0: A versatile, ESMF-compliant component for calculating emissions in atmospheric models. *Geosci. Model Dev.* **2014**, *7(4)*, 1409–1417. doi: 10.5194/GMD-7-1409-2014.
20. Keller, C.A.; Knowland, K.E. Description of the NASA GEOS Composition Forecast Modeling System GEOS-CF v1 0.pdf. *J. Adv. Model. Earth Syst*. **2021**, *13(4)*, e2020MS002413. doi: 10.1029/2020MS002413.
21. Knowland, K.E.; et al. NASA GEOS Composition Forecast Modeling System GEOS-CF v1.0: Stratospheric Composition. *J. Adv. Model. Earth Syst*. **2022**, *14(6)*, 1–28. doi: 10.1029/2021MS002852.
22. Eastham, S.D.; Weisenstein, D.K.; Barrett, S.R.H. Development and evaluation of the unified tropospheric-stratospheric chemistry extension (UCX) for the global

chemistry-transport model GEOS-Chem. *Atmos. Environ*. **2014**, 89, 52–63. doi: 10.1016/j.atmosenv.2014.02.001.

23. Bianz, H.; Prather, M.J. Fast-J2: Accurate simulation of stratospheric photolysis in global chemical models. *J. Atmos. Chem*. **2002**, *41(3)*, 281–296. doi: 10.1023/A:1014980619462.
24. Mao, J.; et al. Chemistry of hydrogen oxide radicals (HOx) in the Arctic troposphere in spring. *Atmos. Chem. Phys*. **2010**, *10(13)*, 5823–5838. doi: 10.5194/acp-10-5823-2010.
25. Sandu, A.; Sander, R. Technical note: Simulating chemical systems in Fortran90 and Matlab with the Kinetic PreProcessor KPP-2.1. *Atmos. Chem. Phys.* **2006**, *6(1)*, 187–195. doi: 10.5194/acp-6-187-2006.
26. Colarco, P.; Da Silva, A.; Chin, M.; Diehl, T. Online simulations of global aerosol distributions in the NASA GEOS-4 model and comparisons to satellite and ground-based aerosol optical depth. *J. Geophys. Res. Atmos.* **2010**, *115(D14)*, D14207. doi: 10.1029/2009JD012820.
27. Randles, C.A.; et al. The MERRA-2 aerosol reanalysis, 1980 onward. Part I: System description and data assimilation evaluation. *J. Clim*. **2017**, *30(17)*, 6823–6850. doi: 10.1175/JCLI-D-16-0609.1.
28. Janssens-Maenhout, G.; et al. HTAP-v2.2: A mosaic of regional and global emission grid maps for 2008 and 2010 to study hemispheric transport of air pollution. *Atmos. Chem. Phys*. **2015**, *15(19)*, 11411–11432. doi: 10.5194/acp-15-11411-2015.
29. Schultz, M.G.; et al. Global wildland fire emissions from 1960 to 2000. *Global Biogeochem*. *Cycles* **2008**, *22(2)*, 1–17. doi: 10.1029/2007GB003031.
30. Van der Gon, H.D.; Hendriks, C.; Kuenen, J.; Segers, A.; Visschedijk, A. TNO Report: Description of current temporal emission patterns and sensitivity of predicted AQ for temporal emission patterns. TNO, Princetonlaan 6, 3584 CB Utrecht, The Netherlands, 2011, pp. 1–22.
31. Bindle, L.; et al. Atmospheric chemistry model. Cambridge University Press, 2021, pp. 5977–5997.

JOURNAL OF
HYDRO-METEOROLOGY

Research Article

Exploring the training results of machine learning models using different batch sizes and epochs: A case study with GNSS time series data

Le Duc Tinh[1], Huynh Nguyen Dinh Quoc[2], Nguyen Gia Trong[1,3*]

[1] Faculty of Geomatics and Land Administration, Hanoi University of Mining and Geology; leductinh@humg.edu.vn , nguyengiatrong@humg.edu.vn
[2] Ho Chi Minh City University of Natural Resources and Environment; hndquoc@hcmunre.edu.vn
[3] Geodesy and Environment research group, Hanoi University of Mining and Geology;

*Corresponding author: nguyengiatrong@humg.edu.vn ; Tel.: +84–963124980

Received: 25 March 2024; Accepted: 03 May 2024; Published: 25 June 2024

Abstract: This study applies the GRU (Gated Recurrent Unit) model when selecting different values of batch-size, namely 16, 32, and 64, with varying epochs of 20, 50, 100, 150, and 200. The input data comprises observations collected by two GNSS CORS stations from the VNGEONET network, namely HYEN and CTHO, spanning from August 10, 2019, to March 18, 2022. Initially, GNSS CORS data is processed using Gamit/Globk software to obtain the Up-component, which serves as the input data for the GRU model. The research results indicate that the statistical performance metrics of the model, such as RMSE and MAE, decrease while the F-Score increases when the batch-size decreases and the epoch value increases. In cases where the Up-component exhibits irregular variations (seasonal fluctuations), the performance of the GRU model is subpar, with an F-Score of 0 observed when batch-size values are 32 and 64 and epoch value is 20. For data following the pattern of CTHO CORS station, the GRU model performs exceptionally well when batch-size is 16 and epoch is 200. However, the forecasting performance is low for data from HYEN CORS station, indicating the need for further investigation in the future.

Keywords: Artificial Intelligence; Batch size; Epoch; GRU; GNSS time-series.

1. Introduction

Due to technological advancements, data collection has been automated, continuous, or temporally dense, resulting in various types of time series data. Time series data in geospatial applications include GNSS, satellite altimetry, remote sensing data, etc. GNSS data has been applied in atmospheric layer research, oceanic observations, soil moisture monitoring, ice sheet observations [1], and tectonic plate movements [2], etc. Altimetry time series data is utilized in various marine activities, monitoring marine life, weather and climate forecasting, coastal inundation monitoring due to sea level rise or subsidence, natural disaster mitigation, etc. [3]. Remote sensing time series data applications include land cover classification [4], forest monitoring [5], erosion studies [6], etc. Research [7] has highlighted the extensive applications of artificial intelligence in large geospatial datasets, quality assessment, data modeling and structuring, data visualization and visual analytics, data mining, and knowledge discovery, etc. With the establishment continuosly operation reference station (CORS), users are provided with time-series data. The data provided by CORS station networks can be applied in various fields such as tectonic plate movement monitoring, sea

level monitoring, atmospheric research [8] etc. Data collected by CORS stations firstly need to be processed using high-precision GNSS data processing software such as Gamit/Globk [9], Bernese [10] etc. The result of this processing is the daily coordinate components of CORS stations. To analyze the daily time-series data obtained as mentioned above, various traditional solutions have been published, such as least-squares estimation, moving ordinary least-squares wavelet decomposition (WD), singular spectrum analysis (SSA), Kalman Filter (KF), adaptive wiener filter (AWF), or combinations thereof [11]. Additionally, artificial intelligence models have also been applied to analyze GNSS time-series data.

Five artificial intelligence models, namely attention mechanism with long short time memory neural network (AMLSTM), long short time memory neural network (LSTM), recurrent neural networks (RNN), support vector machine (SVM), and random forest (RF), have been utilized for landslide detection [12]. Additionally, the authors proposed combining the complete ensemble empirical mode decomposition with adaptive noise (CEEMDAN) technique with the LSTM model. Experimental results demonstrated that the CEEMDAN-LSTM model could be recommended for other landslide prediction studies and has significant potential in landslide risk assessment. The study [13] applied Gradient Boosting Decision Tree (GBDT), LSTM, and SVM models to analyze GNSS time-series data. The results showed that the proposed models had RMSE values ranging from 3mm to 5mm, smaller than those of corresponding traditional methods. Moreover, artificial intelligence models enable the integration of various factors causing in land surface movement from GNSS time series data [13].

The GBDT model has been used as a benchmark against the XGBoost and RF models for interpolating coordinate values in GNSS time-series data. The computational results indicate that the Up-component is interpolated with up to 45% greater accuracy compared to traditional methods, with the XGBoost model yielding the poorest interpolation results [14]. For each different setting of batch size and epoch, different artificial intelligence models will yield different prediction results. Research [15] has compiled errors for both training and testing datasets using batch sizes ranging from 64 to 2048. The results indicate that a batch size of 128 yields the smallest error for both datasets. Additionally, research [16] has shown that the noise level increases as the loss decreases during training and largely depends on the model size, with model performance being improved.

Research [17] has demonstrated that training with small batches has been proven to improve generalization performance and allows for significantly smaller memory usage, which can also be leveraged to enhance machine throughput. Nesterov and Adam optimizers have been found to train more efficiently than baseline models when using large batch sizes. There have been several publications on the application of artificial intelligence in analyzing time-series data. Author [18] employed a recurrent neural network to forecast meaningful wave heights for disaster prevention efforts in Vietnam. Research [19] applied an ANN model to analyze GNSS time-series data, yielding an RMSE determination of 0.006m. RNN models were chosen by authors [20] to predict surface water quality with an accuracy ranging from 75% to 85%. Although some studies have been published, there has been no research in the earth science field specifically addressing experimentation with different batch sizes and epochs to analyze time-series data.

This study evaluates the performance of the GRU model by configuring different values of batch size and epoch during model execution, applied in a typical case of analyzing GNSS time-series data.

2. Data and Research methodology

2.1. Data

The data used in this paper was collected by continuosly operation reference station (CORS) receivers, belonging to the VNGEONET network, namely CTHO and HYEN,

provided by the Department of Survey and Mapping, Vietnam. Information regarding the GNSS data used in this study is provided as shown in Table 1.

Table 1. Information about measurement data at GNSS CORS stations.

Station name	Time		Receiver type	Antenna type	Interval (second)
	First epoch	Last epoch			
CTHO HYEN	2019/08/10	2022/03/18	LEICA GR50	LEIAR25.R4 LEIT	30

The positions of the HYEN CORS station and the CTHO CORS station are depicted as shown in Figure 1.

Figure 1. The positions of the HYEN CORS station and the CTHO CORS station.

2.2. Methodology

The data as described in Table 1 was processed using Gamit/Globk software to obtain daily coordinate components (including the North, East, and Up components) of the GNSS CORS stations. The up-component value series was then utilized as the input data for the GRU model. The research methodology of the paper is provided in Figure 2.

The GNSS data, once collected, will be converted into RINEX data format and analyzed using the Gamit/Globk software [21] to obtain daily coordinate components of the stations. The GNSS data processing procedure in this case has been presented in the study [22].

The Gated Recurrent Unit (GRU) is a type of artificial neural network model, particularly suited for sequential data processing tasks such as natural language processing and time series analysis. Developed as an enhancement of the traditional recurrent neural network (RNN), the GRU addresses some of the shortcomings of the standard RNN architecture, particularly in handling long-range dependencies and the vanishing gradient problem.

One of the key features of the GRU is its gating mechanism, which allows it to selectively update and forget information over time. This mechanism consists of update and reset gates, which regulate the flow of information within the network. By adaptively controlling the flow of information, the GRU is able to capture relevant patterns and dependencies in sequential data

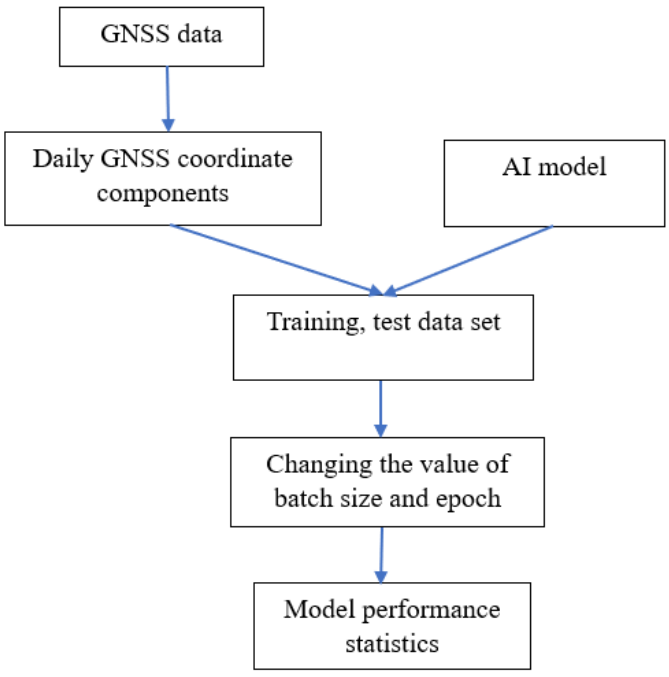

Figure 2. Experimental method of artificial intelligence model testing with different batch sizes and epochs.

more effectively. Compared to the long short-term memory (LSTM) model, another popular variant of the RNN architecture, the GRU offers similar performance with a simpler structure, requiring fewer parameters to train and often achieving faster convergence during training. Its computational efficiency and competitive performance make it a popular choice for various sequence modeling tasks in both research and practical applications.

Based on the selected model, Python language and library functions were utilized to construct the experimental computation program [23, 24], etc.

To achieve the desired results, the research team conducted experiments with batch sizes set to 16, 32, and 64, and for epochs, values were assigned as 10, 50, 100, 150, and 200, respectively. Model evaluation was performed by statistically analyzing performance metrics including RMSE, MAE, and F-score. To assess the performance of the model, evaluation methods similar to those used in studies [18, 19] were employed. The operation method of the GRU model in this case is depicted as shown in Figure 3.

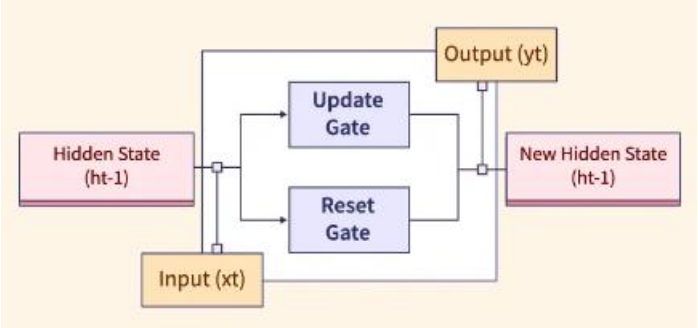

Figure 3. Prediction method with the GRU model.

3. Results and Discussion

3.1. Results obtained with the dataset from HYEN CORS station

From the data in Table 2, it can be observed that the RMSE value increases rapidly when the epoch value is small and the batch-size value increases from 16 to 64. For the same batch-size value, as the epoch value increases, the RMSE value decreases. In the case of the largest batch-size value (with a value of 64), the RMSE value decreases very rapidly. The minimum RMSE value for HYEN CORS station is achieved at 0.010 when batch-size = 16 and epoch = 200.

Table 2. RMSE determination results with data from HYEN CORS station.

Batch size	Epoch				
	20	**50**	**100**	**150**	**200**
16	0.543	0.487	0.248	0.017	0.010
32	5.626	0.557	0.541	0.337	0.103
64	13.394	0.611	0.651	0.606	0.512

Table 3. MAE determination results with data from HYEN CORS station.

Batch size	Epoch				
	20	**50**	**100**	**150**	**200**
16	0.469	0.379	0.192	0.014	0.006
32	5.618	0.429	0.420	0.261	0.079
64	13.393	0.468	0.506	0.471	0.398

The variation in the MAE values for the input data from HYEN CORS station is similar to RMSE. The minimum MAE value achieved is 0.006, corresponding to a batch-size of 16 and epoch of 200.

In AI applications, the F-score, also known as the F1-score, is a metric commonly used to evaluate the performance of a binary classification model. It is the harmonic mean of precision and recall, providing a single measure that balances between these two metrics. Precision measures the proportion of true positive predictions among all positive predictions, while recall measures the proportion of true positive predictions among all actual positives. The F-score ranges from 0 to 1, where a higher score indicates better performance. It's particularly useful when the class distribution is imbalanced, as it considers both false positives and false negatives. The determined F-Score results in this case are as follows:

Table 4. Results of F-Score determination with data from HYEN CORS station.

Batch size	Epoch				
	20	**50**	**100**	**150**	**200**
16	0.312	0.181	0.417	1.000	1.000
32	0.000	0.181	0.179	0.265	0.473
64	0.000	0.146	0.174	0.174	0.179

Table 4 demonstrates the very high performance of the model when selecting batch-size = 16 and epoch = 200; when batch-size is set to 32 or 64, with epoch = 20, the model's predictive performance equals 0. This aligns perfectly with the significantly large RMSE and MAE values. Figures 4, 5, 6 below represent the predicted values, actual values on the test dataset, the entire dataset, and the loss curve in the case of batch-size = 16 and epoch = 200 for the HYEN CORS station dataset.

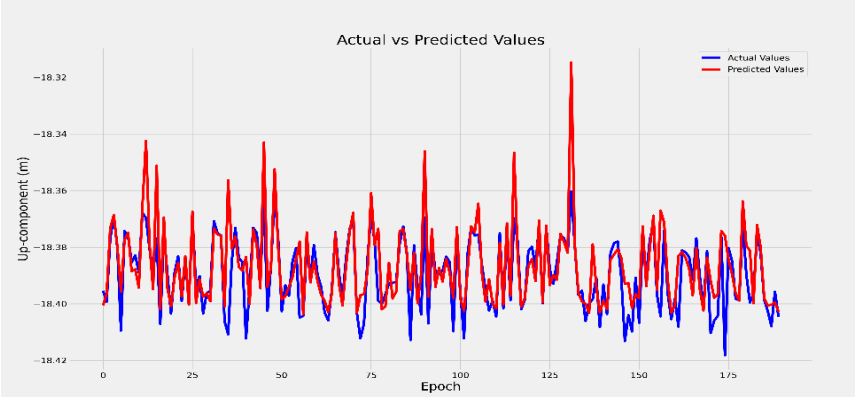

Figure 4. Predicted values on the test dataset of HYEN CORS station

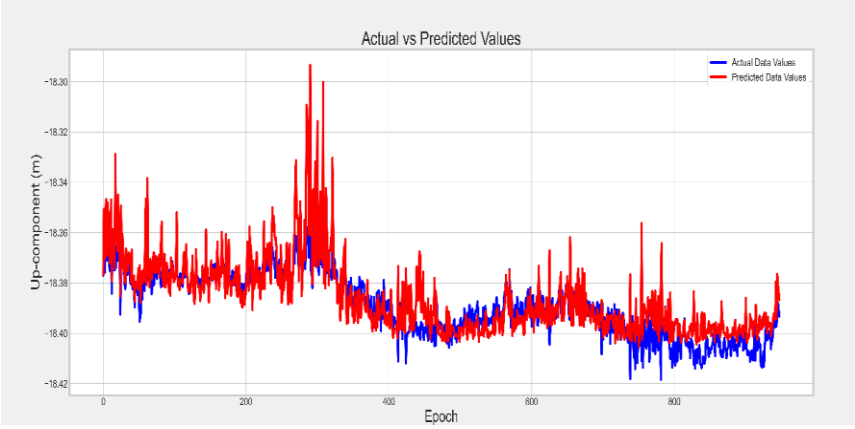

Figure 5. Actual and predicted values on the entire dataset of HYEN CORS station.

From Figure 4, it can be observed that the predicted values are significantly higher than the actual values. There are several factors that may contribute to this phenomenon, including unusual fluctuations in the daily Up-component. To accurately conclude on the

aforementioned phenomenon, it is necessary to gather additional closely related data concerning the variations of the Up-component, such as meteorological data, hydrological and geological data, etc.

Figure 6. Loss curve on the test dataset of HYEN CORS station.

From Figure 5, it can be observed that the variation in the Up-component displacement of HYEN CORS station does not exhibit periodicity as some published results have indicated [25]. Figure 7 shows the Up-component results of the HYEN CORS station determined using the Gamit/Globk software, serving as evidence for the arguments presented above.

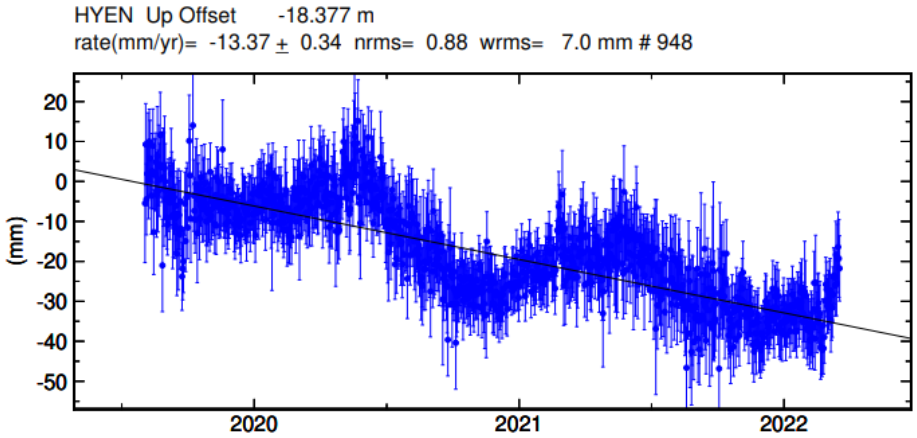

Figure 7. Up-component results of the HYEN CORS station were determined by the Gamit/Globk software.

In Figure 7, the vertical axis represents the daily changes in the up-component (measured in mm), while the horizontal axis represents time (measured in years).

This may lead to the predictive performance of the artificial intelligence model in this case not being as high as the results achieved even with the use of a simple artificial intelligence model [19].

3.2. Results obtained with the dataset from CTHO CORS station

Table 5. RMSE determination results with data from CTHO CORS station.

Batch size	Epoch				
	20	**50**	**100**	**150**	**200**
16	0.1523	0.0870	0.00154	0.00098	0.00074
32	0.1632	0.1513	0.0469	0.00136	0.00129
64	0.2668	0.1846	0.1410	0.07414	0.00213

From Table 5, it can be observed that the RMSE values decrease only slightly as the batch-size varies from 16 to 64. This indicates the suitability of the artificial intelligence model being employed.

Table 6. MAE determination results with data from CTHO CORS station.

Batch size	Epoch				
	20	**50**	**100**	**150**	**200**
16	0.1175	0.0686	0.0010	0.00062	0.00053
32	0.1255	0.1179	0.0370	0.00084	0.00058
64	0.2303	0.1424	0.1110	0.05866	0.00091

Table 7. F-Score determination results with data from CTHO CORS station.

Batch size	Epoch				
	20	**50**	**100**	**150**	**200**
16	0.5573	0.5653	0.95216	0.9621	0.9589
32	0.5490	0.5447	0.55288	0.9522	0.9504
64	0.2312	0.5367	0.54468	0.5778	0.9256

From the data in Table 5 to Table 7, it can be observed that the fluctuation trends of RMSE, MAE, and F-Score values for the data from CTHO CORS stattion are similar to those for HYEN CORS station. However, the variation of the Up-component for CTHO CORS station is similar to previous publications (Figure 8).

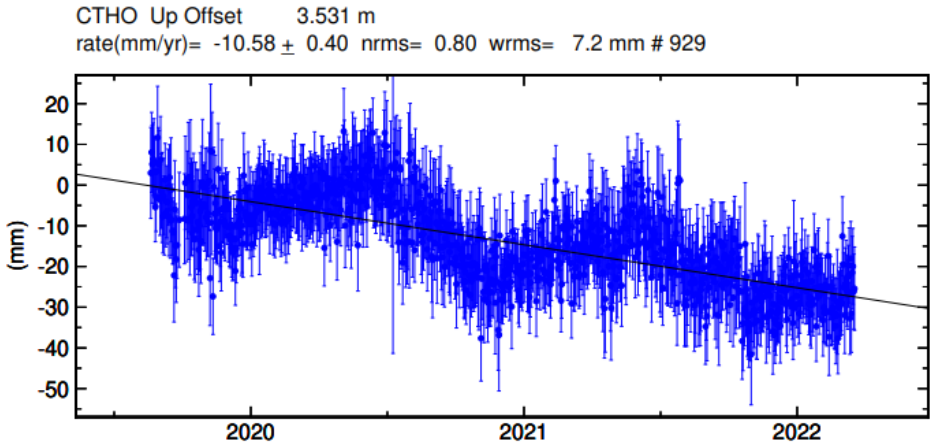

Figure 8. Graph of Up-component of CTHO CORS station determined by Gamit/Globk.

The up-component values in Figure 8 demonstrate a systematic variation of this component for the CTHO CORS station, explaining the F-score values of 0.5490 and 0.2312 respectively for batch-size = 32 and 64, epoch = 20. The RMSE = 0.00074 and MAE = 0.00053 for batch-size = 16 and epoch = 200. These indicate very high performance in predicting the determined quantity from the GNSS time-series data compared to existing publications [13,19,26]. These are promising preliminary results in the application of artificial intelligence models for analyzing GNSS time-series data.

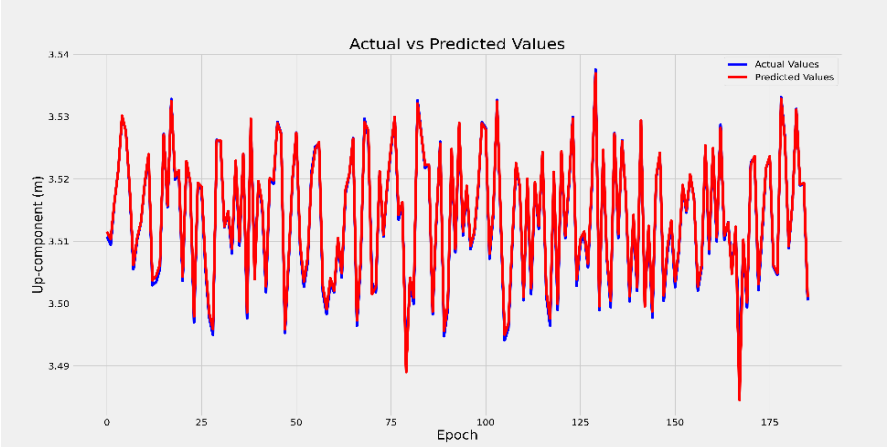

Figure 9. Predicted and actual values for the test dataset of the CTHO CORS station.

The graphs representing the actual values, predicted values on the test dataset, the entire dataset, and the loss curve when analyzing the CTHO CORS station data in the case of batch-size = 16 and epoch = 200 are shown in Figures 9 to 11.

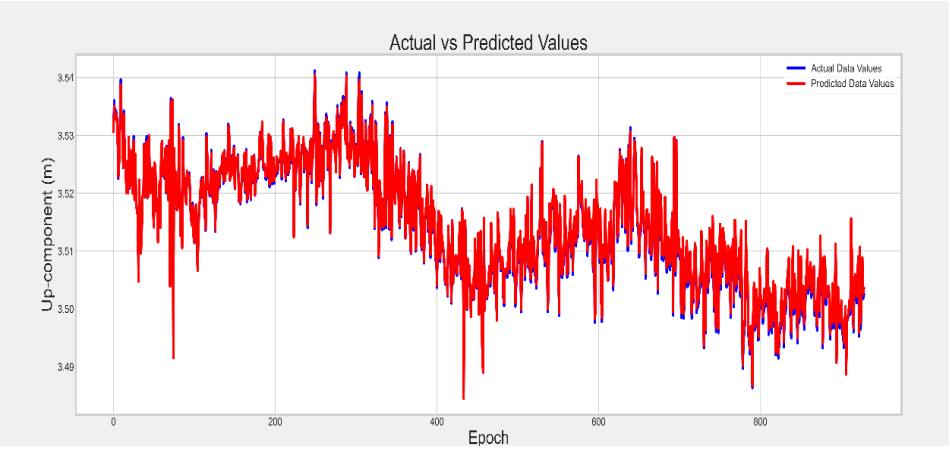

Figure 10. Predicted and actual values for the entire dataset of the CTHO CORS station.

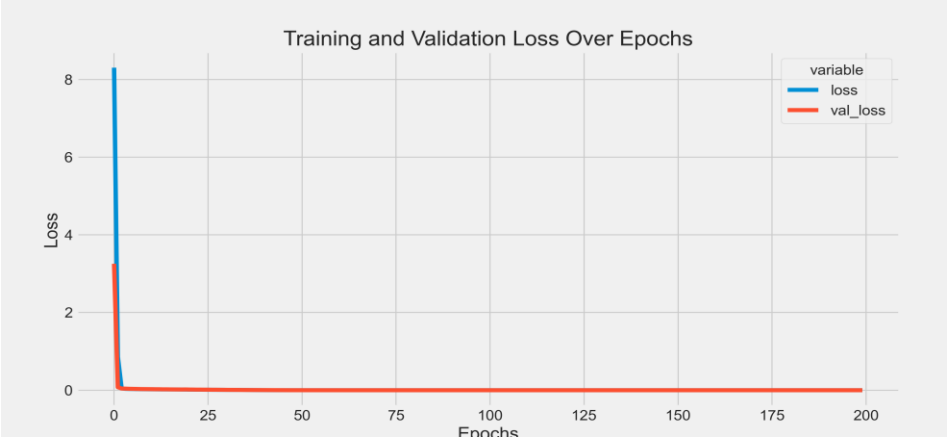

Figure 11. Loss curve of the test dataset of the CTHO CORS station.

Figures 9 and 10 demonstrate the very high suitability of the GRU model for the data of the CTHO CORS station, as evidenced by the predicted values closely matching the actual values across the datasets. Additionally, the loss value nearly approaches zero after a few epochs (Figure 11).

4. Conclusion

This study successfully experimented with different values of batch-size and epoch when analyzing GNSS time-series data using the artificial model. When applying artificial intelligence (specifically the GRU model) to analyze GNSS time series, it is necessary to select a small batch size value (specifically 16) to achieve the best forecasting performance with the model.

The experimental results demonstrate that when the up-component varies irregularly, unlike in the case of HYEN CORS station, predicting using artificial intelligence models is not very effective. Specifically, when the epoch value is 20 and the batch-size is 32 and 64 respectively, the GRU model cannot predict the Up-component values in this case, as indicated by an F-Score of 0.

Statistical metrics such as RMSE and MAE decrease, while F-Score increases (indicating improved prediction performance with artificial intelligence models) as the batch-size decreases and epoch increases. The prediction results show very high performance for the

CTHO CORS station dataset when batch-size = 16 and epoch = 200, demonstrated by metrics such as RMSE = 0.00074, MAE = 0.00053, and F-Score = 0.9589. This performance is excellent compared to existing publications.

One limitation of this study is that it does not propose a solution for forecasting or analyzing the Up-component in cases where the variation is irregular, as in the case of the HYEN CORS station. This is an issue that requires further investigation in the future.

Author contributions: Conceptualization: L.D.T., N.G.T., H.N.D.Q.; Methodology: L.D.T., N.G.T., H.N.D.Q.; Data processing: N.G.T., N.N.D.Q.; Writing - original draft: L.D.T., N.G.T., H.N.D.Q.; Writing - review and editing: N.G.T.

Declaration: The authors collectively declare that this article is the result of their research, not previously published elsewhere, and not copied from previous studies; there is no conflict of interest among the authors.

Acknowledgments: The authors of this paper sincerely thank the Department Of Survey, Mapping and Geographic Information Vietnam for providing the data; the Ministry of Education and Training under project code B2022-MDA-09 for providing the funding to conduct this research.

References

1. Yu, K.; Rizos C.; Burage, D.; Dempster, A.G.; Zhang, K.; Markgraf, M. An overview of GNSS remote sensing. *EURASIP J. Adv. Signal Process.* **2014**, *134*, 1–14.
2. Bastos, L.; Bos, M.; Fernandes, R.M. Deformation and tectonics: contribution of GPS measurements to plate tectonics–overview and recent developments. *Sci. Geodesy-I.* **2010**, 155–184.
3. Srinivasan, M.; Tsontos, V. Satellite altimetry for ocean and coastal applications: A review. *Remote Sens.* **2023**, *15(16)*, 3939. https://doi.org/10.3390/rs15163939.
4. Gómez, C.; White, J.C.; Wulder, M.A. Optical remotely sensed time series data for land cover classification: A review. *ISPRS J. Photogramm. Remote Sens.* **2016**, *116*, 55–72.
5. Banskota, A.; Kayastha N.; Falkowski M.J.; Wulder M.A.; Froese R.E.; White J.C. Forest monitoring using Landsat time series data: A review. *Can. J. Remote Sens.* **2014**, *40(5)*, 362–384.
6. Vrieling, A.J.C. Satellite remote sensing for water erosion assessment: A review. *Catena* **2006**, *65(1)*, 2–18.
7. Li, S.; Dragicevic, S.; Castro, F.A.; Sester, M.; Winter, S.; Coltekin, A.; Pettit, A.; Jiang, B.; Haworth, J.; Stein, A.; Cheng, T. Geospatial big data handling theory and methods: A review and research challenges. *ISPPS J. Photogramm. Remote Sens.* **2016**, *115*, 119–133.
8. Trong, N.G.; Tinh, L.Đ.; Cuong, N.V.; Quang, P.N. GNSS Data Processing: Theory, Software, and Applications. Transport Publishing House, 2023, pp. 300.
9. Li, Y. Analysis of GAMIT/GLOBK in high-precision GNSS data processing for crustal deformation. *Earthquake Res. Adv.* **2021**, *1(8-11)*, 100028. https://doi.org/10.1016/j.eqrea.2021.100028.
10. Cetin, S.; Aydin, C.; Dogan, U. Comparing GPS positioning errors derived from GAMIT/GLOBK and Bernese GNSS software packages: A case study in CORS-TR in Turkey. *Surv. Rev.* **2019**, *51(369)*, 533–543.
11. Klos, A.; Bogusz, J.; Bos, M.S.; Gruszczynska, M. Modelling the GNSS time series: different approaches to extract seasonal signals. *Geodetic Time Ser. Anal. Earth Sci.* 2020, pp. 211–237.
12. Wang, J.; Nie, G.; Gao, S.; Wu, S.; Li, H.; Ren, X. Landslide deformation prediction based on a GNSS time series analysis and recurrent neural network model. *Remote Sens.* **2021**, *13(6)*, 1055. https://doi.org/10.3390/rs13061055.

13. Gao, W.; Li, Z.; Chen, Q.; Jiang, W.; Feng, Y. Modelling and prediction of GNSS time series using GBDT, LSTM and SVM machine learning approaches. *J. Geod.* **2022**, *96(10)*, 71. https://doi.org/10.1007/s00190-022-01662-5.
14. Li, Z.; Lu, T.; Yu, K.; Wang, J. Interpolation of GNSS position time series using GBDT, XGBoost, and RF machine learning algorithms and models error analysis. *Remote Sens.* **2023**, *15(18)*, 4374. https://doi.org/10.3390/rs15184374.
15. Hoffer, E.; Hubara, I.; Soudry, D. Train longer, generalize better: Closing the generalization gap in large batch training of neural networks. *Adv. Neural Inf. Process. Syst.* **2017**, 1–13.
16. McCandlish, S.; Kaplan, J.; Amodei, D.; Team, O.D. An empirical model of large-batch training. *ArXiv* **2018**, 1–35. https://doi.org/10.48550/arXiv.1812.06162.
17. Masters, D.; Luschi, C. Revisiting small batch training for deep neural networks. *Comput. Sci. Mach. Learn.* **2018**, 1–18. https://doi.org/10.48550/arXiv.1804.07612.
18. Thai, T.H.; Khiem, M.V.; Thuy, N.B.; Ha, B.M.; Ngoc, P.K. Building a regression neural network model to predict significant wave heights at Con Co station, Quang Tri, Vietnam. *J. Hydro-Meteorol.* **2022**, *EME4*, 73–84.
19. Phong, D.V.; Trong, N.G.; Chien, N.V.; Thanh, N.H.; Ha, L.L.; Quan, N.V.; Quang, P.N. Analysis of land vertical movement using ANN function from the results of processing GNSS time series data. *J. Hydro-Meteorol.* **2023**, *752*, 41–50.
20. Phong, N.D.; Duong, H.H. Application of deep learning models in forecasting surface water quantity of Bac Hung Hai irrigation system. *Water Resour. Mag.* **2023**, *1*, 61–72.
21. Available online: https://geoweb.mit.edu/gg/.
22. Trong, N.G.; Nghia, N.V.; Khai, P.C.; Thanh, N.H.; Ha, L.L.; Dung, V.T.; Quan, N.V.; Quang, P.N. Determination of tectonic velocities in Vietnam territory based on data of CORS stations of VNGEONET network. *J. Hydro-Meteorol.* **2022**, *739*, 59–66.
23. Available online: https://www.python.org/.
24. Available online: https://anaconda.org/anaconda/pandas.
25. Savchuk, S.; Doskich, S.; Golda, P.; Rurak, A. The Seasonal Variations Analysis of Permanent GNSS Station Time Series in the Central-East of Europe. *Remote Sens.* **2023**, *15(15)*, 3858. https://doi.org/10.3390/rs15153858.
26. Carbonari, R.; Riccardi, U.; Martino, P.D.; Cecere, G.; Maio, R.D. Wavelet-like denoising of GNSS data through machine learning. Application to the time series of the Campi Flegrei volcanic area (Southern Italy). *Geomatics Nat. Hazards Risk* **2023**, *14(1)*, 2187271. https://doi.org/10.1080/19475705.2023.2187271.

Table of content